

AN EXPERIMENTAL SEARCH FOR
THE ELECTRON ELECTRIC DIPOLE MOMENT IN A
GADOLINIUM GALLIUM GARNET CRYSTAL

Young Jin Kim

Submitted to the faculty of the University Graduate School
in partial fulfillment of the requirements
for the degree
Doctor of Philosophy
in the Department of Physics,
Indiana University

September 2011

UMI Number: 3488085

All rights reserved

INFORMATION TO ALL USERS

The quality of this reproduction is dependent on the quality of the copy submitted.

In the unlikely event that the author did not send a complete manuscript and there are missing pages, these will be noted. Also, if material had to be removed, a note will indicate the deletion.



UMI 3488085

Copyright 2011 by ProQuest LLC.

All rights reserved. This edition of the work is protected against unauthorized copying under Title 17, United States Code.



ProQuest LLC.
789 East Eisenhower Parkway
P.O. Box 1346
Ann Arbor, MI 48106 - 1346

Accepted by the Graduate Faculty, Indiana University, in partial fulfillment of the requirements of the degree of Doctor of Philosophy.

Doctoral

Committee

Chen-Yu Liu, Ph.D.

(Principal Advisor)

W. Michael Snow, Ph.D.

Scott W. Wissink, Ph.D.

August 15, 2011

John P. Carini, Ph.D.

Copyright © 2011 by
Young Jin Kim
ALL RIGHTS RESERVED

Acknowledgments

This thesis work has been made possible with the support, instruction, and friendship of many people. In first place, I am heartily thankful to my advisor, Prof. Chen-Yu Liu, whose exceptional patience, encouragement and supervision from start to finish enabled me to develop an understanding of the project as well as to take the project to the next level. Her brilliant scientific ideas and suggestions always amazed me. I would also like to thank my committee members. Prof. W. Michael Snow offered useful suggestions and advice for improving experiments. He also encouraged me to have broaden my thoughts in physics. Prof. Scott W. Wissink offered his great teaching skills and clarity to improve my knowledge of nuclear physics as well as useful suggestions. Prof. John P. Carini enlightened me with his skillful teaching at the start of my research.

I would also like to thank the two talented engineers Gerard Visser and Brandon Kunkler who have instructed me to develop and improve electronic devices that are essential for the project. I have learned much in discussions with them. I am also very thankful to my wonderful colleagues Maciej Karcz and Xiaoying Pang. Their kind help always cheered me. Finally, I have deeply appreciative of the support from my family.

The thesis work was supported from the IU center for Spacetime Symmetries and NSF Grants No. PHY-0457219, PHY-0758018.

Young Jin Kim

AN EXPERIMENTAL SEARCH FOR THE ELECTRON ELECTRIC DIPOLE MOMENT IN A GADOLINIUM GALLIUM GARNET CRYSTAL

This dissertation reports results of an experimental search for the intrinsic Electric Dipole Moment (EDM) of the electron using a solid-state technique. The search for the electron EDM is intended to test the discrete symmetries assumed in the Standard Model (SM) of particle physics. Due to the different transformation properties of the EDM (a polar vector) and the spin (a pseudo-vector), the electron EDM requires the physical laws governing the electron to violate both the time reversal (T) and the parity (P) symmetries. While the phenomena of P violation is firmly established in numerous experiments, T violation has only been observed directly in the neutral-kaon system, with more searches in the B system underway. A nonzero EDM measurement would provide crucial information about the nature of T -violation. The physics of T violation is often linked, via the CPT theorem, to the violation of the combined Charge conjugation (C) and parity symmetries. CP violation is needed to explain the mystery of the observed matter-antimatter asymmetry in the present Universe. Using the known CP violation in the CKM matrix, the SM predicts the electron EDM to be smaller than 10^{-38} e·cm, which is well beyond the reach of the current experimental techniques. New sources of CP violation beyond the SM often lead to a sizable EDM that can be compared with experimental constraints. Free from the SM backgrounds, measurements of EDM are a powerful way to test various extensions to the SM.

While the conventional experimental technique used to measure EDM is based on nuclear magnetic resonance, we are pursuing an alternative approach using a

solid state technique at a low temperature that would improve the present experimental limit on the electron EDM. The experiment uses a paramagnetic insulator Gadolinium Gallium Garnet with a large magnetic susceptibility. The presence of the electron EDM leads to a small but non-zero magnetization when the garnet sample is subjected to a strong electric field. The resulting Stark-induced magnetization is measured using a state-of-the art Superconducting Quantum Interference Device (SQUID) magnetometer. In this dissertation, the solid state method is described and progress on efforts to control the systematic effects and improve the sensitivity are discussed. The major efforts include the design and implementation of a 24-bit data acquisition system with ultra-low degrees of channel cross-talk as well as the control of the voltage drift from the high voltage polarity switch system. This dissertation reports the first background-free experimental limit on the electron EDM of $(-5.57 \pm 7.98 \pm 0.12) \times 10^{-25}$ e·cm with 5 days of data averaging. The limit is presently the most sensitive result achieved using the solid state technique.

Chen-Yu Liu, Ph.D.

W. Michael Snow, Ph.D.

Scott W. Wissink, Ph.D.

John P. Carini, Ph.D.

Contents

Acceptance	ii
Acknowledgments	iv
Abstract	v
1 Introduction	1
1.1 Overview of the Electric Dipole Moment	1
1.1.1 What is the Electric Dipole Moment	1
1.1.2 Violation of Fundamental Discrete Symmetries	3
1.1.3 Theoretical Model Prediction for the Electron EDM	9
1.2 Methods Used for the Electron EDM Search	11
1.2.1 Thallium Atomic Beam EDM Experiment	12
1.2.2 The EDM Experiment in the Polar Molecule YbF	13
1.2.3 The EDM Experiment Using Gadolinium Iron Garnet	15
2 Experimental Approach	16
2.1 New Approach Using a Solid State Technique	16
2.1.1 First Proposal	16
2.1.2 First Proposal in Gadolinium Gallium Garnet	18
2.2 Choice of a Material	19
2.2.1 Properties of GGG	20

2.2.2	Structure Details of GGG	21
2.2.3	Original Estimate of EDM Enhancement Factor in GGG	24
2.3	Choice of the Magnetometer	25
2.3.1	Introduction to SQUID	26
2.3.2	SQUID Readout Electronics	27
2.3.3	Operation of the SQUID	29
3	Sample Characterization	32
3.1	Sample Preparation	32
3.2	Magnetic Susceptibility	33
3.2.1	Correction for the Demagnetization Effect	34
3.2.2	Magnetic Susceptibility of a Polycrystalline GGG Solid	37
3.2.3	Magnetic Susceptibility of a Single Crystal GGG Solid	40
3.2.4	Discussion	41
3.3	Particular Magnetic Property of the GGG Solid	42
3.3.1	Geometric Frustration	42
3.3.2	Possible Improvements	44
3.4	Dielectric Constant Measurement	45
3.4.1	Capacitance Determination	46
3.4.2	Numerical Analysis	48
4	Experimental Details	49
4.1	Experimental Design	49
4.1.1	Experimental Setup	49
4.1.2	Optimized Pickup Coil Design	54
4.1.3	Flux Enhancement Factor of the Pickup Coil	56
4.2	EDM-Induced Magnetic Flux	59
4.2.1	Effective EDM Enhancement Factor	60
4.2.2	Effect of the Sample Geometry	61

4.2.3	Flux Transfer Efficiency	63
4.2.4	Conclusion	66
5	Essential Improvements	67
5.1	A High Dynamic Range Data Acquisition System	67
5.1.1	Motivation	67
5.1.2	Description of the hardware	69
5.1.3	Performance Characterization	75
5.1.4	Conclusion	86
5.2	Low Distortion HV Polarity Switch System	87
5.2.1	Motivation	87
5.2.2	Description of New HV Polarity Switch System	90
5.2.3	Voltage Drift on the HV Polarity Switch System	98
5.2.4	Conclusion	102
5.3	Improvement of the Statistical Sensitivity	103
5.3.1	Stable Operation of the SQUID Sensor	103
5.3.2	Magnetic Shielding Improvement	106
5.3.3	Conclusion	108
6	Experiment Results	110
6.1	Data Analysis	110
6.1.1	Experimental Method	110
6.1.2	EDM Extraction Algorithms	115
6.1.3	Error-Weighting for Data Averaging	119
6.2	Discussion	120
6.2.1	Systematic Effects	121
6.2.2	Final Electron EDM Value	126
7	Conclusions and Future Work	127
7.1	Conclusions of the EDM Experiment	127

7.2	Further Improvements and Prospects	128
7.2.1	Low-Temperature EDM Experiment	128
7.2.2	Design for the Next-Generation EDM Experiment	129
7.2.3	High Voltage System Improvements	135
7.2.4	Conclusion	137
Appendix		139
A	Magnetic Property Measurement at Milli-Kelvin Temperatures	139
A.1	Design and Method	139
A.2	Preliminary Results	144
A.3	Future Work	145
B	Analytical Model for Geometry-Dependent Flux Suppression	147
C	Matlab Script for Data Control and Data Storage	154
Bibliography		163

List of Tables

5.1	Maximum bandwidths and ENOBs	76
5.2	dV/dt of drive signal from the DS360 function generator and HV monitor outputs evaluated in the last 30 % of the half cycle.	101
5.3	dV/dt of drive signal from the 33220A function generator and HV monitor outputs evaluated in the last 30 % of the half cycle.	101
6.1	Systematic effects	125
7.1	Total enhancement of the EDM sensitivity from changing the gap size between two GGG samples.	131
7.2	Total enhancement of the EDM sensitivity from changing the dimensions of lead shields.	132
7.3	Total enhancement of the EDM sensitivity from the change of the sample height.	134

List of Figures

1.1	Vacuum polarization producing virtual electron-positron pairs around an electron. The electron is dressed by a charge cloud of the pairs. . .	2
1.2	Two Feynman diagrams, (a) and (b), for K mesons oscillations via the weak interaction in SM.	6
1.3	Violation of P - and T -symmetries resulting from the existence of the EDM in an elementary particle.	7
1.4	One-loop electron EDM contribution in the SUSY model. \tilde{e} is a scalar electron and \tilde{f} is a neutralino.	10
2.1	The garnet structure of GGG. (a) The unit cell of GGG which contains 24 Gd^{3+} at {c} site (dodecahedral structure), 16 Ga^{3+} at [a] site (octahedron structure), and 24 Ga^{3+} at (d) site (tetrahedron). No oxygen ions are shown. (b) Detailed sub lattices of cations related to neighbor oxygen ions. The figures adapted from Ref. [39].	22
2.2	Positions of the Gd ions in the garnet structure. There are 24 Gd^{3+} ions per unit cell. The projection along a [111] direction is shown in (b). The Gd ions are divided into two interpenetrating sublattices. The figures adapted from Ref. [40, 41].	23
2.3	(a) DC SQUID with a bias current I_b . (b) V - I characteristic of DC SQUID. (c) V - Φ of characteristic of DC SQUID.	27
2.4	FLL circuit for the DC SQUID.	28

2.5	One example of a SQUID $V-\Phi$ output signal: (a) without the flux-lock loop operated and (b) with the flux-lock loop operated. The green square wave signal (ch4) with the same frequency as the test signal is a typical triggering source.	30
3.1	Setup for synthesizing the polycrystalline GGG specimens with solid-state reaction methods. (a) Powder of Gd_2O_3 and Ga_2O_3 . (b) Mortar and pestle to grind and mix these powders. (c) High temperature furnace for sintering. (d) Synthesized poly-crystalline GGG samples.	33
3.2	Solution of the finite-element analysis calculation investigating the demagnetization factor in 2-D color-coded filled contour plot of B_z in Tesla along the $y = 0$ plane.	36
3.3	Volume magnetic susceptibility (in CGS unit) of the polycrystalline GGG solid as a function of temperature, measured at a maximum applied magnetic field of 400 Oe. The dashed red curve shows the Curie-Weiss fit. The temperature-axis is in log scale.	39
3.4	Volume magnetic susceptibility of the single crystal GGG sample as a function of temperature, measured at the external field of 400 Oe. The direction of external fields are applied along z (blue circle), x (red triangle), and y (black square).	40
3.5	Displacement current measurement for the capacitance determination of the GGG/electrodes capacitor. The applied ramp wave is plotted with black circle dots while the measured displacement current is plotted with blue square dots. These time traces have been averaged 512 times.	46
3.6	Estimated capacitance from the field simulation solutions as a function of the set value of dielectric constant in field simulations. The dashed red line indicates the least-square line fit of the data.	47

4.1	Schematic of the experimental setup for the GGG-based solid-state electron EDM experiment.	50
4.2	Photographs of the experimental setup. (a) The assembly that houses the GGG samples and electrodes. (b) The assembly surrounded by two layers of superconducting lead foils. (c) Additional magnetic shields of three layers of Mu-metal wound on square forms with symmetry axes along the x , y , and z directions.	51
4.3	Photographs of the instrumentations. (a) The samples/electrodes assembly is encased by several magnetic shields. The HV lines and leakage current monitor wires are surrounded by lead tubing. The magnetic-shielded SQUID control wires (3 pairs) are connected to a RF-shielded connection box. (b) The continuous-flow helium cryostat. The system is fully immersed in a liquid helium bath. (c) A cylinder of Co-netic ferromagnetic shielding encompasses the whole cryostat for further improvement of magnetic shielding.	52
4.4	Magnetic flux noise spectra of the SQUID magnetometer. The solid (red) and dashed (blue) spectra are with and without a semitron electrode, respectively. The magnetic noise at 1 kHz with the electrode installed is a factor of 1.8 larger than without the electrode installed.	53
4.5	The magnetic flux pickup coil. The inner diameter matches the diameter of the GGG sample. For best CMRR, the inner area πR_1^2 is matched to the outer area $\pi R_3^2 - \pi R_2^2$ where $R_1 = R_2$. (a) Schematic representation of the pickup coil geometry. (b) Photograph of the actual assembled home-made pickup coil. The white material used to hold the niobium wires is machinable MACOR ceramic.	55

4.6	Solutions of the finite-element analysis calculations. (a) 2-D color-coded filled contour plot of B_z in Tesla along the plane of $y=0$. The pickup coil is positioned 0.71 cm away from the immediate surface of each sample. (b) Line scans of B_z along $z=0$ where the pickup coil is placed. Solid (Red) and dashed (Green) lines denote the inner and outer coils of the pickup coil.	57
4.7	2-D schematic of lattice deformation [66]. $2p_\sigma$ electrons of O^{-2} penetrate inside the shifted Gd core.	61
4.8	Solutions of finite-element analysis calculations for estimating the flux suppression factor f . (a) 3-D color-coded filled contour plot of B_z in Tesla including a slice plane along $z=0$ cm. The sample/electrodes assembly is cut along a plane of $y=0$ for better visualization. (b) Line scans of B_z along the line $z=0$ and through the center of the sample with square black dot and circle blue dot, respectively. The red dashed lines denote the diameter of the GGG sample.	62
4.9	(a) Schematic circuit diagram of the SQUID sensor inductively coupled to the flux pickup coil. (b) Photograph of the SQUID sensor used in the EDM experiment. The sensor is shielded by a superconducting lead box from external magnetic fields and mounted with Blu-Tac inside the lead box to reduce its vibration.	64
5.1	Block diagram of the DAQ system.	69
5.2	Simplified schematic diagram of the low noise front-end of the ADC board.	71
5.3	Assembled ADC board inside a heavy-duty RF shielding enclosure that is 12 cm \times 12 cm in size. The analog voltage signal is input into the BNC connector on the left, and the 12 VDC powers is connected through the black and red banana connectors on the right. Two TOSLink optical modules (transmitter and receiver) are also on the right.	73

5.4	Block diagram of the master board.	74
5.5	Histograms of intrinsic rms noise of the DAQ system at OSR=16384 (left plot) and OSR=128 (right plot). The analog input is terminated in these measurements. The red lines is the Gaussian fit providing the standard deviation of each histograms as the rms noise.	77
5.6	Power Spectral Density (PSD) spectra of the intrinsic rms noise of the DAQ system at OSR=16384 (left plot) and 128 (right plot). The vertical axis is in log scale.	78
5.7	Intrinsic rms noise of the DAQ system as a function of the input voltage. The red curve shows the model fit.	80
5.8	Channel cross-talk measurement. (a) Digitized output of the victim channel, averaged over 41548 cycles of the square waveform. (b) PSD spectra of the aggressor channel (blue curve) and the victim channel (red curve) in log-log scale.	81
5.9	Settling time measurement. (a) a step function input with from 9.5 V to 0 V, and (c) a step function from -9.5 V to 0 V. (b) and (d) are zoomed-in voltage plots around the region of voltage transition on (a) and (c). It takes 3 samples to settle the digitized output to the 22-bit resolution (see (a), (c)), and 760 samples to settle to 24-bit resolution (see (b), (d)).	82
5.10	Common-mode rejection test. (a) Digitized output averaged over 7199 cycles. (b) The PSD spectrum of the output of 10,000 samples. The high and low analog inputs are connected to a common voltage source.	83
5.11	Power supply noise measurement. (a) Digitized data averaged over 4798 cycles. (b) The PSD spectrum of the output (with a terminated input) of 10,000 samples	84

5.12	The non-linearity of the DAQ system as a function of the input voltage. (a) with a 0.01 Hz triangular waveform. (b) with a 0.04 Hz triangular waveform. The maximum non-linearity of the DAQ system is ± 3 ppm over the full input range.	85
5.13	Time trace of the applied HV averaged for 3 hours: (a) positive top of 0.5 kV and (b) negative top of -0.6 kV.	88
5.14	Correlation between the measured leakage current and the applied HV: (a) the measured leakage current as a function of the voltage drift, (b) the estimated voltage drift as a function of the applied HV.	89
5.15	(a) Measured spurious electron EDM as a function of the applied HV. (b) Measured spurious magnetic flux as a function of the applied HV.	90
5.16	Overall schematic of HV polarity switching circuit.	91
5.17	Simplified idea of the feedback circuit.	96
5.18	Overall circuit schematic of feedback circuit.	97
5.19	Photograph of the assembled HV polarity switch system.	99
5.20	Digitized output of drive signal and HV monitor outputs on Ch1 and Ch2, averaged over 35849 cycles.	100
5.21	Time derivative of drive signal and HV monitor outputs on Ch1 and Ch2. Plots in the second row are zoomed-in views.	100
5.22	Source of SQUID baseline jumps. (a) Cryogenic-incompatible HV ca- bles. Many cracks on the cables are observed after several thermal cycles of the system. (b) SQUID baseline jumps at every field reversal.	105
5.23	Examples of the SQUID baseline jumps due to HV discharge. (a) and (b) confirm that the HV discharge is a direct cause of SQUID instabilities.	106
5.24	Insufficient magnetic shielding. (a) Many vibrational peaks are observ- able in the flux noise spectrum of the SQUID sensor. (b) The averaged SQUID signal in time domain over 17278 cycles shows evident vibra- tional signals.	107

5.25	Photographs of two layers of superconducting magnetic shielding. (a) Assembled package of electrodes and GGG samples. (b) First layer of lead shield. (c) One layer of a kapton sheet insulator. (d) Second layer of lead shield.	108
5.26	The magnetic flux noise spectra of the SQUID sensor operated at 4.2 K including the nominal noise spectrum (dashed curve) and the spectrum (solid curve) with an external magnetic applied field of 10 Gauss at 2 Hz.	109
6.1	Schematic of the improved signal readout mechanism in the EDM experiment.	111
6.2	Flowchart to collect the voltage signals: HVs, Leakage currents and SQUID signal.	112
6.3	Time-traces of averaged signals for three hours on one HV monitor, one leakage current monitor, and the SQUID readout presented as two cycles of field reversal. Data were taken using the 24-bit DAQ system, with a sampling rate 715 Hz.	114
6.4	Distribution of the electron EDM observable (processed with the drift-correction algorithm). Data points were collected over one uninterrupted run (3 hours).	117
6.5	SQUID readout (averaged over one non-interrupted run) folded modulo one cycle of field reversal. This data set illustrates the worst case of DC voltage drift.	118
6.6	Results of electron EDM measurements, processed using the fitting algorithm. Each data point is the averaged result of one run. The final data point is the final averaged result over 40 experimental runs. . . .	119
6.7	Measured electron EDM as a function of the applied HV. The data point at 9.4 kV _{pp} contains the highest statistics.	122

7.1	Solutions of the finite-element analysis calculation investigating the effect of the flux pickup coil location. (a) 2-D color-coded filled contour plot of B_z in Tesla along the $y = 0$ plane with the gap size of 0.25 cm. (b) Combination of line scans of B_z along $z=0$ where the pickup coil is placed on the solutions. Red and green dashed lines denote areas of the inner and outer coils of the pickup coil.	130
7.2	Solutions of the finite-element analysis calculation with the different radial dimension of the lead shields. (a) 2-D color-coded filled contour plot of B_z along the $y=0$ plane with the shield diameter of 5.1 cm. (b) Combination of each line scans of B_z along $z=0$ on the solutions. Red and green dashed lines denote areas of the inner and outer coils of the pickup coil.	132
7.3	Solutions of the finite-element analysis calculation with the different sample height. (a) 2-D color-coded filled contour plot of B_z along the $y = 0$ plane with the sample height of 2.3 cm as an example. (b) Combination of each line scans of B_z along $z=0$ on the solutions. Red and green dashed lines denote areas of the inner and outer coils of the pickup coil.	133
7.4	Simplified schematic diagram of the precision DAC board.	136
A.1	AC susceptometer apparatus. (a) schematic of the AC susceptometer design. (b) Photograph of the home-made set of AC susceptometer coils, the primary coil (left) and the pickup coil (right).	140
A.2	The expected axial field profile generated by the primary coil. Two dashed red lines indicate the placement of the primary coil.	142

A.3	AC volume magnetic susceptibility of the GGG sample as a function of temperature, measured at frequencies 1250 Hz (red squares), 830 Hz (blue triangles), and 475 Hz (green diamonds) and temperatures ranging from 1.2 K to 150 mK. The DC susceptibility (black circles) measured at a maximum applied magnetic field of 400 Oe is also displayed together for comparison. The x -axis is in log scale.	145
B.1	A single circular loop carrying a steady current I with a radius of ρ' .	148
B.2	Simplified disk-shaped GGG sample as a stack of three identical current rings with a distance of 0.38 cm between the rings. The flux pickup coil is placed 0.33 cm away from the immediate ring as the actual experimental setup.	149
B.3	Solutions of the simplified analytical model. (a), (b), and (c) show the magnetic induction from each current loop 1, 2, and 3. (d) shows the total induced magnetic field by all current loops normalized by number of loops.	150
B.4	Solutions of the analytical model when the pickup coil is positioned at the center of the sample ($z = 0.71$ cm). (a) and (b) are magnetic inductions by the current loop 2 and current loop 1 or 3, respectively. (c) is the total induced magnetic field by all current loops normalized by number of current loops.	151
B.5	Analytical solutions of the EDM-induced magnetic field with two different positions of the pickup coil. Data points with square dots and circular dots for the pickup coil positioned at $z = 0$ and at the sample center, respectively.	152

Chapter 1

Introduction

In this chapter, the theoretical motivation for and impact of the search for the permanent electric dipole moment (EDM) are described. Several important methods used in the search for the electron EDM are also briefly discussed.

1.1 Overview of the Electric Dipole Moment

1.1.1 What is the Electric Dipole Moment

In the classical picture, an EDM is created when the charge q is separated from a charge $-q$ by a distance \mathbf{r} directed toward the positive charge in the form of $\mathbf{d} \equiv q\mathbf{r}$. With this definition, it seems that a point-like particle such as an electron, the object of attention in this dissertation, cannot have an intrinsic EDM. The solution to this puzzle is given by quantum field theory. Due to vacuum polarization, the electron is surrounded by a cloud of virtual charge fluctuations made of short-lived particle-antiparticle pairs (such as $e^+ - e^-$ and $\mu^+ - \mu^-$ pairs) which are created and then annihilated within the limit of the uncertainty principle as shown in Fig. 1.1. The charged pairs can be aligned into positive and negative regions to give an effective size to define the EDM.

In a non-degenerate ground state with non-zero spin, the EDM vector of the ele-

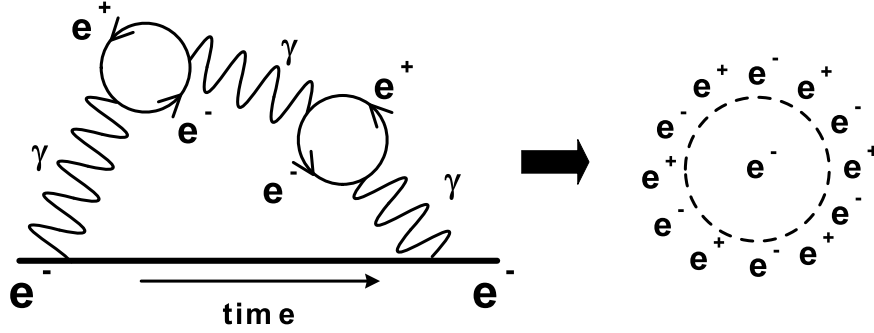


Figure 1.1: Vacuum polarization producing virtual electron-positron pairs around an electron. The electron is dressed by a charge cloud of the pairs.

mentary particle must align with its spin vector since any other direction would cause the system to become degenerate. Only the spin vector can be defined in quantized systems. The constraint on the EDM vector direction can also be understood using the Wigner-Eckart theorem. For a spin $1/2$ particle, the expectation value of the EDM in a non-degenerate ground state is given by $\langle jm | \mathbf{d} | jm \rangle$ in the angular momentum eigenstate $|jm\rangle$ basis. Here the secondary total angular momentum quantum number m is fixed along the z -direction, up or down. Since the EDM operator is a vector operator, \mathbf{d} is a rank-1 spherical tensor T_q^1 for $q = \pm 1$ or 0 . The EDM is defined in terms of the expectation value of $\langle jm | T_q^1 | jm \rangle$. Applying the Wigner-Eckart theorem

$$\langle jm | T_q^1 | jm \rangle = 0 \text{ unless } m = q + m, \quad (1.1)$$

the factor q is required to be zero for the non-zero EDM expectation value where $T_0^1 = d_z^1$. Only the z -direction is allowed for the EDM vector. As a result, the EDM vector is required to be parallel or antiparallel to the spin vector, leading to the form

$$\mathbf{d} = \pm d \frac{\mathbf{S}}{|\mathbf{S}|} \quad (1.2)$$

where \mathbf{S} is the spin vector. The sign of \mathbf{d} remains to be decided experimentally.

$^1T_{\pm 1}^1 = \mp(d_x \pm id_y)/\sqrt{2}$

1.1.2 Violation of Fundamental Discrete Symmetries

The search for the EDM of elementary particles is motivated as a test of the fundamental discrete symmetries assumed in the Standard Model (SM) of particle physics. In physics, the three most important fundamental discrete symmetries are: Charge conjugation (C), Parity-inversion (P), and Time-reversal (T).

The C -symmetry means that a system is invariant under the C transformation which changes the particle in the system into its antiparticle. The C operation changes the sign of all intrinsic additive quantum numbers such as electric charge or baryon number. The sign of spacetime variables such as spin and position, on the other hand, are left intact. One good example showing a consequence of C -conservation is that the π^0 meson decays predominantly ($\sim 98.8\%$) to $\gamma\gamma$, but the decay $\pi^0 \rightarrow \gamma\gamma\gamma$ is not observed. Note that the π^0 and γ have well-defined C values of $+1$ and -1 , respectively.

The P operation inverts the spatial coordinates of a system through the origin: $(x, y, z) \rightarrow (-x, -y, -z)$ or $(r, \theta, \varphi) \rightarrow (r, \pi - \theta, \pi + \varphi)$. Under the P -symmetry, the original system must be indistinguishable from the spatially inverted system.

The T transformation leads to an inversion of the temporal coordinate of a system through the change $t \rightarrow -t$, hence it is also called the motion-reversal transformation. The T -symmetry can be perceived by a simple physical process in which the elastic collision of two balls is identical as when the same process is run backward in time. Contrary to C and P operations, T is represented by an anti-unitary operator with the form $\hat{T} = \hat{U}\hat{K}$ where \hat{U} is a unitary operator and \hat{K} denotes the complex-conjugate operator in the case of a particle without spin. Thus, the time-reversed state $\hat{T}\Psi(\mathbf{r}, t)$ becomes $\Psi^*(\mathbf{r}, -t)$. This can be readily realized employing a single particle time-dependent Schrödinger equation:

$$\hat{H}[\hat{T}\Psi(\mathbf{r}, t)] = \hat{H}\Psi^*(\mathbf{r}, -t) = (-i)\hbar \frac{\partial \Psi^*(\mathbf{r}, -t)}{\partial(-t)} = i\hbar \frac{\partial}{\partial t}[\hat{T}\Psi(\mathbf{r}, t)]. \quad (1.3)$$

The state $\hat{T}\Psi(\mathbf{r}, t)$ is also an eigenstate of the system, resulting in T -invariance. Note

that the Schrödinger equation written only with the substitution $t = -t$ does not derive the result of T -invariance.

Until 1956, it was firmly believed that symmetry invariance is an unbreakable concept since Galileo demonstrated the conservation of energy in his pendulum experiments and constructed the invariance of physical laws under Galilean transformations. Symmetry invariance of physical systems is bound with conservation laws as the famous Noether's theorem states that any continuous symmetry of the action of a physical system has a corresponding conservation law (note that the discrete symmetry in classical mechanics does not lead to conservation laws). For example, conservations of linear momentum and angular momentum result from the fact that the laws of physics remain intact under a translation and rotation of coordinate systems, respectively. The concept of symmetry invariance became more cherished after development of electromagnetism, quantum mechanics, relativity theories and the modern SM, all based on the gauge invariance. The P -conservation in quantum mechanics, as another example, comes from the P -symmetry invariance between the left and right hands. Physicists have believed that the P -conservation held for all physical systems.

In the mid-twentieth century, T. D. Lee and C. N. Yang came up with a startling prediction which would demolish the most fundamental conservation law. Before presenting their far-reaching suggestion, they worked together to make clear the $\theta - \tau$ puzzle [1]. The puzzle argued that the charged θ and τ mesons (they have experimentally identical mass, lifetime, and spin) could not be the same particle if the P -symmetry is conserved during their weak decays because the θ disintegrated into two π mesons, leading to the parity of θ of $+1$, while the τ disintegrated into three π mesons, leading to the parity of τ of -1 , according to Laporte's rule [2]. In 1956, Lee and Yang, motivated by the question that the long-held P -conservation would be violated by the weak interactions, critically asked again "what is the existing experimental support for P -conservation in the weak interaction" and suggested various

possible direct experiments in beta decays, strange-particle decays, and meson decays, all of which could provide necessary evidence for conservation or non-conservation of parity [3].

Some astonishment came about when the P -symmetry was explicitly shown to be broken in the beta decay of ^{60}Co ($^{60}_{27}\text{Co} \rightarrow ^{60}_{28}\text{Ni}^* + e^- + \bar{\nu}_e$ followed by $^{60}_{28}\text{Ni}^* \rightarrow ^{60}_{28}\text{Ni}^* + \gamma(1.17 \text{ MeV}) + \gamma(1.33 \text{ MeV})$) by C. S. Wu and her collaborators [4] one year after the question of P -conservation. They were the first experimental group that performed an experiment in beta decay to prove the P -violation suggested by Lee and Yang. They measured the angular distribution of the electrons (beta rays) coming from beta decays of polarized ^{60}Co nuclei by an external applied magnetic field at low temperatures. The measurement found a large beta asymmetry in the distribution for the applied field pointing up and down, indicating unambiguous evidence of P -violation in beta decay. More observations of the failure of P -invariance were observed by R. L. Garwin *et al.* in the π and μ meson decays [5], also proposed by Lee and Yang.

While the phenomenon of P -violation is firmly established in numerous weak-decay experiments, T -violation has only been observed directly in the neutral-kaon system by the CPLEAR collaboration in 1998 [6]. The CPLEAR experiment measured a difference between the probability that $K_{t=0}^0 \rightarrow \bar{K}_{t=\tau}^0$ and the probability that $\bar{K}_{t=0}^0 \rightarrow K_{t=\tau}^0$. The first K meson transformation is in the forward time direction and the second one is in the backward time direction. The two possible Feynman diagrams of these K meson transformations are shown in Fig. 1.2. Under T -invariance, no difference between the probabilities should be measured. The result of the experiment, however, showed the average decay-rate asymmetry of $\left\langle \frac{R(\bar{K}_{t=0}^0 \rightarrow K_{t=\tau}^0) - R(K_{t=0}^0 \rightarrow \bar{K}_{t=\tau}^0)}{R(\bar{K}_{t=0}^0 \rightarrow K_{t=\tau}^0) + R(K_{t=0}^0 \rightarrow \bar{K}_{t=\tau}^0)} \right\rangle = (6.6 \pm 1.3_{\text{stat.}} \pm 1.0_{\text{syst.}}) \times 10^{-3}$, giving unequivocal evidence of T -violation. In addition, more searches for direct evidence of T -violation are underway in the B meson system [7].

To quantify the violation of physical laws under P and T , outside the scope of

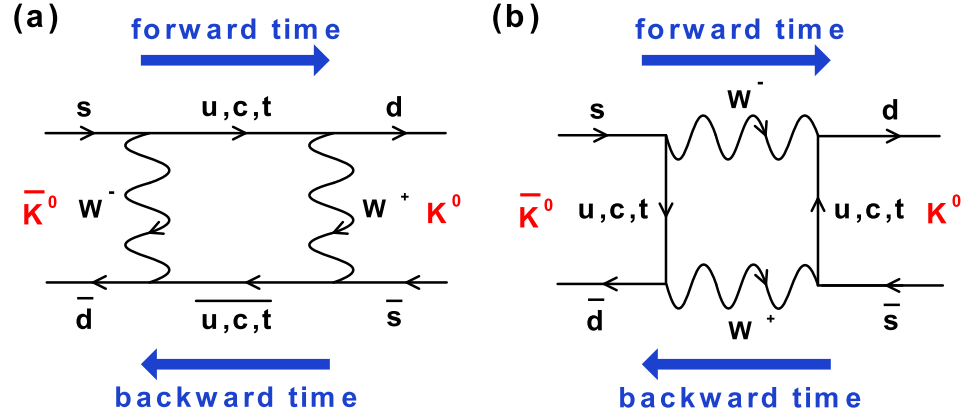


Figure 1.2: Two Feynman diagrams, (a) and (b), for K mesons oscillations via the weak interaction in SM.

weak decays, a measurement of the EDM of elementary particles with spins was first carried out by Purcell and Ramsey in 1950 [8]. On account of the different transformation properties of the EDM (a polar vector) and the spin (a pseudo-vector), the fundamental physical laws that govern an elementary particle must violate both T and P -symmetries for it to acquire an EDM. For example, the mathematical proof that T -invariance forbids the existence of the EDM of the particles is as follows. Under a T transformation, the EDM \mathbf{d} is T -even while the spin \mathbf{S} is T -odd: $\hat{T}\mathbf{d}\hat{T}^{-1} = \mathbf{d}$ and $\hat{T}\mathbf{S}\hat{T}^{-1} = -\mathbf{S}$. With these transformations, the expectation value of the EDM after the T transformation is written

$$\langle jm | \hat{T}^{-1} \mathbf{d} \hat{T} | jm \rangle = \langle jm | \mathbf{d} | jm \rangle. \quad (1.4)$$

Eq. 1.2 leaves another form of Eq. 1.4

$$\begin{aligned} \langle jm | \hat{T}^{-1} \mathbf{d} \hat{T} | jm \rangle &= \langle jm | \hat{T}^{-1} \left(\pm \frac{d}{|\mathbf{S}|} \mathbf{S} \right) \hat{T} | jm \rangle \\ &= \langle jm | \pm \frac{d}{|\mathbf{S}|} (-\mathbf{S}) | jm \rangle \\ &= -\langle jm | \mathbf{d} | jm \rangle. \end{aligned} \quad (1.5)$$

The two equations above result in $\langle jm | \mathbf{d} | jm \rangle = 0$ if T -symmetry is a good symmetry.

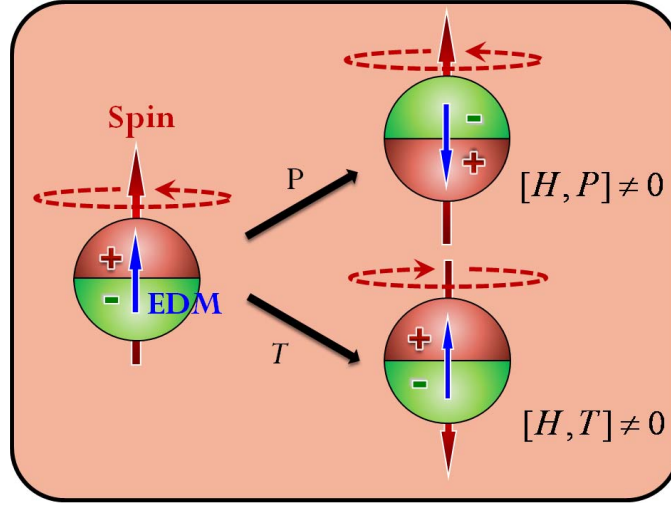


Figure 1.3: Violation of P - and T -symmetries resulting from the existence of the EDM in an elementary particle.

In other words, a non-zero EDM implies T -violation.

Pictorially, Fig. 1.3 shows a particle with both spin and EDM in the same direction. Under a T transformation its spin is reversed while its EDM is invariant. On the other hand, under a P transformation its spin is invariant while its EDM is reversed. Hence T - and P -invariance each make the particle system two-fold degenerate: $|\mathbf{d} \uparrow \mathbf{S} \uparrow\rangle$ and $|\mathbf{d} \uparrow \mathbf{S} \downarrow\rangle$ or $|\mathbf{d} \downarrow \mathbf{S} \uparrow\rangle$. Since such degeneracy is not allowed in the elementary particle system the existence of EDM violates T - and P -symmetries.

The Hamiltonian of the particle system with interactions with electric and magnetic fields is written $H = -\mathbf{d} \cdot \mathbf{E} - \boldsymbol{\mu} \cdot \mathbf{B}$ where $\boldsymbol{\mu}$ is the magnetic dipole moment of the particle. The $\boldsymbol{\mu}$ is created by the particle's spin, thereby the simple relation $\boldsymbol{\mu} = \alpha \mathbf{S}$ can be used where α is proportional to the gyromagnetic ratio. Substituting Eq. 1.2 to the Hamiltonian gives $H = -(\pm d/|\mathbf{S}|)\mathbf{S} \cdot \mathbf{E} - \alpha \mathbf{S} \cdot \mathbf{B}$. Under the T -transformation the Hamiltonian is found not to be invariant owing to

$$\begin{aligned} \hat{T}^{-1} H \hat{T} &= (\pm d/|\mathbf{S}|)\mathbf{S} \cdot \mathbf{E} - \alpha \mathbf{S} \cdot \mathbf{B} \\ &\neq H \end{aligned} \tag{1.6}$$

where \mathbf{E} is T-even and \mathbf{B} is T-odd. Consequently, $[H, T] \neq 0$, resulting in T -violation in the system. In the same manner, it can be shown that $[H, P] \neq 0$, leading to P -non-conservation in the system. As a result, the studies of EDM would provide crucial information about the nature of the less well-understood T -violation.

For decades, EDM searches in elementary particles have been performed using different experimental techniques. None of the experimental efforts, however, has yielded positive results as of today. The elusive nature of the EDM might be closely related to the EDM property of T -violation indicating that a physical reaction could happen at a different rate when played backward in time. The physics of T -violation is often linked, via the CPT theorem², to the violation of the combined C and P symmetries, CP , and vice versa. As a result, the outcome of the EDM search could imply another source of CP -violation which is a necessary feature to explain the unsolved mystery of the matter and anti-matter disparity of our Universe [9].

Most weak interactions have preserved CP -symmetry as opposed to C and P individually, however CP -violation was first discovered by J. W. Cronin *et al.* in the $K^0 - \bar{K}^0$ meson decay in 1964 [10]. They found that one CP eigenstate, $|K_2\rangle = \frac{1}{\sqrt{2}}(|K^0\rangle - |\bar{K}^0\rangle)$, of linear combinations of $|K^0\rangle$ and $|\bar{K}^0\rangle$ decays into two pions with a rate of $\sim 0.2\%$. This decay mode violates CP -symmetry because CP of $|K_2\rangle$ is -1 while that of two pions is $+1$. Another indication of CP -violation in the same system of K mesons was announced in 1999 [11]. Beyond the neutral K meson system, more evidence of CP -violation was observed in the $B^0 - \bar{B}^0$ meson decay in 2001 [12, 13].

The EDM measurements could be the key understanding the mysteries of CP -violation phenomena. In particular, CP - as well as T -violating interactions can be induced by complex number phases [14]. To understand that, recall Eq. 1.3. The Schrödinger equation does not lead to T -invariance if the potential term V on the

²The CPT theorem implies that, for example, when a moving particle is changed into its anti-particle (C) and its mirror image (P), and moved in the reversed direction in time (T), the resulting particle is indistinguishable from the original one. The CPT -symmetry is believed to be conserved due to local Lorentz symmetry [18] and no experimental evidence of CPT -violation has been found.

Hamiltonian of a particle system is complex: $V = |V|e^{i\delta}$ where δ is a phase angle. The phase angle in the system quantifies the degree of T -violation.

1.1.3 Theoretical Model Prediction for the Electron EDM

Over the years, various theoretical models emerged to supply sources of CP -violation that lead to a sizable electron EDM prediction [15]. The only confirmed source of CP -violation in the SM is the complex phase ($e^{i\delta}$) of the CKM matrix [16, 17] that describes the quark mixing in charged-current weak interactions. The phase angle δ , responsible for all CP -violating interactions in the SM, was proposed to explain the CP -violating K meson decays and confirmed by the experiment on the B meson system [18]. The CKM phase manifests the electron EDM (d_e) through high-order loop (at least four-loop) couplings that involve flavor-changing quark interactions with the exchange of W^\pm weak bosons [19]. The low-loop diagram cannot induce the electron EDM due to zero net CP -violating phase. For example, in an one-loop diagram the complex phases for emission and reabsorption of a W weak boson are $e^{i\delta}$ and $e^{-i\delta}$ respectively, leading to no CP violation [14]. As a result, the size of the electron EDM predicted within the framework of the SM is extremely small, $|d_e| < 10^{-38}$ e·cm, well beyond the reach of current experimental techniques. The current experimental upper bound is established using cold polar YbF molecules with a sensitivity of 1.1×10^{-27} e·cm [20].

The degree of CP -violation in the SM, however, is not sufficient to account for the observed baryon asymmetry in the universe. At present, extensive studies in high energy experiments are underway to search for more sources of CP -violation besides the CKM matrix source. New physics models beyond the SM (supersymmetry (SUSY), left-right symmetry, multi-Higgs, etc) introduce new sources of CP -violation that often lead to a sizable electron EDM [15, 21]. That is possible because the models contain additional forces and particles that can generate new complex phases. In particular, some variants of the naive SUSY model can generate an electron EDM

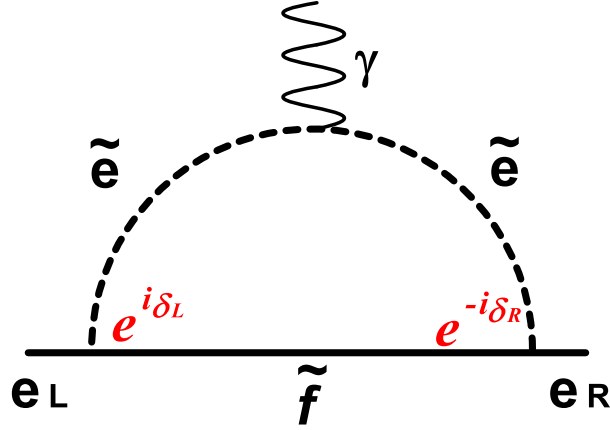


Figure 1.4: One-loop electron EDM contribution in the SUSY model. \tilde{e} is a scalar electron and \tilde{f} is a neutralino.

comparable to the current experimental limit (note that the naive SUSY model predicts d_e at the level of 10^{-25} e·cm and has been almost excluded by the current experimental limit [22]). The SUSY models are very popular among physicists because they can explain the gauge hierarchy problem that the SM does not solve, provide a candidate for Dark Matter, etc. The SUSY models double the number of particles by introducing hypothetical massive superpartners for every observed particle; supersymmetric bosonic partner for each observed fermion (slepton \leftrightarrow lepton, squark \leftrightarrow quark) and supersymmetric fermionic partner for each gauge boson (photino \leftrightarrow photon, gluinos \leftrightarrow gluon, zino \leftrightarrow Z^0 , winos \leftrightarrow W^\pm). Fig. 1.4 shows the one-loop diagram which generates the electron EDM in SUSY. The complex phases, $e^{i\delta_L}$ and $e^{-i\delta_R}$, related to emission and reabsorption of the scalar electron (selectron with zero spin) are allowed to differ if the electron changes its handedness. This results in a non-vanishing CP -violating effect in the one-loop diagram which could give rise to a large electron EDM on the order of $10^{-27} - 10^{-29}$ e·cm.

The electron in Fig. 1.4 can be regarded as a charge cloud composed of short-lived particle-antiparticle pairs. Every once in a while, new massive particle-antiparticle

pairs (spin-zero supersymmetric bosons) that have never been experimentally observed could appear out of the vacuum momentarily and only leave their footprints through their new CP -violating interactions with electrons and quarks that shape the electron EDM. The electron EDM arising from the new CP -violating interactions is suggested to be scaled with the $1/M_{\text{new-physics}}^2$ factor [14, 23]. Here $M_{\text{new-physics}}$ is the mass of the new particle. The discovery of an electron EDM in next generation experiments would suggest that there exists new physics beyond the SM at energy scales higher than tens of TeV [23], and could provide information complementary to results from high-energy collider experiments on the nature of symmetry breaking.

Free from the SM backgrounds, the measurement of EDMs presents a powerful tool for global tests on many theoretical extensions to the SM. For example, the variants of the SUSY model will be put to stringent tests as the next generation of experiments improves the sensitivity by another factor of 100. EDM measurements have ruled out more theoretical models than any other experiment in the history of physics [18], even though none of the experimental efforts have yielded positive results. With more refined experimental techniques, EDM searches continue to be of fundamental significance in particle and nuclear physics [14, 24].

1.2 Methods Used for the Electron EDM Search

Measurements of intrinsic EDMs of elementary particles use different experimental techniques, often with low energy systems, to probe the physics of T - and CP -violation as precision test of the SM. The experimental methods involve atomic systems (Tl, Cs, or Fr), polar heavy atom molecules (YbF, PbO, or TlF), and solid state techniques ($\text{Gd}_3\text{Fe}_5\text{O}_{12}$ or $\text{Gd}_3\text{Ga}_5\text{O}_{12}$). Over the decades, each experiment has steadily increased the sensitivity of the electron EDM. The best experimental limit on the electron EDM was held by the Berkeley experiment with a thallium atomic beam [25] until the first half of 2011. Another experiment using the polar molecule

YbF at Imperial College, London has recently reported an improved experimental limit by a factor of 1.5 [20]. Another possible enhancement on the experimental limit could be achieved using solid state experiments [26, 27]. In this section, several important experiments out of a number of experimental EDM searches are discussed in detail.

1.2.1 Thallium Atomic Beam EDM Experiment

The thallium EDM experiment [25] measures the spin precession frequency as an electron EDM signal when the electron is subjected to a strong electric field parallel or antiparallel with a weak magnetic field. The heavy paramagnetic Tl atoms lead to the enhanced electron EDM with the form of Rd_e where R is generally called as the EDM enhancement factor. The factor of R for Tl atoms is estimated to be -585 by theoretical calculations in many-body perturbation theory [28]. The experiment employs two pairs (up/down beams and left/right beams) of counterpropagating vertical thermal Tl atomic beams (~ 970 K) separated by 2.54 cm. This method is expected to effectively control the leading systematic effect of motional magnetic fields (\mathbf{B}_m): $\mathbf{B}_m \sim \mathbf{E} \times \boldsymbol{\nu}$ where $\boldsymbol{\nu}$ is the velocity of the atom. The \mathbf{B}_m can be canceled out between up- and down-directed beams. The flux of Tl atoms is measured to be 10^{17} atoms/s.

To detect the tiny electron EDM signal, the experiment uses nuclear magnetic resonance with the separated oscillating radio-frequency (RF) fields method pioneered by Ramsey [29]. The separated Tl atomic beams are first polarized by laser optical pumping and then their polarization is rotated by 90 degrees by a RF field. The pairs of polarized beams each pass between electric field plates (with 1 m length and 2.3 cm thickness), leading to the interaction energy $-\mathbf{d} \cdot \mathbf{E}$. The two separate electric field regions generate identical high electric fields of 120 kV/cm with a gap size of 2 mm, but in opposite directions. In those regions, a weak magnetic field aligned with the electric fields is also present to provide an additional energy $-\boldsymbol{\mu} \cdot \mathbf{B}$. This method

provides common-mode noise rejection and control of some systematic effects. In this field stage the spins are precessed. Another RF field, coherent with the first one with a relative phase difference, rotates their polarization back to the original direction after the field regions. In the final analysis stage, the same laser used in the initial stage probes the atoms to measure the shift of spin precession frequency.

Based on the interaction energy with the electric and magnetic fields, an energy difference between the spin states parallel and antiparallel to the fields can be written $\hbar\omega = 2\mu B \pm 2dE$ assuming that \mathbf{B} is parallel to \mathbf{E} . Here ω is the spin precession frequency and the \pm sign arises from Eq. 1.2. Reversing the direction of the electric field results in switching only the sign of \mathbf{E} , hence the magnetic term can be offset by subtracting the precession frequencies measured in each case. As a result, the shift of the precession frequency is $\Delta\omega = 4dE/\hbar$. The electron EDM signal can be extracted from the frequency measurements.

As stated before, the leading systematic effect in this experiment is the motional magnetic fields. With a slight misalignment between the magnetic and electric fields, the motional field is added to the magnetic field, leading to an asymmetry in the magnetic field strength upon the reversals of the electric field. Accordingly, the motional field changes the spin precession frequency and mimics the EDM signal. This systematic effect is currently limiting the sensitivity of the thallium EDM experiment. The final result reported the experimental limit of $|d_e| \leq 1.6 \times 10^{-27} \text{ e}\cdot\text{cm}$ [25].

1.2.2 The EDM Experiment in the Polar Molecule YbF

The EDM search using the YbF polar molecule at Imperial College London [20] is another promising experiment to enhance the EDM sensitivity. The YbF molecule has two prominent experimental advantages, making it possible to improve over the Tl experiment. One advantage is that the EDM interaction energy of YbF is enhanced by a factor of 220 compared to that of Tl because of its large internal electric fields. The other is that the leading systematic effect of the motional magnetic field that

limits the Tl experiment is negligible in the YbF experiment.

In this experiment, the polar molecule YbF beams are emitted by a source. Since Yb and F atoms have a nuclear spin of 0 and 1/2 respectively, the system has the $F = 1$ and $F = 0$ hyperfine levels of the ground state that are separated by 170 MHz. The molecular beams first pass through the laser optical pumping region in which all $F = 1$ ground state molecules are eliminated and only $F = 0$ ground state molecules remain. The polarized beams enter the RF region where a static electric field of 3.3 kV/cm and a 170 MHz RF magnetic field vertical to the electric field are present. In this region, the $F = 0$ ground state $|F = 0, m_F = 0\rangle$ is excited to the superposition state $|\psi\rangle = \frac{1}{\sqrt{2}}(|1, 1\rangle + |1, -1\rangle)$. After the RF region, the beams enter a region with a pair of electric field plates of 65 cm length where there are static strong electric (8.3 kV/cm) and weak magnetic fields in parallel. The molecules are moving for a time τ in this region and the two parts of superposition state develop a relative phase shift $2\phi = 2(\mu_B B - d_e E_{\text{eff}})\tau/\hbar$ where μ_B is the Bohr magneton through the interaction with the fields. The effective internal field E_{eff} is estimated to be 13 GV/cm under the applied field of 8.3 kV/cm, confirming the great enhancement of the EDM signal in this system. Another RF region after the field region drives the excited state back to the $F = 0$ ground state with phase shift $0.5(e^{i\phi} + e^{-i\phi})|0, 0\rangle$. Due to the developed phase shift, the final population of the $F = 0$ molecules is a function of $\cos^2 \phi$. At the final stage, the YbF molecule beams are probed using a fluorescence detector in order to scan the phase shift.

With the usual approach where the applied electric field is reversed, the magnetic interaction term can be canceled out. As a result, the electron EDM signal is extracted by the physical observable $\Delta\phi = 4d_e E_{\text{eff}}\tau/\hbar$. A possible systematic effect is the motional magnetic field. This field, however, is greatly suppressed because of the large tensor Stark splitting of the $F = 0$ state. The experiment has finally reported the improved experimental limit of $|d_e| \leq 10.5 \times 10^{-28}$ e-cm.

1.2.3 The EDM Experiment Using Gadolinium Iron Garnet

Beyond atomic and molecular experiments, a different type of EDM experiment using a solid state system has been accomplished by L. Hunter and colleagues at Amherst College with a reasonable result [30] (this dissertation will report a complementary EDM experiment in $\text{Gd}_3\text{Ga}_5\text{O}_{12}$). The experiment uses a macroscopic solid state sample of $\text{Gd}_3\text{Fe}_5\text{O}_{12}$ (GdIG) insulator. There are remarkable features in such a solid state EDM experiment. (1) High number density of gadolinium ions containing unpaired electrons on the order of $\sim 10^{22}/\text{cm}^3$ (atomic experiments have $10^8 \sim 10^{16}$ particles during the measurements), leading to great improvement in EDM sensitivity. (2) The electrons are confined in the solid, thereby the experiment is free of the leading systematic of the motional magnetic field. (3) The applied electric field (magnetic field) induces bulk magnetization (electric polarization) in the solid.

In the experiment, the GdIG sample is exposed to a strong external magnetic field, causing substantial spin polarization inside the sample. Because of Eq. 1.2, the spin polarization leads to volume electric charge polarization inside the sample that produces a voltage across the sample. The resulting induced electric field in the sample is written in the form $E = 0.7 \times 10^{-10} (d_e / 10^{-27} \text{e} \cdot \text{cm}) \text{ V/cm}$. A reversal of the applied magnetic field is used to extract the electron EDM signal from the electric field measurement. This experiment, however, suffers from a large spurious EDM signal resulting from a component of magnetization that does not reverse with the applied magnetic field, the so-called M -even effect [30].

The experiment has reported the experimental limit of $|d_e| < 5 \times 10^{-24} \text{ e} \cdot \text{cm}$ in 2005. The solid state experiment can be improved using another garnet sample, $\text{Gd}_3\text{Ga}_5\text{O}_{12}$, of interest in this dissertation. The expected experimental limit in the solid state EDM experiment could be on the order of $10^{-30} \text{ e} \cdot \text{cm}$ [26].

Chapter 2

Experimental Approach

The leading experimental technique used to measure an EDM is based on nuclear magnetic resonance: EDM interactions induce a shift in the Larmor precession frequency when the fermion is under an externally applied electric field, parallel or anti-parallel to a weak magnetic field. In an attempt to improve the current experimental limit on the electron EDM, an alternative approach using a non-conventional solid-state technique has been designed. The realization of this unique approach could open a new prospect in the field of precision measurements and fundamental symmetry tests. This chapter is dedicated to describing in detail the solid-state method in the search for the electron EDM.

2.1 New Approach Using a Solid State Technique

2.1.1 First Proposal

The idea of employing the solid-state system to search for the electron EDM was first proposed by Shapiro in 1968 [31]. With the application of a strong electric field to a paramagnetic insulator at low temperatures, the EDMs of unpaired valence electrons inside the solid align with the electric field. Because the EDM vector is bound to the direction of the spin vector, a non-zero net EDM alignment results in a net spin

polarization in the sample. The spin ordering generates a small, but non-zero bulk magnetization which produces a magnetic field surrounding the paramagnet. Even though the energy shift predicted from the EDM coupling for individual electrons ($\Delta\epsilon \sim 10^{-23}$ eV) is much smaller than the thermal energy ($k_B T \sim 10^{-6}$ eV), the cumulative effect from the large number of electrons in a solid sample can lead to a magnetization equivalent to a few million Bohr magnetons (details in Sec. 2.2.1). This EDM-induced magnetization manifested by the Stark-aligned electron EDM can be detected using very sensitive magnetometry such as a superconducting quantum interference device (SQUID) inductively coupled to a flux pickup coil around the solid sample.

Direct measurement of the electron EDM would be impractical because an electric field accelerates the charged electrons out of the experiment. In order to address this difficulty, the atomic EDM of neutral atoms is measured instead. The atomic EDM can be understood to inherit the free electron EDM. Analogous to the Schiff theorem [32], an applied field is completely shielded inside a crystal because the constituents of the crystal can rearrange themselves. There exists no internal electric field inside the crystal and electron EDM interactions could not be observed. Due to relativistic effects, however, the electrons in high atomic shells experience an enhanced electric field and the atomic EDM of large Z atoms would have an EDM that scales with Z^3 , where Z is the atomic number, larger than the EDM of the bare electron [33]. For this reason the sample used in the solid-state technique is a paramagnetic insulator containing high Z elements as well as many unpaired valence spins which can enhance the EDM sensitivity. In this experiment, we chose a Gadolinium Gallium Garnet ($\text{Gd}_3\text{Ga}_5\text{O}_{12}$, GGG) paramagnet. In addition to the enhanced EDM, using the solid sample also eliminates a common systematic effect experienced by beam experiments [25], related to the motional magnetic field ($\sim \mathbf{v} \times \mathbf{E}$), because the atoms are trapped inside the solid structure.

2.1.2 First Proposal in Gadolinium Gallium Garnet

The use of GGG for the magnetization-type electron EDM search was first put forward by Lamoreaux [26] and realized by Liu [27]. According to Lamoreaux's proposal, the EDM-induced magnetic flux Φ_e scales with the magnetic susceptibility χ of GGG, the sample area A , the atomic EDM d_a , and the internal electric field E_{int} inside the sample:

$$\Phi_e = \frac{\chi d_a E_{int}}{\mu_a} A \quad (2.1)$$

where μ_a is the atomic magnetic moment. Because the Stark-induced spin polarization increases as the sample temperature decreases, due to the suppression of thermal fluctuations in GGG, the experiment is planned to operate at low temperatures. With a realizable sample size of 100 cm^2 in a strong sustainable applied electric field of 10 kV/cm at an extremely low temperature of 10 mK , the EDM-induced magnetic flux per electron EDM of $10^{-27} \text{ e}\cdot\text{cm}$ is predicted to be $17 \mu\Phi_0$, where Φ_0 is the magnetic flux quantum with a magnitude of $2.07 \times 10^{-15} \text{ T}\cdot\text{m}^2$. For simplicity, the enhancement on the atomic EDM is neglected here: $d_a E_{int} = d_e E_{ext}$ where d_e is the electron EDM and E_{ext} is the applied electric field. In addition, χ follows the typical paramagnetic property (see Ch. 3).

The state-of-the-art modern SQUID magnetometers yield a magnetic flux noise of

$$\delta\Phi_{sq} = 0.2\mu\Phi_0/\sqrt{t} \quad (2.2)$$

where t is the measurement time in seconds. It is immediately obvious that a longer integration time means a reduction of random noise. Since the EDM sensitivity is dominated by SQUID sensor noise, it is possible to estimate the experimental limit to the electron EDM δd_e by

$$\begin{aligned} \delta d_e &= \left(\frac{0.2\mu\Phi_0/\sqrt{t}}{17\mu\Phi_0 \times 0.017} \right) \times 10^{-27} \text{ e}\cdot\text{cm} \\ &= (0.7/\sqrt{t}) \times 10^{-27} \text{ e}\cdot\text{cm} . \end{aligned} \quad (2.3)$$

Here it is assumed that the SQUID sensor measures 1.7 % of the actual flux produced by the sample, which is typical in this type of SQUID-based measurement.

In 10 days of data averaging, the simple estimation leads to the EDM experimental limit of 10^{-30} e·cm, which is a factor of 1000 better than the current best limit [20]. As a result, the GGG-based EDM search has the potential for improving the current sensitivity and providing the fundamental physics with a major impact. Ideally, the GGG-based experiment has to be performed in an environment free of magnetic fields because the spin coupling induced by the magnetic field would certainly dominate over the small electron EDM interaction. In practice, even with the most hermetic magnetic shielding, some residual fields are inevitable around the sample. Thus the EDM experiment needs to be carried out in AC mode, in which the change of EDM-induced magnetization upon the reversal of the electric field is measured. Unfortunately, during the required field reversal, transient currents create a magnetic field that also flips its direction. The transient field diminishes quickly, but the presence of hysteresis effects that lead to finite remnant magnetization (with long relaxation time) inside the sample would be detrimental to the successful realization of this solid state technique at the proposed sensitivity level. As a measure against possible systematic effects arising from ferromagnetic materials we use the paramagnetic garnet, as opposed to gadolinium iron garnet, even though the latter has a much higher magnetic susceptibility [34].

2.2 Choice of a Material

The first electron EDM search using the solid state technique was performed in nickel zinc ferrite at a temperature of 4.2 K in 1978 [35] in which the Fe^{3+} ion has unpaired electrons. However, the experiment obtained a low EDM sensitivity, on the order of 10^{-22} e·cm. Due to the low atomic number of the Fe ion ($Z = 26$), the overall atomic EDM is very small. The spontaneous magnetization and low dielectric strength (\sim

2kV/cm) also limit EDM sensitivity in the ferrite sample. Furthermore, the rf-SQUID magnetometer used in that experiment offered a low flux sensitivity. A decade later, a possible paramagnetic material EuS was suggested for the solid state technique [36], but this solid was also shown to be incompatible with the requirement of strong electric fields because of its low resistivity, $\sim 10^3 \Omega\cdot\text{cm}$ [37], (i.e., large leakage currents which result in serious systematic effects). In contrast, the GGG material contains suitable features for the solid state EDM search and they are described in the next section.

2.2.1 Properties of GGG

The GGG material is advantageous for its high number density of Gd^{3+} ions ($\sim 10^{22}/\text{cm}^3$), each containing seven unpaired electrons on the half-filled $4f$ shell. This leads to a strong magnetic response in a bulk sample. The ground state electronic configuration of the Gd^{3+} ion in GGG is $[\text{Xe}]4f^75d^06s^0$ (recall $[\text{Xe}]4f^75d^16s^2$ for Gd atom). Since the other ions of Ga^{3+} ($3d^{10}4s^04p^0$) and O^{2-} ($1s^22s^22p^6$) have complete closed electron shells, the Gd^{3+} ion determines all the magnetic properties of GGG. In addition, GGG possesses a superb dielectric strength of 10 MV/cm and a high electrical resistivity (volume resistivity higher than $10^{16} \Omega\cdot\text{cm}$ below 77 K) that allows it to withstand a strong electric field with sufficiently small leakage currents.

Due to the small energy of electron EDM interactions, the induced magnetic field is minute. However, with EDMs near the present experimental limit, the accumulated magnetic signal from the large number of electrons inside the GGG sample could lead to a sizable magnetic signal above the background. With an internal electric field E_{int} of 10 kV/cm and the present upper limit for the electron EDM ($d_e \sim 10^{-27} \text{ e}\cdot\text{cm}$), the EDM interaction energy $\Delta\epsilon$ is given by

$$\Delta\epsilon = d_e E_{int} = 10^{-23} \text{ eV} . \quad (2.4)$$

The thermal energy is $k_B T = 8.6 \times 10^{-7} \text{ eV}$ at a desired temperature of 10 mK, where

k_B is the Boltzmann constant. The degree of EDM-induced magnetization for each Gd^{3+} ion with the magnetic moment $\mu_a = 7.94\mu_B$ is washed out by the thermal fluctuation:

$$M_{EDM} = \mu_a d_e E_{int} / k_B T \simeq 10^{-16} \mu_B \quad (2.5)$$

where μ_B is the Bohr magneton. On the other hand, the large number of Gd^{3+} ions in the GGG solid results in a bulk magnetization¹ of

$$M_{\text{Bulk}} = 10^{22} \text{cm}^{-3} \times M_{EDM} \simeq 10^6 \mu_B / \text{cm}^3 \quad (2.6)$$

which leads to a net magnetic field of 10^{-17} T ($\mu_0 M_{\text{Bulk}}$), high enough to be detected using the SQUID magnetometer.

2.2.2 Structure Details of GGG

The GGG belongs to the garnet family [38] with a general structure of $\{A_3\}[B_2](C_3)\text{O}_{12}$, where A denotes triply-ionized metallic ions, M^{3+} , on a {dodecahedral} lattice, B and C are ions on a [octahedral] and (tetrahedral) lattice, respectively. Oxygen ions, O^{2-} , form a cage around the ions and balance the charge. In general, the couplings between these sub-lattices are antiferromagnetic. The A , B , and C terms can be substituted by many different metallic elements, with varying degrees of magnetism, leading to a wealth of possible magnetic properties that change with temperature. The rare-earth elements², which are of interest to the electron EDM search, can occupy the A sites. As mentioned before, the EDM of paramagnetic atoms (ions) is enhanced by Z^3 , thus the electron EDM of the Gd^{3+} ion ($Z = 64$) dominates over that of the Ga^{3+} ($Z = 31$) and O^{2-} ($Z = 8$). Non-magnetic Ga^{3+} ions populate the B and C sites, leaving the

¹The EDM interaction energy level per Gd^{3+} ion is $H_{EDM} = -d_e E_{int}$. Note that the non-relativistic Hamiltonian is taken into account. The resulting magnetization per unit volume in thermal equilibrium is $\langle M \rangle = N\mu_a [(e^x - e^{-x}) / (e^x + e^{-x})] = N\mu_a \tanh x$, where $x = d_e E_{int} / k_B T$. For $d_e E_{int} \ll k_B T$, $\langle M \rangle = N\mu_a (d_e E_{int} / k_B T)$.

²Most rare-earth ions (from Ce^{3+} to Yb^{3+} in the periodic table) have similar chemical properties determined by the unpaired $4f$ shell electrons and they generally yield paramagnetic behavior.

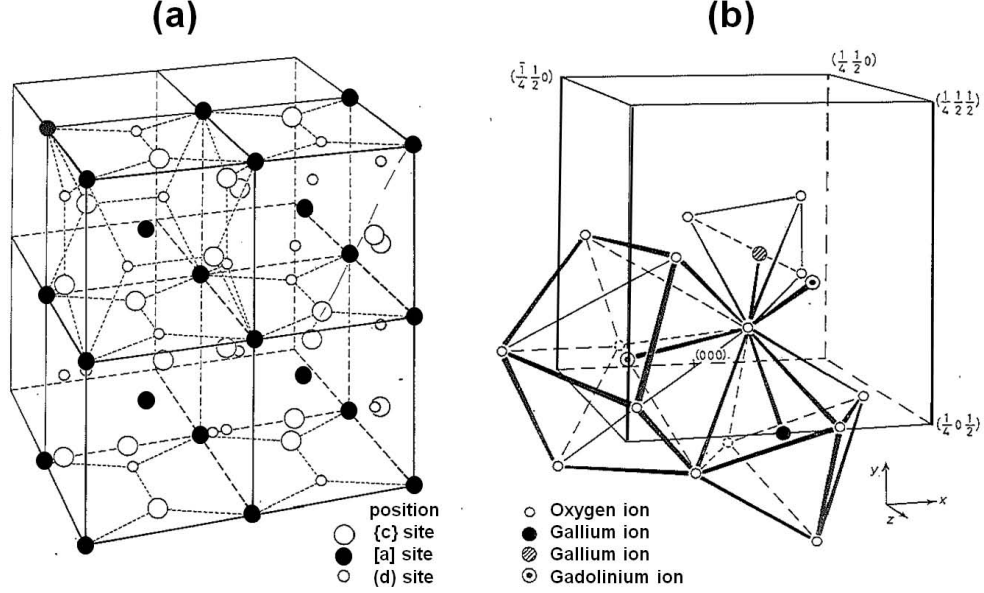


Figure 2.1: The garnet structure of GGG. (a) The unit cell of GGG which contains 24 Gd^{3+} at {c} site (dodecahedral structure), 16 Ga^{3+} at [a] site (octahedron structure), and 24 Ga^{3+} at (d) site (tetrahedron). No oxygen ions are shown. (b) Detailed sub lattices of cations related to neighbor oxygen ions. The figures adapted from Ref. [39].

magnetic property of GGG to be determined solely by the spin interactions of the Gd^{3+} ions on the dodecahedral lattice. The rare-earth ion Gd^{3+} has total orbital angular momentum $L = 0$ and total spin $S = 7/2$. Therefore, the magnetic moment of the Gd^{3+} ion is only given by the spins and expressed by $\mu_a = g\sqrt{J(J+1)}\mu_B = 7.94\mu_B$ with the spectroscopic splitting factor $g = 2$ and $J = 7/2$. Since $L = 0$, the spin-orbit interaction is negligible and it is easy to magnetize the material. In other words, the spin anisotropy is very weak in this material.

This rare-earth paramagnetic garnet GGG has a cubic crystal system and crystallizes in $Ia3d$ space group [39]. Fig 2.1 displays the garnet crystalline structure of GGG. As seen in the figure, there are 24 Gd^{3+} ions at dodecahedral sites (c site) associated with 8 neighboring O^{2-} ions. There are 24 and 16 Ga^{3+} ions at tetrahedron

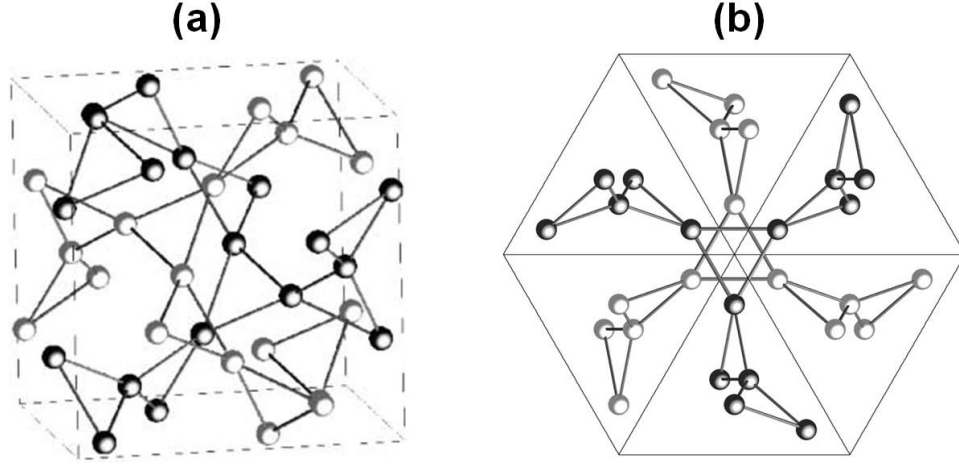


Figure 2.2: Positions of the Gd ions in the garnet structure. There are 24 Gd^{3+} ions per unit cell. The projection along a $[111]$ direction is shown in (b). The Gd ions are divided into two interpenetrating sublattices. The figures adapted from Ref. [40, 41].

(d site) and octahedron (a site) sites organized by 4 and 8 O^{2-} ions, respectively. The lattice constant of GGG is estimated to be $a = 12.38 \text{ \AA}$. The distance between O^{2-} and Gd^{3+} in the dodecahedral structure (distorted cube) is either 1.89 \AA or 2.45 \AA .

The Gd^{3+} ions are anomalously formed on the magnetic sublattices of a 2-D Kagome lattice [40, 41, 42, 43, 44] incorporating triangles within the garnet structure. The 2-D Kagome lattice is distinguished from a typical triangular lattice by having two interpenetrating corner-sharing triangles in a cubic lattice as shown in Fig. 2.2. The projection of the magnetic sublattices along a $[111]$ direction is shown in Fig. 2.2(b). This peculiar magnetic sublattice structure in GGG produces unique magnetic properties at low temperatures in conjunction with the fact that the GGG is magnetically isotropic. The details are presented in the next chapter.

2.2.3 Original Estimate of EDM Enhancement Factor in GGG

According to the Schiff theorem [32], field shielding inside a crystal makes it impossible to observe EDM interactions. It should be noted that since the Schiff theorem assumes non-relativistic motions, it is not valid for a crystal containing heavy atoms for which relativistic effects must be considered [33]. The theoretical approach has proved that the atomic EDM of heavy atoms is expected to be much larger than that of the bare electron, indicating that the GGG-based EDM experiment has the capacity to improve the EDM sensitivity.

The energy shift ($\Delta\epsilon$) arising from the non-zero atomic EDM d_a of the Gd^{3+} ion in the GGG structure can be expressed in terms of the electron EDM d_e by an EDM enhancement factor α , which quantifies the scale of the local electric field acting on the Gd^{3+} ion

$$\Delta\epsilon = -\alpha d_e E_{ext} . \quad (2.7)$$

In the estimate of α , the energy shift per Gd ion can be written as $\Delta\epsilon = -d_a E_l$ where E_l is the local field that acts on the Gd^{3+} ion. The magnitude of the local field is significantly different from that of the internal field. For a general case, the local field is given by the simple Lorentz relation [45]

$$E_l = \left(\frac{2 + K}{3} \right) E_{int} \quad (2.8)$$

where K is the dielectric constant. The internal field inside the GGG sample, defined by the average electric field over the volume of the crystal cell, is determined by both E_{ext} and the depolarization field within the sample which tends to oppose the applied field. The depolarization field is induced by E_{ext} and is equal to the field in vacuum of a fictitious surface charge density of the sample (see [45]). As a result, E_{int} is reduced

by the dielectric constant K of the GGG material³

$$E_{int} = \frac{1}{K} E_{ext} . \quad (2.9)$$

The magnitude of d_a induced by the electron EDM is calculated in Ref. [46] to be $d_a = -2.2d_e$. According to the theoretical result, the overall energy shift per Gd ion is given by

$$\begin{aligned} \Delta\epsilon &= -d_a E_l = -(-2.2d_e) \left(\frac{2+K}{3} \right) \frac{E_{ext}}{K} \\ &= 0.86d_e E_{ext} \end{aligned} \quad (2.10)$$

with $K \approx 12$ suggested by Ref. [47, 48]. The value of K is also independently confirmed with capacitance measurements (details in the next chapter). Hence, the resulting EDM enhancement factor is estimated to be 0.86. For a more rigorous estimate of α , the displacement of Gd^{3+} with respect to surrounding O^{2-} due to the local field on the {dodecahedral} lattice (GdO_8 cluster) needs to be considered because the wave functions of O^{2-} ions would penetrate inside the Gd^{3+} ion. Specific discussion concerning this is given in Chap. 4.

2.3 Choice of the Magnetometer

The most sensitive magnetometer, the Superconducting Quantum Interference Device, SQUID, is employed to measure minute EDM-induced magnetic signals. Modern SQUID sensors can achieve measurement sensitivity close to the quantum limit. Particular properties of the SQUID sensor are described briefly in this section.

³ $E_{int} = E_{ext} - \sigma/\epsilon_0$ where σ is the surface charge which can be written by $\sigma = \hat{\mathbf{n}} \cdot \mathbf{P}$. Here \mathbf{P} is the polarization and $\hat{\mathbf{n}}$ is the normal vector pointing outward from the polarized material. Since the polarization is given by $P = \epsilon_0 \chi_e E_{int}$ where χ_e is the electric susceptibility, $E_{ext} = (1 + \chi_e) E_{int} = K E_{int}$.

2.3.1 Introduction to SQUID

A superconductor is a material which expels magnetic flux below a certain temperature called the critical temperature (T_c). The maximum magnetic field which can be applied to the superconductor while maintaining its superconducting state is called the critical magnetic field (B_c). As an example, the superconductor niobium has T_c of 9.2 K and B_c of 0.2 T. Two effects which are unique to superconductors are known as the Josephson effect and flux quantization.

When two superconductors are separated by a very thin insulating layer, a supercurrent can still flow between them by Cooper pairs tunneling through the insulating barrier. This is known as the Josephson effect and a junction of this type (superconductor-insulator-superconductor) is called a Josephson junction. Furthermore, when a magnetic flux is applied through a closed superconducting loop, only quantized units of the flux are allowed inside the loop. This effect is known as flux quantization. One flux quantum is formed to be $\Phi_0 \equiv h/2e \approx 2.07 \times 10^{-15} \text{ T} \cdot \text{m}^2$.

The SQUID converts changes in external magnetic flux (Φ_{sq}) to voltage signals as a flux-to-voltage transducer by combining the two unique properties of the superconductor mentioned above [49]. SQUIDs come in DC and RF types. The DC SQUID is capable of higher sensitivity and is the SQUID of choice for this type of experiment. The DC SQUID sensor is composed of two Josephson junctions in parallel on a superconducting loop as shown in Fig. 2.3(a) and is operated by a DC bias current I_b . The principle of magnetic signal detection using the SQUID is as follows. When a steady bias current I_b flows in the SQUID loop (see Fig. 2.3(a)), Cooper pairs penetrate two Josephson junctions with phase coherence and $0.5I_b$ flows through each half of the loop. However, applying a magnetic flux generates a phase difference (θ) between the two superconductors across the Josephson junction. The phase difference causes a change in the critical current I_c in accordance with the relation of $I_c = I_0 \sin \theta$ where I_0 is the critical current without a magnetic flux, Φ_{sq} . The critical current is the maximum supercurrent able to flow while maintaining the superconducting state,

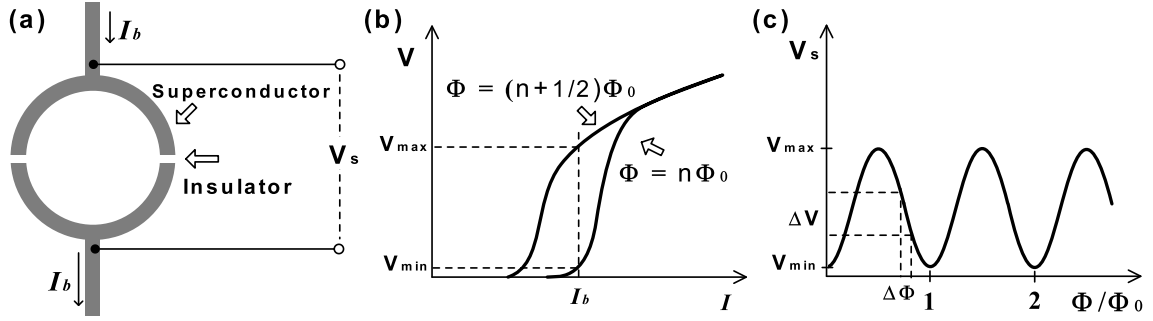


Figure 2.3: (a) DC SQUID with a bias current I_b . (b) V - I characteristic of DC SQUID. (c) V - Φ characteristic of DC SQUID.

that is, a voltage V_s across the SQUID loop appears for $I_b > I_c$ as the material becomes normal with a finite resistance. The voltage-current characteristic is illustrated in Fig. 2.3(b). I_c shows a maximum value when $\Phi_{sq} = n\Phi_0$ and a minimum value when $\Phi_{sq} = (n + 1/2)\Phi_0$. Provided that I_b is fixed at a reasonable value and then Φ_{sq} is steadily increased or decreased, the V_s varies periodically between the maximum value V_{\max} and the minimum value V_{\min} with the period of Φ_0 as shown in Fig. 2.3(c). Thus a change in external magnetic flux $\Delta\Phi_{sq}$ will be converted to a voltage change ΔV .

Since the SQUID sensor outputs a nonlinear voltage signal, similar to the sine wave, it must be linearized for precise measurements. To that end, a feedback circuitry using a flux-locked loop is employed for the DC SQUID sensor.

2.3.2 SQUID Readout Electronics

A typical circuit diagram of a flux-locked loop (FLL) for the DC SQUID is displayed in Fig. 2.4. The FLL circuit, operated at room temperature, converts $\Delta\Phi_{sq}$ into a linearized voltage signal. A FLL is composed of amplification components, a lock-in detector, an integrator, and a feedback circuit including a feedback coil with an inductance of L_f . The SQUID voltage output at the point with a maximum slope

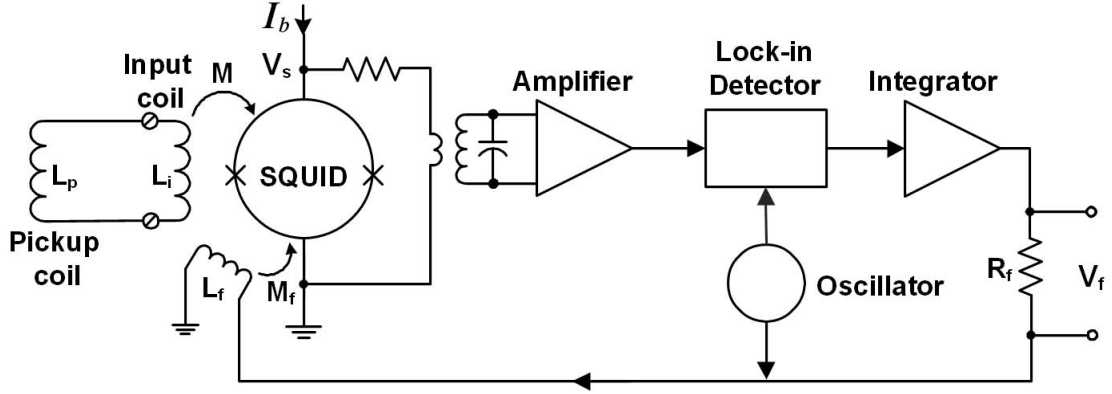


Figure 2.4: FLL circuit for the DC SQUID.

on the nonlinear curve in Fig. 2.3(c) is fixed at zero. Once Φ_{sq} is detected and voltage across the SQUID is changed, the voltage change ΔV is amplified via both the cooled transformer and the amplifier, and then it is measured by the lock-in detector at the flux modulation frequency of a few hundred kHz. The voltage output, which is still nonlinear, from the lock-in detector is followed by the integrator circuit. When the voltage change is integrated, a current I_f flows back into the feedback coil, magnetically coupled to the SQUID with a mutual inductance M_f , to counterbalance the $\Delta\Phi_{sq}$ and retain the fixed point. The ΔV is finally linearized as V_f through the feedback resistance R_f , typically in $k\Omega$ range, with the relation of $\Delta V = I_f R_f$.

The pickup coil with L_p integrates magnetic flux Φ_e , such as EDM-induced magnetic flux in the GGG sample, and the built-in input coil of the SQUID sensor with L_i , inductively coupled to the SQUID with M , generates Φ_{sq} proportional to Φ_e . In general, Φ_{sq} is smaller than Φ_e due to the mismatch in area between the material generating Φ_e and the SQUID. This poses an unavoidable loss in sensitivity to the EDM. The pickup coil can be manually made in the form of magnetometer or n^{th} -order gradiometer, depending on the type of experiment.

The DC SQUID sensor would fail to operate in the flux-lock loop when the flux changes too rapidly. The maximum rate of change of Φ_{sq} is represented as the slew

rate, expressed in Φ_0/s . The intrinsic flux noise for the DC SQUID sensor originates from thermal fluctuations, flux trapping, or critical current change in the SQUID readout electronics and is usually measured to be a few $\mu\Phi_0/\sqrt{\text{Hz}}$.

2.3.3 Operation of the SQUID

Operation of the DC SQUID sensor used in this experiment is done by Star Cryoelectronics' PC-based electronics: PCI-1000 and PFL-100 [50]. The former functions as a computer interface via a standard serial or parallel port, while the latter contains a programmable feedback loop (PFL) and performs the FLL function. The PCI-1000 generates all digital control signals to the PFL as directed by a computer. The linearized voltage output from PFL-100 is transferred to PCI-1000 using a serial port. The overall flow of the electronics is: computer - serial (or parallel) port - PCI-1000 - serial port - PFL-100 - connection wires - DC SQUID - pickup coil.

In order to operate the SQUID sensor in the experiment, first the sensor has to be tuned by a sawtooth-shaped test signal, which provides the SQUID with a flux sweep without the flux-lock loop operating until it reaches the highest sensitivity. The test signal is applied to the feedback coil shown in Fig. 2.4 and then the corresponding magnetic flux is created in the SQUID loop. With the test signal applied, the nonlinear SQUID voltage output will be measured as Fig. 2.3(c). The DC bias current (a few tens of μA) needs to be selected at the point which provides the maximum peak-to-peak amplitude of the output signal to obtain high sensitivity. The blue curve (ch2) in Fig. 2.5(a) is an example where the voltage output signal shows the maximum amplitude of 7.10 V. Furthermore, other tuning parameters such as modulation phase and current must be also optimized to obtain high sensitivity. The output waveform can be varied using another tuning parameter of DC offset which adds a DC voltage to the test signal.

Next, the voltage-to-flux transfer function in units of V/Φ_0 of the SQUID readout system has to be determined so as to estimate the measured magnetic flux of interest

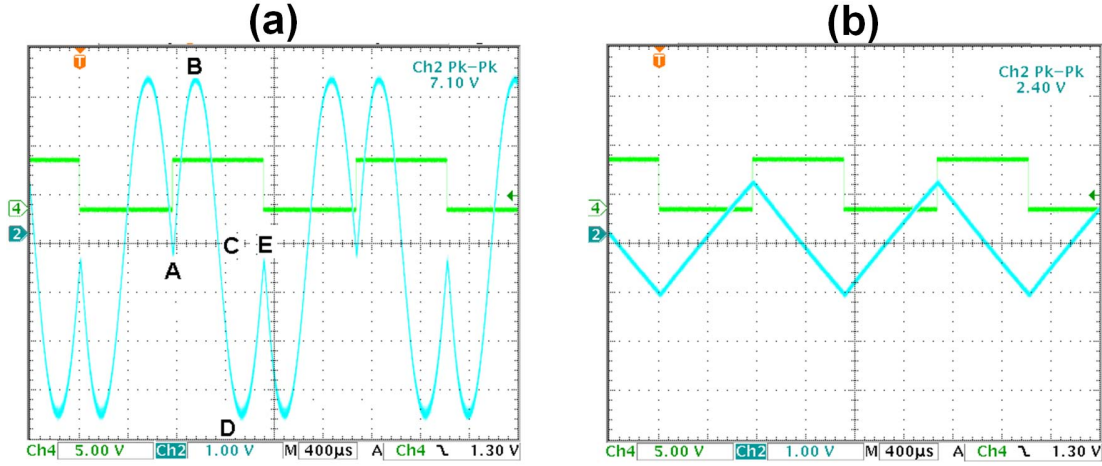


Figure 2.5: One example of a SQUID $V-\Phi$ output signal: (a) without the flux-lock loop operated and (b) with the flux-lock loop operated. The green square wave signal (ch4) with the same frequency as the test signal is a typical triggering source.

from the SQUID readout. To do this, the amplitude of the test signal should be adjusted to correspond to exactly $1 \Phi_0$ by examination of the $V-\Phi$ output. The blue curve in Fig. 2.5(a) shows a SQUID voltage output which satisfies this requirement. In the figure, point B denotes the maximum voltage output with the flux of $(n + 1/2) \Phi_0$ and point D denotes the minimum voltage output with the flux of $n \Phi_0$. In addition, points A and E denote the voltage output with flux $(n + 1/4) \Phi_0$ and point C for a flux of $(n + 3/4) \Phi_0$. It can be estimated that the flux generated by the test signal has increased linearly in the region from A to E and has decreased beyond this region, forming the sawtooth wave. As a result, the amplitude of the test signal in this case corresponds to $1 \Phi_0$. Assuming the test signal corresponds to $3/2 \Phi_0$, the output signal would continue increasing after point E. After accomplishing this calibration, the flux-lock loop is ready to be operated. During this operation, the nonlinear voltage output is changed to the linear output as shown in Fig. 2.5(b). Since the test signal amplitude was adjusted to exactly $1 \Phi_0$, the peak-to-peak amplitude of voltage output in the flux-lock loop is now equal to the voltage-to-flux transfer function (feedback

loop calibration). In the case of Fig. 2.5, the transfer function is estimated to be $2.40 \text{ V}/\Phi_0$.

When the prerequisites for SQUID operation are finished, the test signal can be turned off and the SQUID sensor is ready to measure magnetic signals. To estimate the intrinsic flux noise in units of $\Phi_0/\sqrt{\text{Hz}}$, the voltage output is connected to a spectrum analyzer. During this process, more studies of the magnetic shielding or noise pickup can be conducted. The $1/f$ corner is also determined to choose a pertinent operation frequency for the EDM experiment. Assuming the SQUID output noise is measured to be $7.2 \text{ } \mu\text{V}/\sqrt{\text{Hz}}$ at 1 kHz on a spectrum analyzer, the intrinsic flux noise in Fig. 2.5 is estimated to be $(7.2 \text{ } \mu\text{V}/\sqrt{\text{Hz}})/(2.40 \text{ V}/\Phi_0) = 3 \text{ } \mu\Phi_0/\sqrt{\text{Hz}}$ at 1 kHz.

The bandwidth of the SQUID readout system can be adjusted by the feedback resistance, the voltage-to-flux transfer function, and the integrator capacitor [50]. It is necessary that the SQUID be heated above its T_c prior to operation to eliminate any possible trapped flux.

Chapter 3

Sample Characterization

It is essential to characterize the GGG material which will be used in the EDM experiment. In this section, experimental measurements of the magnetic susceptibility of the GGG solid and possible limitations of the GGG solid. In addition, experimental determinations of the GGG dielectric constant which is an important parameter in estimate of the local electric field acting on the Gd ion are also described.

3.1 Sample Preparation

We synthesized a polycrystalline GGG solid [27] using a solid-state reaction method [51, 52] and bought a single crystal GGG solid. Fig. 3.1 displays the main steps to synthesize the polycrystalline GGG solid: Powders of Gd_2O_3 and Ga_2O_3 are prepared, and ground and mixed together using a mortal and pestle. The synthesized GGG pellets are sintered in the high temperature furnace. The final polycrystalline GGG samples are shown in Fig. 3.1(d).

I measured the resistivity of the synthesized polycrystalline GGG sample using an electrometer (Keithley 6517B), and observed a volume resistivity of $(5.32 \pm 0.04) \times 10^{15} \Omega \cdot \text{cm}$ and a surface resistivity of $(2.95 \pm 0.02) \times 10^{15} \Omega / \text{cm}^2$ at a room temperature. At low temperatures, these resistivities are expected to increase drastically following

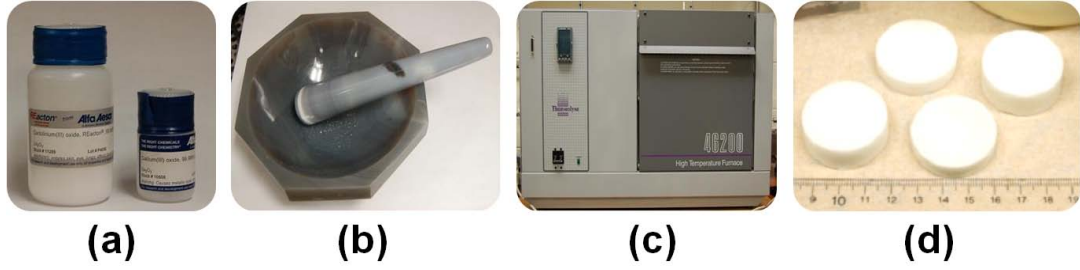


Figure 3.1: Setup for synthesizing the polycrystalline GGG specimens with solid-state reaction methods. (a) Powder of Gd_2O_3 and Ga_2O_3 . (b) Mortar and pestle to grind and mix these powders. (c) High temperature furnace for sintering. (d) Synthesized poly-crystalline GGG samples.

the typical insulator behavior.

3.2 Magnetic Susceptibility

The SQUID-based susceptometer system [54] is used to measure the magnetic susceptibility of both the polycrystalline and single crystal GGG solids. The susceptometer is able to cool the solid to 2 K and has the remarkably high sensitivity provided by the SQUID magnetometer. The DC magnetic susceptibility measurements provide important information about the degree to which the GGG solid is magnetized under an external static magnetic field. Using an external static magnetic field, the solid is magnetized. The resulting induced sample magnetization is measured and provides information about the solid's magnetic response. The DC susceptometer uses a pickup signal derived from the motion of the magnetized GGG sample through the pickup coil in order to detect its induced magnetization. Detailed measurements reveal that the magnetic susceptibility of such a finite-sized sample is slightly reduced due to the demagnetization effect. Therefore careful study of the geometry-dependent demagnetization is necessary to accurately determine the magnetic susceptibility.

3.2.1 Correction for the Demagnetization Effect

In practice, the measured magnetic susceptibility χ_{mea} differs from the intrinsic (true) susceptibility χ due to the geometry-dependent demagnetization effect from demagnetization field \mathbf{H}_d inside the sample. In order to accurately determine the intrinsic magnetic susceptibility of the GGG material, a correction for the demagnetization effect must be applied to the measured susceptibility. The origin of the demagnetization field can be understood intuitively by imaging a fictitious magnetic charge associated with the sample magnetization \mathbf{M} . Maxwell's equation $\nabla \times \mathbf{H} = 0$ when there is no free current inside the sample can be rewritten $\mathbf{H} = -\nabla \Phi_M$, analogous to the electrostatic case $\mathbf{E} = -\nabla \Phi$. Here Φ_M denotes the magnetic scalar potential. The combination of $\nabla \cdot \mathbf{B} = 0$ and $\mathbf{B} = \mu_0(\mathbf{H} + \mathbf{M})$ (in SI units) allows the magnetic scalar potential to satisfy the Poisson equation $\nabla^2 \Phi_M = -\nabla \cdot \mathbf{M}$. The solution for Φ_M taking into account the boundary surface of the sample is written [55]

$$\Phi_M(\mathbf{x}) = -\frac{1}{4\pi} \int_V \frac{\nabla' \cdot \mathbf{M}(\mathbf{x}')}{|\mathbf{x} - \mathbf{x}'|} d^3x' + \frac{1}{4\pi} \oint_S \frac{\hat{\mathbf{n}}' \cdot \mathbf{M}(\mathbf{x}')}{|\mathbf{x} - \mathbf{x}'|} da' \quad (3.1)$$

in conjunction with an outward pointing normal vector $\hat{\mathbf{n}}'$. Here the terms $-\nabla \cdot \mathbf{M}$ and $\mathbf{n} \cdot \mathbf{M}$ can be thought of as a fictitious bound magnetic volume charge density ρ_M distributed throughout the sample volume and the magnetic surface charge density σ_M , respectively. Since the sample is uniformly magnetized only σ_M survives. The resulting magnetic surface charge gives rise to the additional demagnetization field \mathbf{H}_d inside the sample which opposes the applied magnetic field. This leads to a partial cancellation of the applied field inside the sample, analogous to the depolarization electric field associated with the electric surface charge density in electrostatics.

The demagnetization field is given by $\mathbf{H}_d = -N\mathbf{M}$ where N is called the demagnetizing factor which depends on the sample geometry used in the susceptibility measurement. The intrinsic magnetic susceptibility has the form

$$\chi = \frac{M}{H_{\text{int}}} \quad (3.2)$$

where H_{int} is the strength of the internal magnetic field inside the sample. On the other hand, the measured magnetic susceptibility is expressed by

$$\chi_{\text{mea}} = \frac{M}{H_{\text{app}}} \quad (3.3)$$

where H_{app} is the strength of the applied external magnetic field. The relation between \mathbf{H}_{int} and \mathbf{H}_{app} is set by \mathbf{H}_d : $\mathbf{H}_{\text{int}} = \mathbf{H}_{\text{app}} + \mathbf{H}_d$. Therefore the intrinsic magnetic susceptibility can also be expressed as:

$$\chi = \frac{M}{H_{\text{app}} - NM} = \frac{\chi_{\text{mea}}}{1 - N\chi_{\text{mea}}} . \quad (3.4)$$

To accurately determine χ of the GGG material, this equation must be applied to χ_{mea} .

A cube-shaped GGG sample with dimensions $0.30 \text{ cm} \times 0.30 \text{ cm} \times 0.30 \text{ cm}$ was used for this measurement. The demagnetization factor N of the cubic sample was estimated using a three-dimensional finite-element analysis calculation (Field Precision Amaze 3.0 [56]) with the same susceptometer/sample set geometry. The solution volume is the sample chamber of the susceptometer and the boundary is formed by superconducting solenoids generating the static magnetic field. Since the GGG solid becomes spin-polarized under the influence of the static magnetic field, it can be treated as a permanent magnet with an arbitrarily chosen remnant field of 1 Tesla along the z direction. The solution of the magnetostatic field simulation is shown in Fig. 3.2 using a 2-D color-coded filled contour plot of B_z in Tesla along the plane of $y = 0$.

The solution produces a non-uniform magnetic field in such a sample geometry, but the total magnetic flux can be calculated through a square loop with the same area as the sample situated midway around the sample. The algorithm to integrate

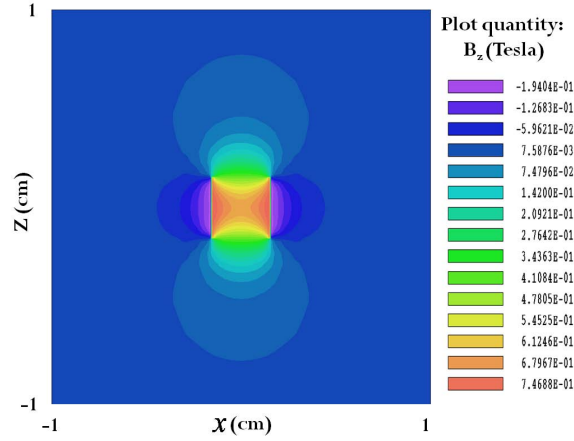


Figure 3.2: Solution of the finite-element analysis calculation investigating the demagnetization factor in 2-D color-coded filled contour plot of B_z in Tesla along the $y = 0$ plane.

the total magnetic flux Φ using the discontinuous field solution is given by:

$$\begin{aligned}
 \Phi &= \iint B_z(x, y) dx dy \\
 &= 4\Delta y \left\{ \sum_{i=1, x_1=0}^{n-1, x_n=0.15} \left[\frac{B_z(x_{i+1}, 0) + B_z(x_i, 0)}{2} \right] (x_{i+1} - x_i) \right. \\
 &\quad + \sum_{i=1, x_1=0}^{n-1, x_n=0.15} \left[\frac{B_z(x_{i+1}, \Delta y) + B_z(x_i, \Delta y)}{2} \right] (x_{i+1} - x_i) \\
 &\quad \left. + \dots + \sum_{i=1, x_1=0}^{n-1, x_n=0.15} \left[\frac{B_z(x_{i+1}, 0.15) + B_z(x_i, 0.15)}{2} \right] (x_{i+1} - x_i) \right\}. \tag{3.5}
 \end{aligned}$$

Δy was set to 0.0015 cm to allow the total flux to be calculated to sufficient accuracy. In such a magnetized sample, the ideal total flux Φ_i is expected to be $\mu_0 MA$. However due to the effect of the demagnetization field, the measured total flux Φ_m is expressed as $\Phi_m = \mu_0(H_d + M)A = \mu_0(1 - N)MA$ and the Φ_m can be rewritten

$$\Phi_m = (1 - N)\Phi_i. \tag{3.6}$$

According to the equation above, comparing the measured total flux to the ideal total flux will provide the value of the demagnetizing factor. Φ_i is expected to be

0.023 T·cm² given the uniform 1 T magnetic flux density inside the sample. On the other hand, the resulting Φ_m is calculated to be 0.017 T·cm² using Eq. 3.5. Thus, using Eq. 3.6, the cubic GGG sample is estimated to have a demagnetization factor $N = 0.26$.¹

3.2.2 Magnetic Susceptibility of a Polycrystalline GGG Solid

Once the demagnetization effect is evaluated, the magnetic susceptibility of the synthesized polycrystalline GGG sample can be measured using the DC susceptometer. As a way of observing the sample magnetization, the susceptometer moves the sample through the superconducting pickup coils which are inductively coupled to a SQUID sensor with superconducting wires. The movement of the magnetized sample induces an electric current in the pickup coil in accordance with Faraday's law. The superconducting solenoid, which generates a homogeneous static magnetic field around the sample, surrounds the pickup coils which are located at the center of the solenoid. Since the pickup coils are in the form of a second-order gradiometer, any common-mode magnetic signals can be eliminated and only the sample magnetization is detected by the SQUID sensor.

The GGG sample was cut using a diamond saw into a cube approximately 0.30 cm × 0.30 cm × 0.30 cm. The total number of moles of Gd³⁺ ions inside the sample was 0.00062 and its total weight and volume were measured to be 0.21 g and 3.2 × 10⁻² cm³. Based on these measurements, the number density of Gd³⁺ ions is estimated to be 1.2 × 10²²/cm³. The cubic sample is mounted on a rod which allows the sample to move inside the system.

The magnetic susceptibility is in general a tensor quantity rather than a scalar.

¹The demagnetization factor of some simple geometries has already been analyzed. For example, the factor N for a spherical geometry is known to be 1/3. As a check of the calculation method described above, the simulation was also performed for a spherical geometry and produced a value for N of 0.33, in agreement with the known value.

However, the polycrystalline sample is composed of many differently oriented grains with different sizes. Even if the GGG solid is an anisotropic material, the measured magnetic susceptibility is already an averaged value over all possible orientations of the grains. In other words, the orientation dependence of the susceptibility is negligible and the susceptibility can be regarded as a scalar quantity. To closely study the change in χ with temperature, the measurement sequence consists of multiple steps. The sample magnetization scan is repeated five times and averaged at each temperature setting, ranging from 300 K to 2 K. The statistical error in the measurement originates from the averaging of the magnetization measurements. A zero field process is performed between each sequence of five measurements to eliminate any remaining flux that can be trapped in the superconducting solenoid. When a sequence is finished, the remnant field in the solenoid is measured which provides external field uncertainties. The total statistical error of the measured magnetic susceptibility is determined with the usual propagation of error

$$\delta\chi_{mea} = \chi_{mea} \sqrt{\left(\frac{\delta M}{M}\right)^2 + \left(\frac{\delta H}{H}\right)^2}. \quad (3.7)$$

The volume magnetic susceptibility is determined from several values of the external magnetic field (400 Oe, 100 Oe, and 10 Oe) since the volume susceptibility is used in the extraction of the electron EDM value (see Eq. 4.15). As an example, the result in CGS units with the maximum applied field of 400 Oe is displayed in Fig. 3.3 from 300 K to 2 K. Recall that the demagnetization effect correction to the χ_{mea} is already applied using Eq. 3.4. The data confirm the typical paramagnetic $1/T$ behavior of the GGG sample in which χ increases as temperatures decrease. The fit to the Curie-Weiss relation, $\chi = C/(T - \theta_{CW})$, determines the Curie-Weiss temperature of (-2.09 ± 0.01) K, nearly comparable (8 % discrepancy) to the one determined earlier in Ref. [57], and the Curie constant of (0.160 ± 0.001) . The negative sign of the Curie-Weiss temperature implies that the couplings between adjacent Gd^{3+} ions are indeed antiferromagnetic (AFM), causing the magnetic moment of one

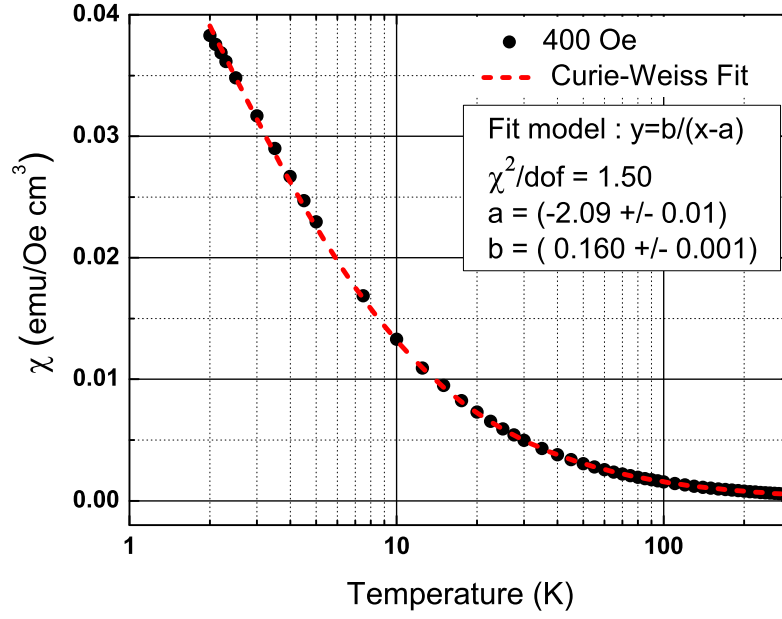


Figure 3.3: Volume magnetic susceptibility (in CGS unit) of the polycrystalline GGG solid as a function of temperature, measured at a maximum applied magnetic field of 400 Oe. The dashed red curve shows the Curie-Weiss fit. The temperature-axis is in log scale.

Gd^{3+} ion to be strongly ordered opposite to that of the nearest Gd^{3+} ions below the Néel temperature (ordering temperature) T_N [45]. The magnetic properties of the GGG solid will change drastically at T_N , in general $T_N \leq |\theta_{CW}|$. These features of the GGG solid suggest that the electron EDM sensitivity presented in Lamoreaux's proposal [26] is overestimated by a few orders of magnitude because the proposal did not take into account the features.

Since the electron EDM experiment is operated at liquid helium temperature, the value of χ at this temperature is required when determining the electron EDM using Eq. 4.14. Each value of χ measured at 4.2 K under the applied fields of 400 Oe, 100 Oe, and 10 Oe is extracted and averaged to obtain the final value of $(330 \pm 2) \times 10^{-3}$ in SI unit (remember that the conversion factor for the χ from CGS unit to SI unit is

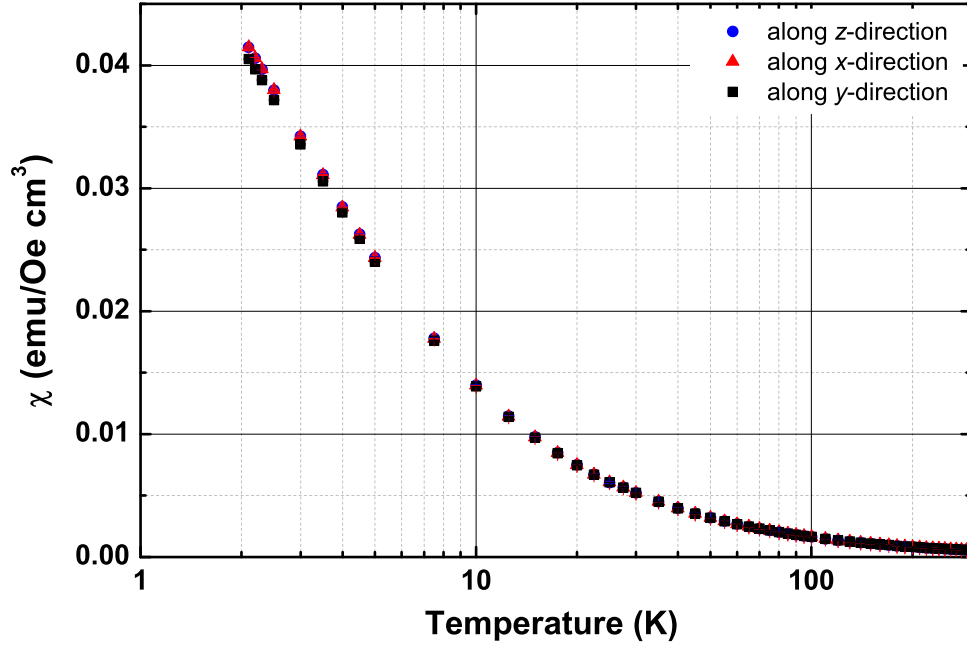


Figure 3.4: Volume magnetic susceptibility of the single crystal GGG sample as a function of temperature, measured at the external field of 400 Oe. The direction of external fields are applied along z (blue circle), x (red triangle), and y (black square).

4π). This is the value of χ that is used in the electron EDM calculation from the magnetic flux measurements.

3.2.3 Magnetic Susceptibility of a Single Crystal GGG Solid

The volume magnetic susceptibility of single crystal GGG solid was also measured. The sample was cut using a diamond saw as described above to make the desired cube. The number of moles of Gd^{3+} ions was estimated to be 0.00053 mole. The sample was measured to have total weight of 0.18 g and volume of $2.6 \times 10^{-2} \text{ cm}^3$. Magnetic anisotropy can be investigated using the signal crystal [58].

In order to understand the orientation dependence of the GGG solid, it is necessary to measure χ in three orthogonal directions: $M_{x,y,z} = \chi_{x,y,z} H_{x,y,z}$. Since the external field direction is fixed along the z -axis in the susceptometer, the sample must be rotated manually around the axes x and y by 90° to determine χ_y and χ_x .

Each χ component (including the demagnetization effect correction) measured at the maximum applied field of 400 Oe is plotted in Fig. 3.4. No strong anisotropic behavior is observable implying no preferred direction for the spin alignments. The result of fully isotropic spins of Gd^{3+} ions is in agreement with what was already described in Ref. [43]. The exchange energy between nearest-neighbor spins can be explained by the Heisenberg model and the second-order dipolar interaction which has an angular dependence (anisotropy) would have negligible influence in the magnetic system.

In comparison with the polycrystalline GGG solid, the single crystal shows a few percent higher magnetic susceptibility. The discrepancy could result from the fact that single crystal GGG has a slightly higher density than the polycrystalline GGG used in the measurement, and thus slightly more Gd^{3+} ions (more unpaired spins) exist in the single crystal which can contribute to the susceptibility. Accordingly, the synthesized polycrystalline GGG sample would contain some impurities such as Gd_2O_3 or Ga_2O_3 . For future electron EDM measurements, it is necessary to prepare more dense polycrystalline GGG samples for further enhancement in the magnetic response. Alternatively, the single crystal GGG can be employed rather than the polycrystal in conjunction with some necessary investigations, for example leakage current effects or SQUID stability studies.

3.2.4 Discussion

It is known that paramagnetic susceptibility with Curie-Weiss behavior is given by

$$\chi = \frac{N\mu_a^2}{3k_B(T - \theta_{CW})} \quad (3.8)$$

where N and μ_a are the number density and the magnetic moment of the paramagnetic Gd^{3+} ion, and k_B is the Boltzmann constant. The magnetic moment is expressed by $\mu_a = g\sqrt{J(J+1)}\mu_B = 7.94\mu_B$ where μ_B is the Bohr magneton with the spectroscopic splitting factor $g = 2$ and $J = 7/2$, assuming that all of the magnetization is coming from the magnetic moments of Gd^{3+} ions. According to this relation, the Curie constant can be defined as $C = N\mu_a^2/3k_B$. Thus the expected value of the Curie constant for the GGG solid is estimated to be 0.16 with $N = 1.2 \times 10^{22}/\text{cm}^3$ of the polycrystal. This expected value is in very good agreement with the value obtained from the Curie-Weiss fit performed on the susceptibility measurement of Fig. 3.3. Thus the reliability of the magnetic susceptibility measurements is confirmed.

3.3 Particular Magnetic Property of the GGG Solid

As described in the preceding section, despite the intrinsic AFM coupling, the spins of the Gd^{3+} ions remain disordered and follow the typical paramagnetic behavior. However, at temperatures lower than the ordering temperature T_N AFM ordering prevails, and the χ value of GGG would significantly deviate from the $1/T$ relation. Usually the χ value of such an antiferromagnetic material exhibits a maximum at T_N [45]. As a result, the distinguishing magnetic property could limit the size of χ and thus hamper the electron EDM sensitivity.

3.3.1 Geometric Frustration

Although the strong AFM coupling could lead to an order-disorder phase transition at T_N , fortunately, this phase transition is highly suppressed and has not been observed in GGG. This is the case because the AFM-coupled Gd^{3+} systems are on magnetic sublattices of a triangle-based Kagome lattice within the garnet structure, as presented in the preceding chapter, and the strong AFM ordering in the sublattice gives rise to a geometrically frustrated magnetic system [44].

It is common for a frustrated antiferromagnet to exhibit a T_N that is much lower than θ_{CW} which is caused by the suppression of long-range magnetic ordering, while a non-frustrated magnet has a T_N almost equivalent to θ_{CW} . In the strongly frustrated GGG magnetic structure below T_N , there exists no single (unique) ground state², thus the spin degree of freedom remains disordered [59, 60]. This exceptional feature transforms the paramagnetic phase of GGG into the unusual spin glass phase [43].

In its spin glass phase, the GGG magnetic system becomes frozen in one of many metastable ground state configurations at a freezing temperature without any long-range ordering [61]. At temperatures lower than the freezing temperature, the strong magnetic response of GGG to the external field is highly minimized so that the magnetic susceptibility does not increase as with typical paramagnetic behavior. The intrinsic spin freezing phenomena in the spin glass phase could restrict the sensitivity of the electron EDM experiment. No clear theoretical explanation for the nature of the freezing process exists, however one can suppose that an anisotropy, which limits the spin fluctuations, originating from the dipolar interaction between the Gd^{3+} spins, may cause the freezing phenomena [43]. Other relevant features of the spin glass state are the frequency dependence of the AC χ as well as the DC χ showing a temperature dependent discrepancy between field-cooled and zero-field-cooled measurements. Based on magnetic susceptibility measurements reported in Ref. [43], the GGG material has demonstrated these features, thus the spin glass transition indeed occurs in GGG.

According to Ref. [43], long-range magnetic ordering in GGG has not been observed until a temperature of 400 mK with applied fields around 1 Tesla, above which the geometric frustration becomes suppressed by the Zeeman energy. This confirms that the magnetic structure of GGG is in a geometrically frustrated state. The spin

²As an example, consider a triangular sublattice within the Kagome lattice, its ground state is six-fold degenerate. The simple hamiltonian of the antiferromagnet is $H = -\sum_{ij} J_{ij} \mathbf{S}_i \cdot \mathbf{S}_j$, where \mathbf{S}_i is the spin in the i^{th} Gd^{3+} ion and J_{ij} is negative for the AFM ordering as the nearest-neighbor interaction.

glass phase transition is reported to occur below 180 mK with an applied field below 0.1 Tesla [43]. Around this temperature (same as the ordering temperature), the magnetic susceptibility displays a rounded peak. Therefore, the electron EDM experiment loses sensitivity to the EDM signal when GGG material is cooled below this temperature, indicative of one of the limitations when working with GGG. Spin freezing in GGG is also reported to occur around 50 mK. However, these features have only been investigated in single crystal GGG; the underlying magnetic properties of polycrystalline GGG at low temperature remain largely unexplored. Neutron scattering experiments on polycrystalline GGG have shown that the GGG magnetic system is not completely frozen [40] at temperatures which correspond to freezing in single crystal GGG.

3.3.2 Possible Improvements

To maintain high sensitivity to the electron EDM at low temperatures, the unpaired spins must remain free to be able to respond to external fields. Therefore, it is essential to learn more about the conditions of phase transitions to ensure that the experiment is operated in the paramagnetic phase. To alleviate spontaneous magnetic ordering at low temperatures, the GGG material can be spin diluted by partially substituting the magnetic Gd^{3+} ions with non-magnetic Y^{3+} ions on the same lattice sites ($\text{Gd}_{(3-x)}\text{Y}_x\text{Ga}_5\text{O}_{12}$). The substitution is expected to greatly reduce the strength of AFM interactions in the system, namely the nearest neighbor spins interaction, J . This results in a lower Curie-Weiss temperature according to the relation [44]:

$$T_{CW} = \frac{2}{3}zS(S+1)k_B|J| \quad (3.9)$$

where z is the number of nearest neighbors (for GGG, $z = 4$). The spin-glass phase transition can be potentially pushed to even lower temperatures. Even though the spin dilution reduces the number density of Gd^{3+} ions a few tens of percent, the restored paramagnetic phase leads to a rapid increase in magnetic susceptibility which

compensates sufficiently for the reduced spin density.

Satisfactory experimental studies of the proposed trial in the GGG system have not yet been accomplished. Our preliminary tests have shown that the spin dilution could help to decrease the temperature at which the spin glass phase transition happens.

3.4 Dielectric Constant Measurement

In order to experimentally determine the dielectric constant of the GGG insulator, a capacitance measurement can be implemented. In the present electron EDM experimental setup (see Chap. 4), the sample/electrodes assembly forms a typical capacitor with the dielectric GGG medium. The capacitance of a capacitor with a dielectric medium is given by the relation of $C = KC_0$ where C_0 is its capacitance in vacuum and K is a dielectric constant. The capacitance C_0 is simply calculated by $C_0 = \varepsilon_0 A/d$, a function of geometrical parameters, where A is the cross sectional area, d is the distance between two conductive electrodes, and ε_0 is the permittivity of vacuum ($\varepsilon_0 = 8.85 \times 10^{-12}$ F/m). This relation does not take into account the fringing fields which alter the effective height of the dielectric medium in the capacitor. Accounting for this effect gives the more accurate capacitance relation:

$$C = K\varepsilon_0 \frac{A}{\xi d} \quad (3.10)$$

where ξ is larger than 1 as a geometrical factor related to the fringing effect.

Finite-element analysis calculations can be used to accurately estimate the value of ξ in the GGG sample/electrodes assembly, which will determine the value of the dielectric constant. The employed strategy consists of: (1) several expected values for the GGG dielectric constant ($K=12, 15$, and 17) are set in the field simulations; (2) each corresponding capacitance value is estimated from the simulation solution; (3) a relation between capacitances and dielectric constants is evaluated (ξ can be determined in this step); and (4) the actual K of the GGG material is determined

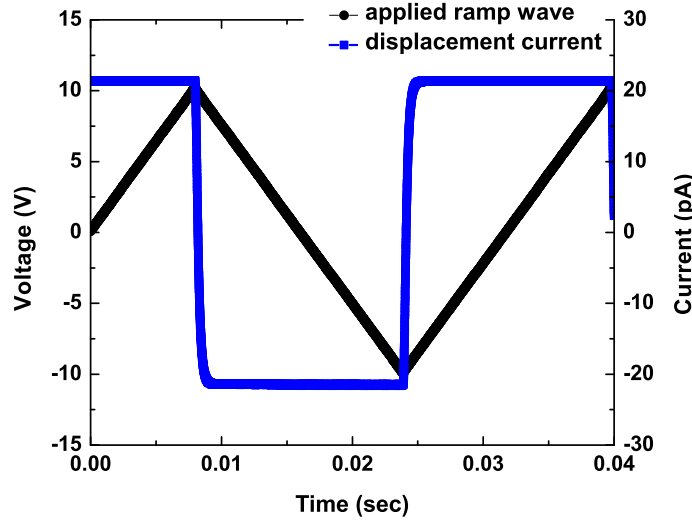


Figure 3.5: Displacement current measurement for the capacitance determination of the GGG/electrodes capacitor. The applied ramp wave is plotted with black circle dots while the measured displacement current is plotted with blue square dots. These time traces have been averaged 512 times.

based on a measured capacitance value. The following sections present both the experimental capacitance measurements using two methods and the field simulation solutions.

3.4.1 Capacitance Determination

Two experimental methods are used for measuring the capacitance of the GGG/electrodes capacitor: one is a direct measurement using a LCR meter (Stanford Research Systems SR720), and the other is a displacement current measurement with a ramp wave applied to the electrodes. In the first method, the capacitance is readily measured to be (19.5 ± 1.6) pF. The uncertainty of this measurement is evaluated using two reference capacitors whose capacitances are already known. In the second method, a ramp wave with a frequency of 31.43 Hz and an amplitude of 20 V_{pp} is applied

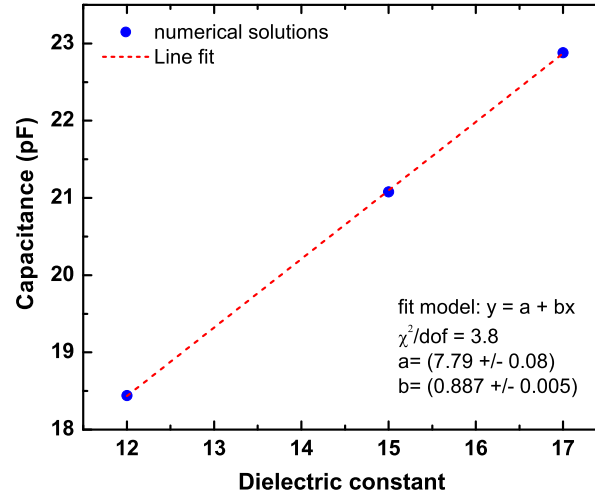


Figure 3.6: Estimated capacitance from the field simulation solutions as a function of the set value of dielectric constant in field simulations. The dashed red line indicates the least-square line fit of the data.

across the GGG medium in series with the electrodes, then the displacement current flowing through the ground electrode is measured by a low-noise current preamplifier. The results are displayed in Fig. 3.5. The lines with black circles and blue squares show the averaged time trace of the applied ramp wave and measured displacement current, respectively. The capacitance is calculated to be (17.1 ± 0.5) pF according to the relation of $I = CdV/dt$ with the applied dV/dt of 1257.2 V/s and the measured current of 21.4 nA. Uncertainty in this measurement is also estimated using two reference capacitors, similar to the first method. As a result, the final experimental capacitance value is measured to be (18.3 ± 1.6) pF by taking an average of the two experimental results above. This experimentally-determined capacitance value will be compared to the value obtained from field simulations.

3.4.2 Numerical Analysis

In the electrostatic field simulations, the top and bottom electrode are set to potentials of 2.5 kV and -2.5 kV while each ground electrode has zero voltage. Note that the lead shields are also at zero voltage, just as in the EDM experiment. The simulation solution in each case (with $K = 12, 15$, and 17) provides a magnitude of total surface charge Q on the top (or bottom) electrode by integrating the normal electric field over the surface of the electrode. The relation $C = Q/V$ where $V = 2.5$ kV determines the capacitance value of the assembly. The results are plotted in Fig. 3.6. The numerically-determined capacitance increases linearly for higher set values of the dielectric constant. The line fit (dashed red line) is performed on the plot to understand the relation between them. The fit gives the result of $C = (7.79 \pm 0.08) + (0.887 \pm 0.005)K$. Thus the final value of the GGG dielectric constant is estimated to be $K = (11.9 \pm 1.9)$ taking into account the experimentally-determined capacitance value of (18.3 ± 1.6) pF.

Chapter 4

Experimental Details

With the GGG solid characterized, a prototype electron EDM experimental cell from two disk-shaped GGG samples has been built. In this chapter, the experimental design of the GGG-based measurement and the relation between the measured magnetic flux and the EDM signal will be discussed.

4.1 Experimental Design

4.1.1 Experimental Setup

The electron EDM experiment consists of two disk-shaped polycrystalline GGG samples with a diameter of 3.3 cm, a height of 0.76 cm, and a density of 6.66 g/cm^3 . The GGG samples are sandwiched between two planar high voltage (HV) electrodes and two isolated ground electrodes as shown in Fig. 4.1. The HV electrodes are connected to HV sources of opposite polarities in such a way that the electric fields in both GGG samples are aligned along the same direction. In the presence of a strong electric field, the electron EDMs are aligned by the applied electric field, leading to a net spin polarization in the sample since the EDM vector lies parallel (or antiparallel) to the spin vector as a result of the Wigner-Eckart theorem. This Stark-induced spin ordering generates a bulk magnetization which produces a magnetic field surrounding

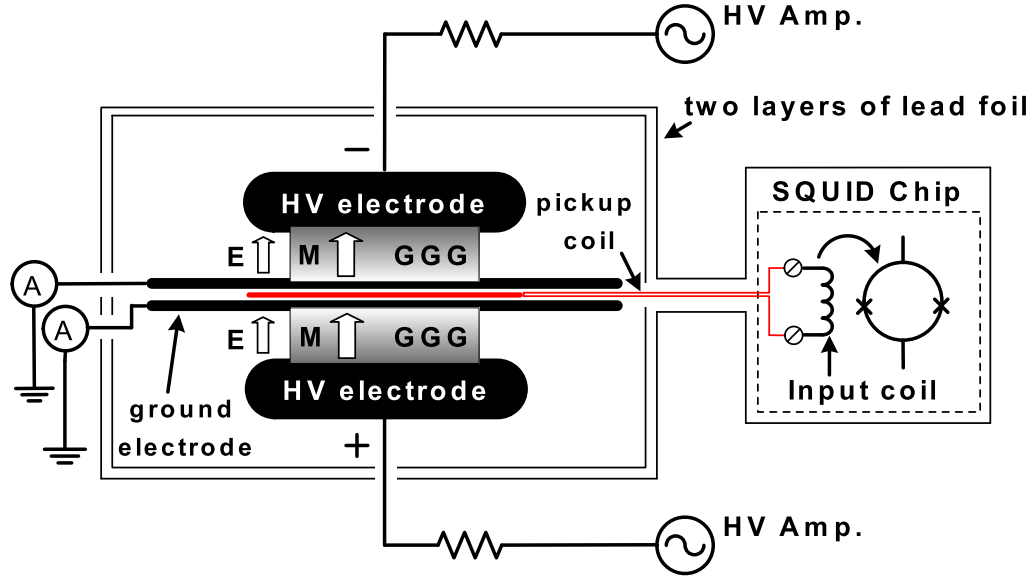


Figure 4.1: Schematic of the experimental setup for the GGG-based solid-state electron EDM experiment.

the paramagnetic GGG sample. The magnetization can be detected using an ultra-sensitive DC superconducting quantum interference device (SQUID) sensor, serving as a flux-to-voltage converter. During the experiment, leakage currents on the ground electrodes are monitored by a dedicated low-noise current preamplifier (Stanford Research Systems SR570). The experimental advantage of using the current preamplifier is that it can be operated by internal batteries to eliminate any noise coming from the AC power lines.

The experimental setup is displayed in Fig. 4.2. Fig. 4.2(a) shows the assembly that houses the GGG samples and the electrodes. The assembly, covered by fiber glass (G10) plates, long nylon screws, and ceramic nuts, is inserted in a G10 cylinder with radius 7.6 cm and height 15 cm. The assembly is shielded from external magnetic fields with two layers of superconducting lead foils shown in Fig. 4.2(b). The SQUID magnetometer and the flux pickup coil are also surrounded by a solder-sealed

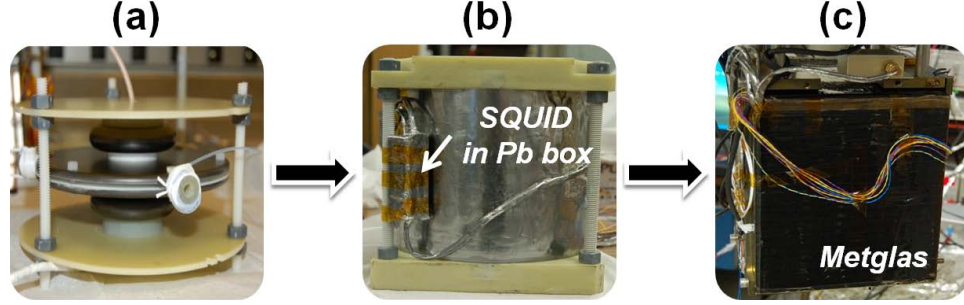


Figure 4.2: Photographs of the experimental setup. (a) The assembly that houses the GGG samples and electrodes. (b) The assembly surrounded by two layers of superconducting lead foils. (c) Additional magnetic shields of three layers of Mu-metal wound on square forms with symmetry axes along the x , y , and z directions.

lead box and lead tubing. The system employs an additional three layers of passive magnetic shielding made of Mu-metal¹ (Metglas alloy ribbon) wound on square forms with symmetry axes along the x , y , and z directions and is shown in Fig. 4.2(c). Fig. 4.3 shows photographs of the cryogenic systems for the experiment. As shown in Fig. 4.3(a), both the HV lines and leakage current monitor wires are surrounded by long lead tubing. Since several holes in the superconducting magnetic shields are inevitable in order to connect the wires to the samples/electrodes assembly, the lead tubes are more than 10 times longer than the diameter of the corresponding holes, which can effectively prevent external magnetic fields from passing through the holes. The magnetically-shielded SQUID control wires (3 pairs of copper wires) are connected to the PFL circuit box outside the cryostat through a RF-shielded connection box. The experiment is mounted inside a stainless steel cryostat to allow full immersion in a bath of liquid helium at 4.2 K and atmospheric pressures as shown in Fig. 4.3(b). Finally, a cylinder of Co-Netic ferromagnetic shielding (with a maximum

¹Mu-metal is an alloy of approximately 75 % nickel, 15 % iron and copper and molybdenum. Since it has very high magnetic permeability ($\mu_r \approx 90,000$), it effectively screens static or low-frequency magnetic fields.

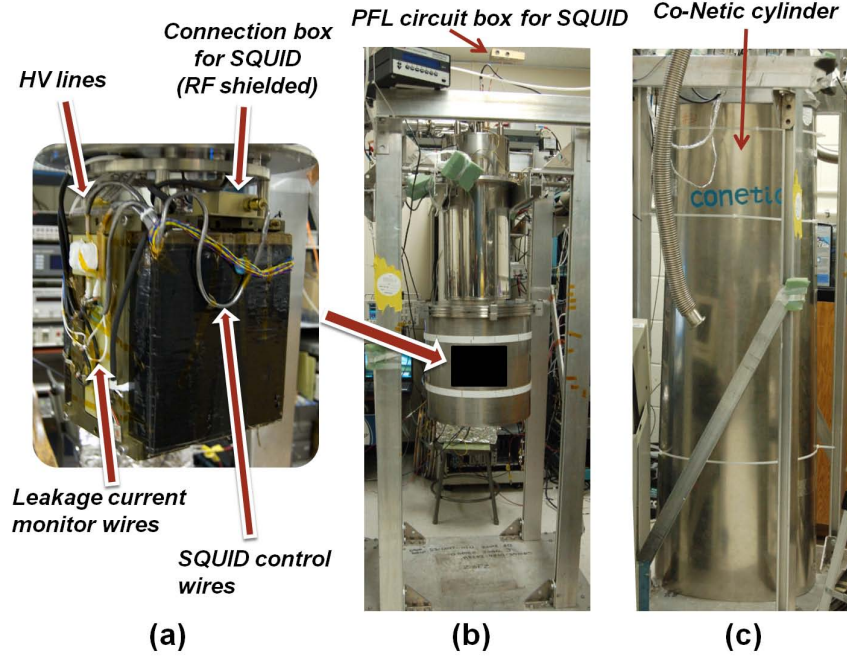


Figure 4.3: Photographs of the instrumentations. (a) The samples/electrodes assembly is encased by several magnetic shields. The HV lines and leakage current monitor wires are surrounded by lead tubing. The magnetic-shielded SQUID control wires (3 pairs) are connected to a RF-shielded connection box. (b) The continuous-flow helium cryostat. The system is fully immersed in a liquid helium bath. (c) A cylinder of Co-netic ferromagnetic shielding encompasses the whole cryostat for further improvement of magnetic shielding.

$\mu_r \approx 450,000$) at room temperature encompasses the whole cryostat to provide the initial reduction of the ambient fields as shown in Fig. 4.3(c).

The electrodes, both HV and ground, are made of machinable ceramic (MACOR) coated with graphite, a non-metallic material, to provide a large but finite resistivity. Electric conductors generally give rise to magnetic field fluctuations (magnetic Johnson noise) produced by thermal fluctuations of current densities which vary with electrical resistivity and thickness. Hence, magnetic Johnson noise could limit the experimental sensitivity in this EDM experiment which strives to detect very weak

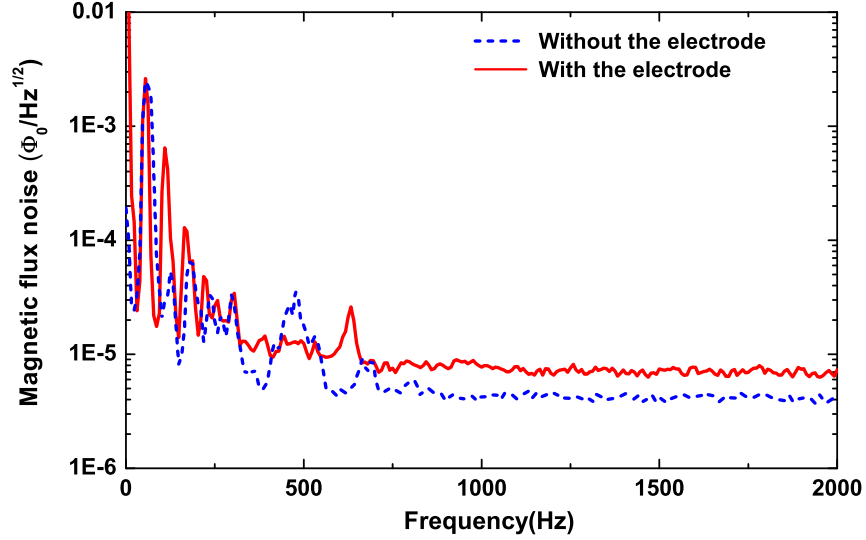


Figure 4.4: Magnetic flux noise spectra of the SQUID magnetometer. The solid (red) and dashed (blue) spectra are with and without a semitron electrode, respectively. The magnetic noise at 1 kHz with the electrode installed is a factor of 1.8 larger than without the electrode installed.

magnetic signals. To experimentally verify that the presence of the electrical conductor increases the magnetic noise, a small cryostat was used in which a SQUID sensor and various electrodes can be tested easily at 4.2 K. A DC SQUID sensor was mounted in the cryostat and immersed in liquid helium. Then the magnetic flux noise of the SQUID sensor was measured using a spectrum analyzer (Stanford Research Systems SR780) with and without the semitron electrode. The semitron electrode was positioned about 1.0 cm away from the pickup coil inductively coupled to the SQUID sensor. Fig. 4.4 shows the measured magnetic flux noise spectra. The baseline noise at 1 kHz with the electrode installed is measured to be $6.92 \mu\Phi_0/\sqrt{\text{Hz}}$, while without the electrode the noise is measured to be $3.85 \mu\Phi_0/\sqrt{\text{Hz}}$. This confirms that electrical conducting materials generate some degree of magnetic Johnson noise, thereby reducing the sensitivity of the SQUID sensor. Many vibrational peaks at

low frequencies in the spectra are also observed due to insufficient superconducting magnetic shields.

The results from Ref. [62, 63] show that the simplified magnetic Johnson noise $B_J(z)$ at a distance z from the surface of an infinite conducting material with a thickness of t and an electrical resistivity of ρ is

$$B_J(z) \propto \sqrt{\frac{k_B T t}{8\pi \rho z(z+t)}} \quad (4.1)$$

where k_B is the Boltzmann's constant and T is the absolute temperature. This relation shows that the larger resistivity ρ_g of graphite as compared to common conducting materials such as copper ρ_c or aluminum ρ_a helps to reduce the magnetic noise (note that $\rho_g = 1.4 \times 10^{-5} \Omega\cdot\text{m}$, and $\rho_c = 1.7 \times 10^{-8} \Omega\cdot\text{m}$, $\rho_a = 2.7 \times 10^{-8} \Omega\cdot\text{m}$ at room temperature). Using a graphite coating rather than a bulk piece of graphite for the electrode reduces the thickness considerably and suppresses the magnetic noise (in practice it is difficult to use a pure graphite electrode due to its weak strength).

An additional challenge in the EDM experiment is the presence of eddy currents, one of the systematic effects of the experiment, which contribute to magnetic flux noise. The well-known eddy current proportionality $1/\sqrt{\rho}$ implies that the eddy current effect can be reduced when the electrode is painted with graphite. The top and bottom surfaces of the GGG samples are also thinly painted with graphite to make better contact between the electrodes and the samples. This helps to reduce possible electrical breakdowns.

4.1.2 Optimized Pickup Coil Design

The magnetic flux pickup coil is situated between the two ground electrodes. The coil is made from an insulated superconducting niobium wire with a diameter of 0.013 cm (36 AWG) (see fig 4.1). The pickup coil is in the form of a planar first-order gradiometer with a two-turn inner coil wound clockwise with a radius of 1.8 cm and a single-turn outer coil wound counter-clockwise with a radius of 2.5 cm on a MACOR

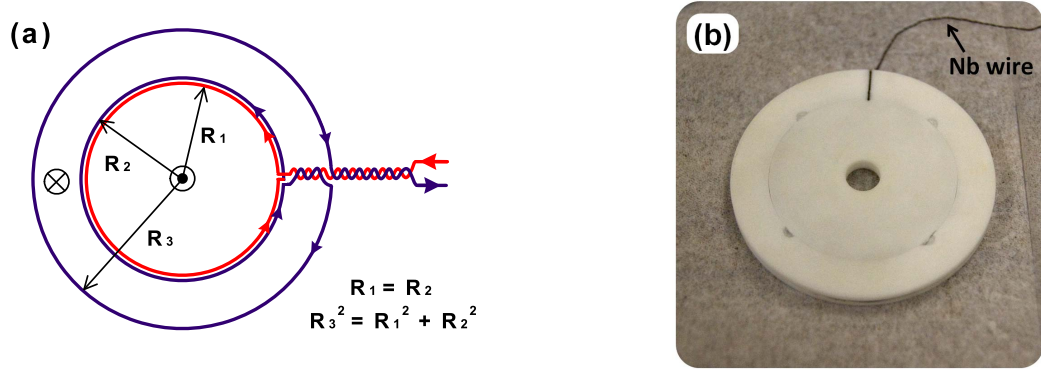


Figure 4.5: The magnetic flux pickup coil. The inner diameter matches the diameter of the GGG sample. For best CMRR, the inner area πR_1^2 is matched to the outer area $\pi R_3^2 - \pi R_2^2$ where $R_1 = R_2$. (a) Schematic representation of the pickup coil geometry. (b) Photograph of the actual assembled home-made pickup coil. The white material used to hold the niobium wires is machinable MACOR ceramic.

support as shown in Fig. 4.5. Note that the radius of the outer coil is a factor of $\sqrt{2}$ larger than the radius of the inner coil. The diameter of the inner coil matches the diameter of the sample. In such a configuration, the pickup coil integrates the EDM-induced magnetic flux produced by the GGG sample over the area of the coil. More importantly, the use of a gradiometer eliminates the common-mode magnetic signal from the residual magnetic field remaining inside the magnetic shield. It can significantly reduce the magnetic pickup resulting from vibrational motion of the coil under a residual field as shown in Fig. 4.4. The common-mode rejection ratio (CMRR) of a typical hand-wound coil was measured to be ~ 200 , corresponding to a 0.5 % area mismatch.

The pickup of the coil is slightly enhanced by partially enclosing the returning flux, leading to an enhancement factor when compared with a simple one-turn coil in the following way: The total magnetic flux Φ_{total} picked up through by the coil is given by

$$\Phi_{\text{total}} = \Phi_{\text{in}} - \Phi_{\text{out}} \quad (4.2)$$

where Φ_{in} and Φ_{out} are the magnetic flux measured by the inner two turns coil and the outer single turn coil. The negative sign comes from the fact that the inner and outer coils are wound in the opposite directions. Φ_{in} and Φ_{out} are given by

$$\begin{aligned}\Phi_{\text{in}} &= 2(B_{\text{EDM}} + B_{\text{R}})A_{\text{in}} \\ &= 2\pi R_{\text{in}}^2(B_{\text{EDM}} + B_{\text{R}}),\end{aligned}\tag{4.3}$$

$$\begin{aligned}\Phi_{\text{out}} &= B_{\text{EDM}}A_{\text{in}} - \eta B_{\text{EDM}}(A_{\text{out}} - A_{\text{in}}) + B_{\text{R}}A_{\text{out}} \\ &= \pi[B_{\text{EDM}}R_{\text{in}}^2 - \eta B_{\text{EDM}}(R_{\text{out}}^2 - R_{\text{in}}^2) + B_{\text{R}}R_{\text{out}}^2]\end{aligned}\tag{4.4}$$

where B_{EDM} denotes the EDM-induced magnetic field and B_{R} denotes the common mode residual field. A_{in} and A_{out} are the cross-sectional area of the inner coil and outer coil, respectively. R_{in} is the radius of inner coil and R_{out} is that of outer coil. The second term in Eq. 4.4 represents the returning EDM-induced magnetic field enclosed through the outer area ($A_{\text{out}} - A_{\text{in}}$) which is expected to be some fraction of B_{EDM} as a factor of η ranging from 0 to 1. Therefore, the relation $R_{\text{out}} = \sqrt{2}R_{\text{in}}$ means Eq. 4.2 becomes

$$\begin{aligned}\Phi_{\text{total}} &= \pi R_{\text{in}}^2(1 + \eta)B_{\text{EDM}} \\ &= (1 + \eta)\Phi_{\text{EDM}}\end{aligned}\tag{4.5}$$

where Φ_{EDM} is the EDM-induced magnetic flux generated by the GGG sample. As a result, our custom flux pickup coil is optimized to enhance the magnetic flux by a factor of $1 + \eta$, resulting in not only enhancement of the EDM sensitivity but also effective elimination of the common mode residual field. The desired value of η is close to one. The present flux enhancement factor is calculated using three-dimensional finite-element analysis calculations and the results are described in the next section.

4.1.3 Flux Enhancement Factor of the Pickup Coil

In order to estimate the present flux enhancement factor, $1 + \eta$, of the pickup coil, a three-dimensional and conformal hexahedral mesh was used in the field simulation

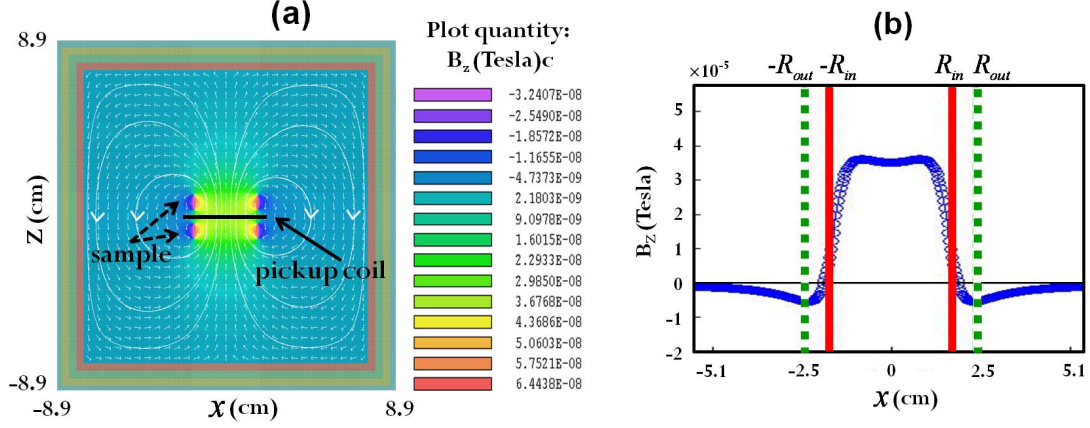


Figure 4.6: Solutions of the finite-element analysis calculations. (a) 2-D color-coded filled contour plot of B_z in Tesla along the plane of $y=0$. The pickup coil is positioned 0.71 cm away from the immediate surface of each sample. (b) Line scans of B_z along $z=0$ where the pickup coil is placed. Solid (Red) and dashed (Green) lines denote the inner and outer coils of the pickup coil.

software [56] with a geometry matching the electron EDM experimental setup shown in Fig. 4.6(a). The pickup coil is located in the center of the solution volume and there are two samples positioned a distance of 0.33 cm above and below the pick up coil. The solution volume is surrounded by two layers of superconducting lead foil for the Dirichlet boundary condition which implies that the magnetic field is constrained to be parallel to any specified boundary². The conformal-mesh size in the sample area is set to ‘fine’ with 0.05 cm size to obtain accurate field solutions. The samples are treated as permanent magnets with a remnant magnetic field of 1 Gauss along

²Let $\hat{\mathbf{n}} = n_x \hat{\mathbf{x}} + n_y \hat{\mathbf{y}}$ be the inwardly directed normal vector to the boundary. Then, the unit vector tangent to the boundary and perpendicular to \mathbf{n} is given by $\hat{\mathbf{t}} = -n_y \hat{\mathbf{x}} + n_x \hat{\mathbf{y}}$. Since the vector potential \mathbf{A} is constant on the Dirichlet boundary condition, $\hat{\mathbf{t}} \cdot \nabla \mathbf{A} = 0$. Supposed that $\mathbf{B} = B_x \hat{\mathbf{x}} + B_y \hat{\mathbf{y}}$, $B_x = \partial A_z / \partial y$ and $B_y = -\partial A_z / \partial x$ with the choice of the *Coulomb gauge* $\nabla \cdot \mathbf{A} = 0$ and $A_x = A_y = 0$. As a result, $\hat{\mathbf{t}} \cdot \nabla \mathbf{A} = -n_y \frac{\partial A_z}{\partial x} + n_x \frac{\partial A_z}{\partial y} = (n_x B_x + n_y B_y) = \hat{\mathbf{n}} \cdot \mathbf{B} = 0$. This final equation implies that the magnetic flux density has to be parallel to the Dirichlet boundary.

the z -axis assuming that the samples produce an EDM-induced magnetization under a strong electric field in the z -direction. A two-dimensional color-coded filled contour plot of the solution B_z along the plane $y = 0$ is shown in Fig. 4.6(a) since the pickup coil is only sensitive to the B_z component of the magnetic field. The returning flux along the outside of the samples is visible in the solution. A line scan of B_z along the line $z = 0$ with a scan width of 0.036 cm is performed to estimate the amount of magnetic flux that is integrated by the pickup coil. Fig. 4.6(b) shows the result of the line scan as a function of x . Solid (red) and dashed (blue) lines correspond to the inner and outer coils of the pickup coil, respectively. It is found that the outer coil partially encloses the returning flux (with a negative magnitude) in the figure.

Since the solution shows a non-uniform magnetic field given a uniform magnetization inside the sample, the algorithm to integrate the solution field B_z through the area of the pickup coil is built as follows:

$$\begin{aligned}\Phi_{\text{in}} &= 2\pi \int_0^{R_{\text{in}}} B_z(x) x \, dx \\ &= \pi \left[\sum_{i=1, x_1=-R_{\text{in}}}^{n-1, x_n=R_{\text{in}}} \left(\frac{B_z(x_{i+1}) + B_z(x_i)}{2} \right) \left| \frac{x_{i+1} + x_i}{2} \right| (x_{i+1} - x_i) \right], \quad (4.6)\end{aligned}$$

$$\begin{aligned}\Phi_{\text{out}} &= 2\pi \int_{R_{\text{in}}}^{R_{\text{out}}} B_z(x) x \, dx \\ &= \pi \left[\sum_{i=1, x_1=-R_{\text{out}}}^{n-1, x_n=-R_{\text{in}}} \left(\frac{B_z(x_{i+1}) + B_z(x_i)}{2} \right) \left| \frac{x_{i+1} + x_i}{2} \right| (x_{i+1} - x_i) \right. \\ &\quad \left. + \sum_{i=1, x_1=R_{\text{in}}}^{n-1, x_n=R_{\text{out}}} \left(\frac{B_z(x_{i+1}) + B_z(x_i)}{2} \right) \left| \frac{x_{i+1} + x_i}{2} \right| (x_{i+1} - x_i) \right]. \quad (4.7)\end{aligned}$$

Since the total magnetic flux pickup is given by $\Phi_{\text{total}} = \Phi_{\text{in}} - \Phi_{\text{out}}$, the flux enhancement factor $1+\eta$ can be estimated by

$$1 + \eta = \frac{\Phi_{\text{total}}}{\Phi_{\text{in}}}. \quad (4.8)$$

The validity of the algorithm used here was evaluated by checking whether the factor $1 + \eta$ estimated using a sum of all of the returning flux as Φ_{out} is equal to 2 because

the magnetic flux lines are closed curves. The resulting Φ_{total} is calculated to be $1.4 \times 10^{-5} \text{ T}\cdot\text{m}^2$, while Φ_{in} is calculated to be $1.3 \times 10^{-5} \text{ T}\cdot\text{m}^2$, leading to the present flux enhancement factor of 1.1. In other words, the effective area A for flux pickup in the gradiometer is a factor of 1.1 higher than the actual cross-sectional area of the GGG sample. It was confirmed that this result does not change with different set values of the remnant field in the field simulation calculation. The flux enhancement factor can be increased up to 1.8 by reducing the radial dimension of the superconducting lead shield, thus compressing the returning flux lines laterally to increase the flux pickup (see Sec. 7.2.2).

4.2 EDM-Induced Magnetic Flux

The EDM-induced magnetic flux in the GGG sample enclosed by the pickup coil, Φ_e , can be estimated using [26]

$$\Phi_e = f \left(\frac{\chi \alpha d_e E_{\text{ext}}}{\mu_a} \right) A . \quad (4.9)$$

Recall that α is the effective paramagnetic EDM enhancement factor for the Gd^{3+} ion in the GGG structure, which includes the effect of the dielectric reduction of the external field. E_{ext} is the strength of the externally applied electric field, A is the effective cross-sectional area of the pickup coil, μ_a is the magnetic moment of the paramagnetic Gd^{3+} ion, with the assumption that all of the magnetization is coming from the magnetic moments of the heavy atoms carrying an EDM, and f is the flux suppression factor due to the demagnetizing effects which depend on the geometry of the GGG sample. One can see immediately that for this magnetization-type EDM search, a desired sample material should have large magnetic susceptibility, hence the choice of GGG was appropriate. This section will discuss in detail several undetermined parameters that appear in Eq. 4.9.

4.2.1 Effective EDM Enhancement Factor

Sushkov's group [64, 65, 46, 66] carried out extensive theoretical calculations on the effective EDM enhancement factor α seen in Eq. 4.9. In the perturbation calculation, the EDM-induced energy shift $\Delta\epsilon$ per Gd^{3+} ion arises from three independent effects: (a) the electron EDM interaction on the Gd^{3+} ion, (b) the electron-electron Coulomb interaction, and (c) the crystal lattice deformation originating from the positional shift of the Gd^{3+} ion with respect to the surrounding O^{-2} ions in the GdO_8 cluster. The relativistic EDM interaction V_d with the electric field \mathbf{E} used in the perturbation calculation is given by $V_d = -d_e\gamma_0\boldsymbol{\Sigma} \cdot \mathbf{E}$ where γ_0 and $\boldsymbol{\Sigma} = \gamma_0\gamma_5\boldsymbol{\gamma}$ are Dirac γ matrices [64], in contrast with the non-relativistic interaction $\mathbf{d} \cdot \mathbf{E}$. In the electron EDM interaction, single-particle perturbation theory contributes to the EDM enhancement factor calculation. Since unpaired electrons in the Gd ion are in the electronic f shell, the leading many-body corrections (residual Coulomb interactions between valence and core electrons) to the calculation need to be taken into account. The resulting EDM enhancement factor from the electron EDM effects (a) and (b) is calculated to be -2.2 ± 0.5 .

The crystal lattice deformation is shown in Fig. 4.7. In the GdO_8 cluster in the form of a distorted cube, the O^{-2} ion has a closed shell with electronic configuration $1s^22s^22p^6$. In three doubly occupied $2p$ orbitals, only $2p_\sigma$ electrons are considered because the $2p_\sigma$ orbitals point toward the Gd^{3+} core so that the orbitals penetrate inside the Gd core. The displacement of the Gd core along the field direction induced by the local electric field along the z -axis causes the deformation of the lattice, resulting in a change of the wave functions inside the Gd core. The lattice deformation effect induces an additional EDM enhancement factor of 16.

Considering the three independent effects, the resulting $\Delta\epsilon$ is calculated to be $36d_eE_{int}$ where E_{int} is the electric field inside the sample. Because of the dielectric reduction of the internal electric field of $E_{int} = E_{ext}/K$ where the dielectric constant $K \simeq 12$ in GGG as mentioned in the preceding chapter, the overall energy shift per

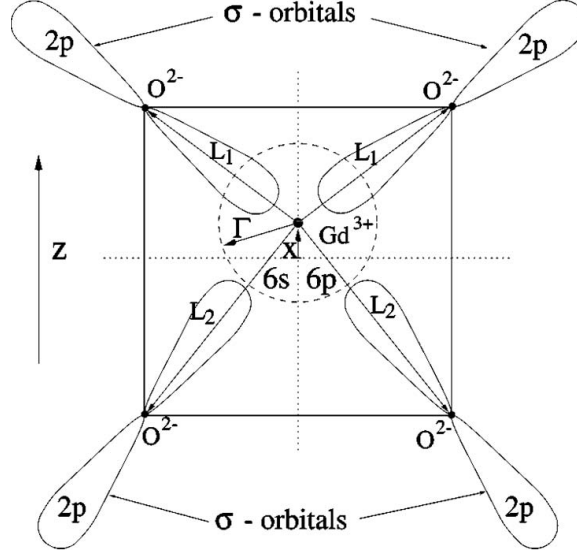


Figure 4.7: 2-D schematic of lattice deformation [66]. $2p_\sigma$ electrons of O^{-2} penetrate inside the shifted Gd core.

Gd³⁺ ion is

$$\Delta\epsilon = 36d_e \left(\frac{E_{ext}}{12} \right) = 3.0d_e E_{ext} . \quad (4.10)$$

Note that the authors used a value of $K = 30$ quoting from an online table [67]. References all suggest a smaller $K \simeq 12$, and we also independently confirmed the smaller dielectric constant of the GGG with capacitance measurements (see Sec. 3.4). Hence, the effective EDM enhancement factor α is 3.0, which is a factor of 3.5 larger than the original estimate in Sec. 2.2.3.

4.2.2 Effect of the Sample Geometry

The flux suppression factor f in Eq. 4.9 describes the degree to which the actual magnetic flux generated by the samples is reduced due to the effect of finite sample geometry. The factor f of the disk-shaped GGG sample with a diameter of 3.3 cm and a height of 0.76 cm used in the experiment has been calculated with finite-element analysis calculation. The samples are treated as a permanent magnet with a remnant

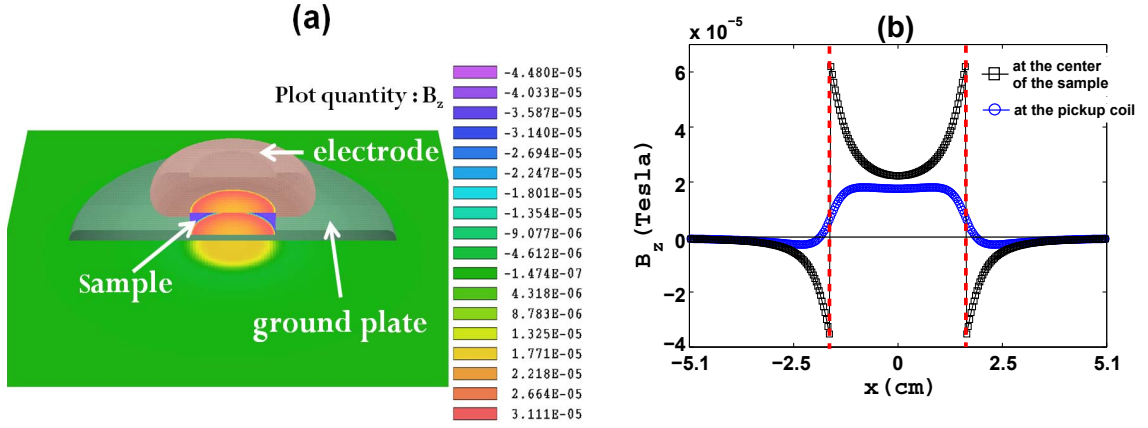


Figure 4.8: Solutions of finite-element analysis calculations for estimating the flux suppression factor f . (a) 3-D color-coded filled contour plot of B_z in Tesla including a slice plane along $z=0$ cm. The sample/electrodes assembly is cut along a plane of $y=0$ for better visualization. (b) Line scans of B_z along the line $z=0$ and through the center of the sample with square black dot and circle blue dot, respectively. The red dashed lines denote the diameter of the GGG sample.

magnetic field of 1 Gauss along the z -axis as the estimate of the flux enhancement factor of the pickup coil. Fig. 4.8(a) shows a color-coded three-dimensional contour plot of B_z in Tesla containing the overall sample/electrodes assembly that is built in the calculation. There are two layers of lead foils exterior to the solution volume not shown in the figure. The pickup coil is located on the green colored slice plane at $z = 0$. Fig. 4.8(b) shows line scans of B_z in Tesla. The square black dots and round blue dots are field solutions along the line $z = 0$ and along the sample center (halfway between sample's top and bottom surfaces) respectively.

The flux Φ_e in Eq. 4.9 is estimated using the algorithm in Eq. 4.6 due to the non-uniform magnetic field solutions. The actual Φ_e is expected to be $4.2 \times 10^{-5} \text{ T} \cdot \text{m}^2$ since the remnant field is uniformly set to be 1 Gauss throughout the sample volume. However, the resulting magnetic flux measured when the pickup coil is positioned at the center of the sample is estimated to be $1.5 \times 10^{-5} \text{ T} \cdot \text{m}^2$. The EDM-induced

magnetic flux is suppressed by a factor of 0.37 which is a result of the finite dimensions of the sample geometry. The resulting magnetic flux measured when the pickup coil is positioned between the ground electrodes (at $z = 0$) is estimated to be $0.65 \times 10^{-5} \text{ T} \cdot \text{m}^2$. As a consequence, the EDM-induced magnetic flux is suppressed by another factor of 0.43 due to the placement of the pickup coil 0.33 cm away from the immediate surface of the sample. The total suppression factor f is estimated to be 0.16, leading to a loss of sensitivity to the electron EDM which was not considered in the original proposal [26].

The flux suppression factor can be reduced by moving the pickup coil nearer to the sample (see Sec. 7.2.2). Note that the origin of this flux suppression is the demagnetization field when the sample has a macroscopic magnetization, as discussed before in the context of the magnetic susceptibility measurement (see Sec. 3.2.1). A simple analytical model for describing the flux suppression can be developed by treating the bulk magnetization of the sample as a current flowing on the sample surface by Stokes' theorem. The details are in Appendix B.

4.2.3 Flux Transfer Efficiency

As shown in Fig. 4.1 and more specifically in Fig. 4.9(a), the flux pickup coil connects to the built-in input coil of the SQUID sensor chip (Superacon CE2 blue). The pickup coil self-inductance L_p has been measured to be 618 nH using the SR720 LCR meter. The model CE2 blue sensor, displayed in Fig. 4.9(b), is a low- T_c DC SQUID magnetometer with low input coil self-inductance L_i of 420 nH and mutual inductance M between input coil and SQUID of 8.1 nH. The SQUID sensor provides low intrinsic flux noise of $\sim 3\mu\Phi_0/\sqrt{\text{Hz}}$, suitable for the EDM experiment. A supplemental low-pass filter is added in parallel at the input coil to greatly reduce high frequency spark signals from leaking into the SQUID loop.

The EDM-induced magnetic flux change Φ_e through the pickup coil induces an electromotive force ε varying as a function of time around the circuit by Faraday's

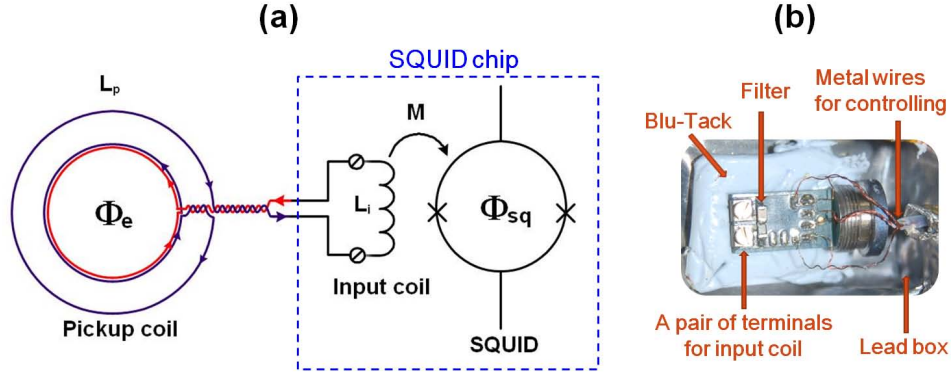


Figure 4.9: (a) Schematic circuit diagram of the SQUID sensor inductively coupled to the flux pickup coil. (b) Photograph of the SQUID sensor used in the EDM experiment. The sensor is shielded by a superconducting lead box from external magnetic fields and mounted with Blu-Tac inside the lead box to reduce its vibration.

law:

$$\begin{aligned}\varepsilon &= -\frac{d\Phi_e}{dt} = -A\frac{dB_e}{dt} \\ &= i\omega\Phi_e\end{aligned}\tag{4.11}$$

where A is the effective cross-sectional area of the pickup coil and ω is the frequency of the flux. Note that the pickup coil used in the experiment is an one-turn gradiometer. A current I_e is induced by the electromotive force, which is given by

$$\begin{aligned}I_e &= \frac{\varepsilon}{(z_i + z_p)} = \frac{i\omega\Phi_e}{i\omega(L_i + L_p)} \\ &= \frac{\Phi_e}{(L_i + L_p)}\end{aligned}\tag{4.12}$$

where z_i and z_p are impedances of the input coil and the pickup coil, respectively. The current flows into the input coil and produces a flux Φ_{sq} that inductively couples to the SQUID loop. The flux through the SQUID loop, Φ_{sq} , is read out as a voltage signal as mentioned in Sec. 2.3. As a result, the relation between Φ_{sq} and Φ_e is given

by

$$\Phi_{sq} = MI_e = \frac{M}{(L_i + L_p)} \Phi_e = \beta \Phi_e . \quad (4.13)$$

Here the factor of β is the flux transfer efficiency which quantifies how much the flux is diminished when Φ_e is delivered to the SQUID sensor. With the values of inductances above, β is calculated to be 0.0078, indicating that the SQUID measures only 0.8 % of the EDM-induced magnetic flux produced in the sample area. Consequently, this flux reduction is another inevitable cause of EDM sensitivity loss because the physical observable is not Φ_e but Φ_{sq} in the experiment. The final relation between Φ_{sq} and d_e is expressed by

$$d_e = \frac{\Phi_{sq} \mu_a}{\beta f \chi \alpha E_{ext} A} , \quad (4.14)$$

and the corresponding statistical sensitivity of d_e is determined by the typical propagation of error:

$$\delta d_e = |d_e| \sqrt{\left(\frac{\delta E_{ext}}{E_{ext}}\right)^2 + \left(\frac{\delta \chi}{\chi}\right)^2 + \left(\frac{\delta \Phi_{sq}}{\Phi_{sq}}\right)^2} . \quad (4.15)$$

These formulas will be used to extract the EDM signal from the magnetic flux measurements.

To enhance the measurable flux, a several-turn pickup loop might be used. Having the N -turn pickup loop leaves Eq. 4.13

$$\Phi_{sq} = \frac{NM}{(L_i + L_p)} \Phi_e .$$

Therefore, the flux transfer efficiency can be improved by a factor of N , resulting in enhancement of the EDM sensitivity. However, increasing continuously the number of turns in the pickup coil causes the EDM sensitivity to deteriorate since the pickup coil inductance is proportional to N^2 . The optimal N is usually determined by maximizing the Φ_{sq} : $\partial \Phi_{sq} / \partial N = 0$. The maximum value of Φ_{sq} happens at $L_p \approx L_i$. As a result, improvement of the flux transfer efficiency is valid only until $L_p \approx L_i$. The reason that the gradiometer used in the experiment has just one turn is to have the self-inductance of the pickup coil match that of the input coil.

4.2.4 Conclusion

The physical observable Φ_{sq} of the EDM experiment was presented as well as the process of conversion of the measured magnetic flux into the electron EDM signal. According to Eq. 4.14, experimental requirements to increase the EDM sensitivity are a strong external electric field, a large sample size and an optimized flux pickup coil. There are two enhancement mechanisms in the GGG material for the EDM sensitivity: the magnetic susceptibility and the EDM enhancement factor. This makes the choice of the GGG material promising for an EDM search. Note that the experimental setup described here is the prototype design for the proof-of-principle measurement. Future work is planned to extend this work to sub-Kelvin temperatures to achieve better sensitivity due to the enhanced magnetic susceptibility (see Chap. 7).

Chapter 5

Essential Improvements

Over the past few years, we have expended significant efforts in studying and mitigating background effects. The efforts include (1) building a 24-bit data acquisition (DAQ) system with ultra-low cross-talk between channels, (2) reducing the voltage drift originating from the HV polarity switch system, and (3) stabilizing operation of the SQUID sensor. In this chapter, I describe these efforts in detail. This chapter also discuss our considerable efforts in enhancing the statistical sensitivity.

5.1 A High Dynamic Range Data Acquisition System

5.1.1 Motivation

The EDM experiment aims to measure the small magnetic signal ($\sim \text{fT}$) generated by the Stark-induced magnetization in the GGG sample as the EDM signal using the SQUID sensor as mentioned in the preceding chapter. According to Lamoreaux's proposal [26], at 10 mK, the spin alignment in the GGG sample is enhanced as the thermal fluctuation is reduced and we would expect an induced magnetic flux of $17 \mu\Phi_0$ with an applied electric field of 10 kV/cm, if the EDM of each unpaired electron in the

solid was as large as 10^{-27} e·cm [26]. Here the flux quanta $\Phi_0 = 2.07 \times 10^{-7}$ G·cm². This EDM-induced magnetic flux is large enough to be measured using a standard DC SQUID magnetometer operated at 4 K. With a typical SQUID transfer function of 2 V/ Φ_0 and a ~ 1 % flux coupling efficiency from the sample to the magnetometer, we expect a voltage signal output from the SQUID electronics to be about 340 nV, without further amplification. A typical data acquisition (DAQ) system with 16-bit resolution (i.e., 0.3 mV resolution in ± 10 V input range) is not sufficient to measure such a small voltage signal. In addition, the experiment requires simultaneous sampling of voltage signals from the magnetometer, high voltage monitors, and leakage current monitors, each with a very different voltage scale. To meet these stringent requirements, we developed an ultra-high precision 24-bit DAQ system with eight input channels for simultaneously sampling the analog voltage signals of interest.

Because the expected EDM-induced magnetic signal to be measured by the SQUID sensor is very small, signal contamination from capacitive coupling of neighboring channels would adversely affect the measurement precision. In particular, the high voltage monitoring channels have a very large voltage that is in phase with the magnetization signal. To address this problem, that has been plaguing the experiment since the very beginning, we take extra efforts to design a custom DAQ system to have each analog input channel individually shielded in its own isolated heavy-duty radio frequency (RF) shielding enclosure with galvanic isolation from the rest of the system. Fiber optic communications to the master board are used for the control of the measurement sequences and the retrieval of the digitized data. With these features, the DAQ system is expected to minimize cross-talk between channels, reduce electromagnetic interference, and reduce the susceptibility to ground loops that could generate noise. Finally, to reduce the random noise and reach the desired EDM sensitivity, we need to repeat the EDM experiment over many polarity modulation cycles and carry out the average of the accumulated data sets. Therefore, ensuring that the DAQ system has no sources of non-Gaussian noise at the level of the required voltage

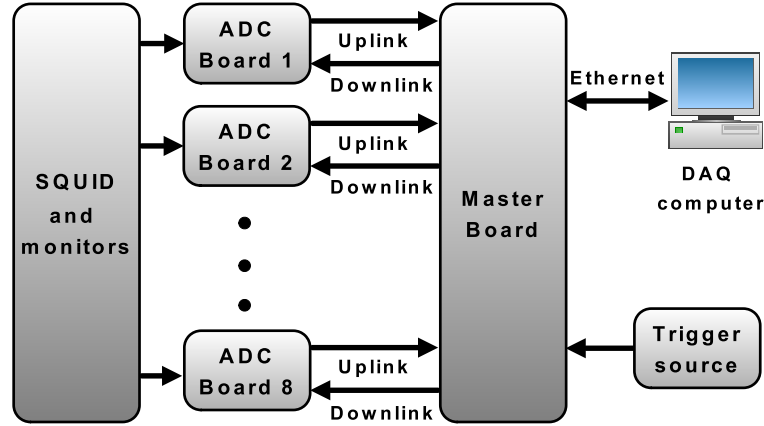


Figure 5.1: Block diagram of the DAQ system.

sensitivity is essential for the success of the EDM experiment. A system capable of such performance requirements is currently not commercially available.

Our custom DAQ system can be used by other experiments that require simultaneous monitoring of several voltage sources. The system can accommodate both very low-level and large-amplitude signals with a large dynamic range that comes with 24-bit resolution. More importantly, the design incorporates good grounding and shielding techniques to reduce noise pickup and channel cross-talk. We explain the hardware and software of the DAQ system in Sec. 5.1.2 and evaluate its overall performance in Sec. 5.1.3.

5.1.2 Description of the hardware

As shown in Fig. 5.1, the DAQ system has a master board to control eight independent modular analog-to-digital converter (ADC) boards. Each ADC board contains a 24-bit ADC chip and supporting electronic components. A front-end of the ADC boards connects to various analog voltage sources in the experiment that need to be measured, digitized, and recorded. The ADC boards can be placed as close as possible to the experiment, with long optical fibers transmitting the digitized signals back to the

master board for temporary data buffering. The master board is equipped with a field programmable gate array (FPGA) chip that can be programmed for specific tasks and DAQ sequences. The communication between the master board and the ADC boards is implemented through serial fiber optic data links in both directions. The data is sent to a DAQ computer at specified intervals. Any personal computer running a MATLAB program can be used as the DAQ computer to interface with the master board through an optically coupled Ethernet port. The device acquires an Internet Protocol (IP) address and thus can be remotely accessed through any computer connected to the Internet. This DAQ computer provides the overall control of data acquisition, data storage and analysis. The DAQ system is triggered through an external trigger source (with a transistor-transistor Logic (TTL) signal) which can be controlled independently by the DAQ computer.

I ADC Board

The ADC board uses a differential-input, 24-bit delta-sigma ADC chip (LTC2440 [68]) made by Linear Technology. Because a high dynamic range with a low noise level is the essential feature for this custom system, we paid extra attention to the noise from different parts of the system. The intrinsic noise of the ADC chip is estimated to be $200 \text{ nV}_{\text{rms}}$ when sampled at 6.9 Hz (with lots of internal oversampling). The sampling rate can be increased up to 3.5 kHz at the cost of larger noise. To preserve this noise figure, we implement the analog front-end with low noise, precision operational amplifiers (LT1007 [69]) that have a high common-mode rejection. The voltage input can be connected single-endedly or differentially. The low degree of voltage noise and fluctuation is further ensured by the use of a very low noise voltage reference (ADR445 [70]) with an adjustment to optimize the common-mode rejection ratio (CMRR).

The schematic diagram of the analog front-end is shown in Fig. 5.2. The input stage comprises a low pass filter (R_1 , C_1 , and R_2 , C_2 for each differential input) to

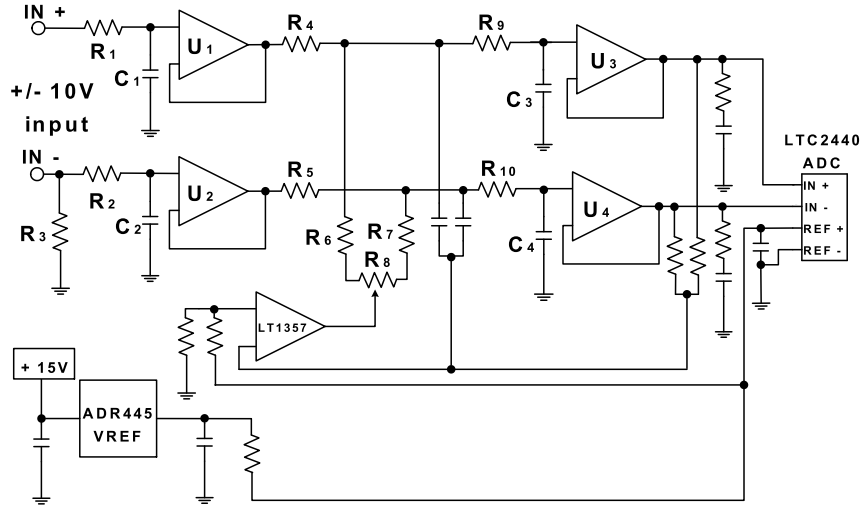


Figure 5.2: Simplified schematic diagram of the low noise front-end of the ADC board.

remove high frequency noise, and a unity gain buffer (U_1 and U_2) to provide a high input impedance of $7\text{ G}\Omega$ to prevent any significant loading and perturbation of the voltage source. The value of R_1 and R_2 is $604\ \Omega$ with a tolerance of 1 % and the value of C_1 and C_2 is 1 nF with a tolerance of 5 %. The cutoff frequency of the low pass filters is calculated to be 264 kHz . The buffers U_1 and U_2 are a bipolar junction transistor (LT1007) with the bias current as low as 10 nA [69]. The resistor R_3 provides a bypass ground path for the operational amplifier (op-amp) bias current when the source ground is not common to the ADC box. The attenuation stage (R_4 - R_7) linearly attenuates the $\pm 10\text{ V}$ input signal, the voltage swing from a typical physics experiment, to a $\pm 2.5\text{ V}$ signal that is compatible with the input voltage range of the ADC chip (LTC2440). The input stage is followed by the buffer stage that comprises an anti-aliasing filter (R_9 , C_3 , and R_{10} , C_4 for each differential input) and a unity gain buffer (U_3 and U_4). The value of R_9 and R_{10} is $150\ \Omega$ and the value of C_3 and C_4 is 82 nF , giving the cutoff frequency of 13 kHz . The anti-aliasing filter attenuates any signal with frequencies above the cutoff frequency to prevent high

frequency interferences from being shifted into the frequency band of interest during sampling. The cutoff frequency of the anti-aliasing filter does not need to change according to the sampling rate because internal filtering of the ADC chip would be suffice. The high impedance of the buffer prevents over-loading of the attenuation stage. Finally, the feedback stage ensures the differential voltage to be centered in the ADC input range around 0 V. The CMRR adjustment is made with potentiometer R_8 . The overall gain accuracy is approximately 0.3 %.

The ADCs are controlled from a complex programmable logic device (CPLD) on the same ADC board using optical communication. The ADC sample clock signal is recovered from the encoded data received over the serial optical interface (see Sec. II) with a phased-locked loop (PLL). Each voltage input channel has a dedicated ADC board that is mounted in its own metal RF shielding enclosure. Fig. 5.3 shows the photo of an assembled ADC board in its metal box, that is 12 cm×12 cm in size. This ADC board can be powered by a DC power supply at 110 mA, however a clean 12 VDC car battery supply is preferable to eliminate any power line frequency and the switching regulator RF interference used in most of the modern power supplies. The required ± 15 V and ± 5 V supplies for the internal circuitry are generated on-board. Note that the enclosure is connected to the zero voltage reference set by the battery. The BNC input shield is isolated from the chassis to prevent ground loops.

II Serial Optical Interface

The serial optical interface between the master board and each ADC board is implemented with inexpensive TOSLink optical modules and cables, commonly used for digital audio. Each ADC board has its own pair of optical fibers that can be connected to the master board. This optical interface is used to provide galvanic isolations of the ADC boards from each other and from the master board. This feature significantly reduces the possibility of ground loop formations and spurious noise pickups. Serial communication is carried out with a custom data encoding scheme

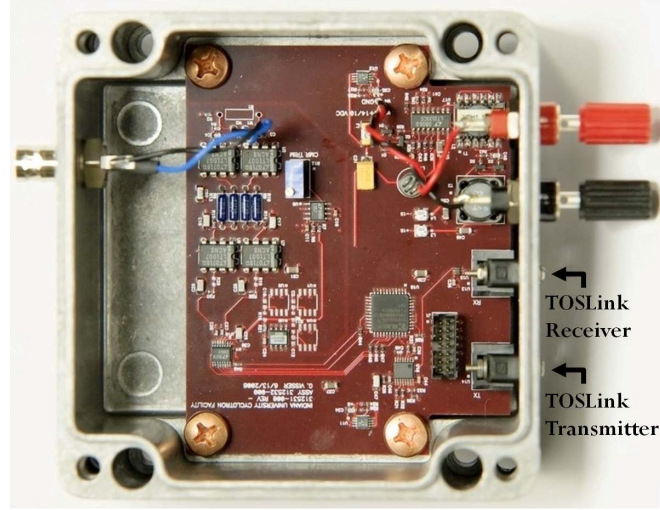


Figure 5.3: Assembled ADC board inside a heavy-duty RF shielding enclosure that is 12 cm×12 cm in size. The analog voltage signal is input into the BNC connector on the left, and the 12 VDC powers is connected through the black and red banana connectors on the right. Two TOSLink optical modules (transmitter and receiver) are also on the right.

that ensures a 50 % duty cycle, allowing its use with both the optical transmitter and receiver. The data encoding scheme also embeds the clock signal in the transmitted data so that the synchronized clock signal (sent by the master board) can be easily recovered using the low cost PLL chip on the individual ADC board.

III Master Board

The master board controls the DAQ sequence, renders communications with the ADC boards, implements packetization of the digitized data from ADC, and provides Ethernet connectivity with the DAQ computer. Fig. 5.4 shows a functional block diagram of the master board. All major functions are contained within a Spartan-3E FPGA [71] made by Xilinx®. The FPGA parses Ethernet packets from, and transmits Ethernet Packets to the DAQ computer. Ethernet connectivity between the computer

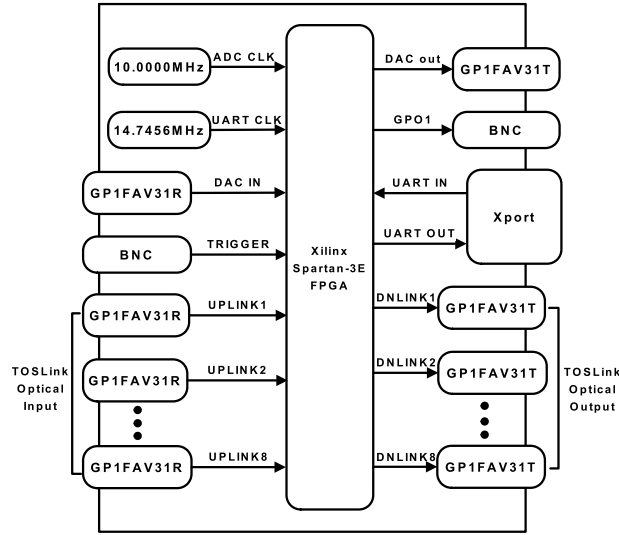


Figure 5.4: Block diagram of the master board.

and the FPGA is implemented with the use of the Lantronix[®] XPort[™] [72] embedded Ethernet device server that provides a RS-232 serial port interface connected to the FPGA. Data is transferred between the device server and the FPGA by way of an universal asynchronous receiver/transmitter (UART) that resides within the FPGA. All UART functions within the FPGA operate on the 14.7456 MHz clock oscillator, from which all standard baud rates can be derived. The Ethernet downlink from the DAQ computer contains data words that control the oversampling rate (OSR) of the ADC. The FPGA transmits the OSR value from the Ethernet downlink to every ADC board over the optical downlink on every rising edge of the trigger input. Every ADC samples its analog input upon receiving the OSR value. As a result, every ADC in the system reads simultaneously upon the trigger input, which defines the sample rate. Data transactions between the master board and the ADC board occur at a baud rate of 625 kbps, which is derived from the 10 MHz clock oscillator.

The CPLD on the ADC board transmits the current sample over the optical uplink each time an OSR value is received. The master board receives the ADC

sample from each ADC board over the optical uplink. Once parsed, all ADC samples are multiplexed, along with a time-stamp, into a first-in-first-out (FIFO) buffer that is implemented in the FPGA. These data frames are stored in the FIFO until a request for data is made by the DAQ computer through the DAQ software (such as MATLAB), at which point it is sent to the device server by way of the RS-232 interface. Finally, the device server transmits the data frames, which contain a time stamp and sample from every ADC channel, over the Ethernet uplink to the DAQ computer.

To expand the capability of the system, the master board also contains another set of optical interface (digital-to-analog converter (DAC) in and DAC out) and a general purpose output (GPO1). The DAC interface, which may be used to control a DAC, is identical to the ADC board interfaces; it uses the same optical connectors. The GPO1 output is capable of driving a $50\ \Omega$ load, making it useful for triggering other devices to be in sync with the DAQ system.

IV Data Acquisition Software

The DAQ software, written in MATLAB, provides data acquisition control, data storage, and data analysis. Ethernet connectivity with the master board is achieved with the free TCP/UDP/IP toolbox [73]. The function is implemented as a MEX-file which allows one to interface C subroutines (dynamic link libraries) to MATLAB. This DAQ software collects data from each voltage monitoring channel at a fixed trigger rate and stores the data to a disk in the DAQ computer. Functions for data analysis such as numerical average or data filtering are also implemented.

5.1.3 Performance Characterization

Performance evaluation of this custom DAQ system is necessary prior to use in the EDM experiment. The significant characteristics that need to be evaluated include the intrinsic root-mean-squared (rms) noise (without load), the cross-talk between

Table 5.1: Maximum bandwidths and ENOBs

OSR	Maximum sampling rate	Measured ENOB	ADC chip Spec. ENOB
64	2.9 kHz	18.0	17.0
128	1.9 kHz	20.4	20.0
256	976 Hz	21.1	21.3
512	488 Hz	21.6	21.8
1024	244 Hz	22.1	22.4
2048	122 Hz	22.6	22.9
4096	61 Hz	23.0	23.4
8192	30 Hz	23.4	24.0
16384	15 Hz	23.8	24.4
32768	7 Hz	24.1	24.6

channels, the settling time, the CMRR, the power supply rejection ratio (PSRR), and the linearity of the system.

I Intrinsic rms Noise

The intrinsic rms noise of the DAQ system stems from noise of the ADC chips and supporting circuitry. On the level of the ADC chip, we expect the intrinsic rms noise to vary with the OSR value, that defines the effective bandwidth of the on-chip digital filter, and the voltage level in the following ways: the rms noise increases by approximately $\sqrt{2}$ when OSR decreases by a factor of 2 from OSR=32768 to OSR=256. An exception is that the rms noise at OSR=128 and OSR=64 has an additional contribution from the internal modulator quantization noise (see Ref. 3). The conversion between the OSR and the sampling can be found in Table 5.1.

To assess the rms noise at all the different OSR values, we collected and analyzed a large amount of data from the DAQ system with the analog input on the ADC board under test terminated. Fig. 5.5 shows the histogram of a typical set of data with a total of 30,000 samples collected at OSR=16384 and OSR=128 with sampling rates of 15 Hz and 1.5 kHz, respectively. Each voltage distribution can be fitted

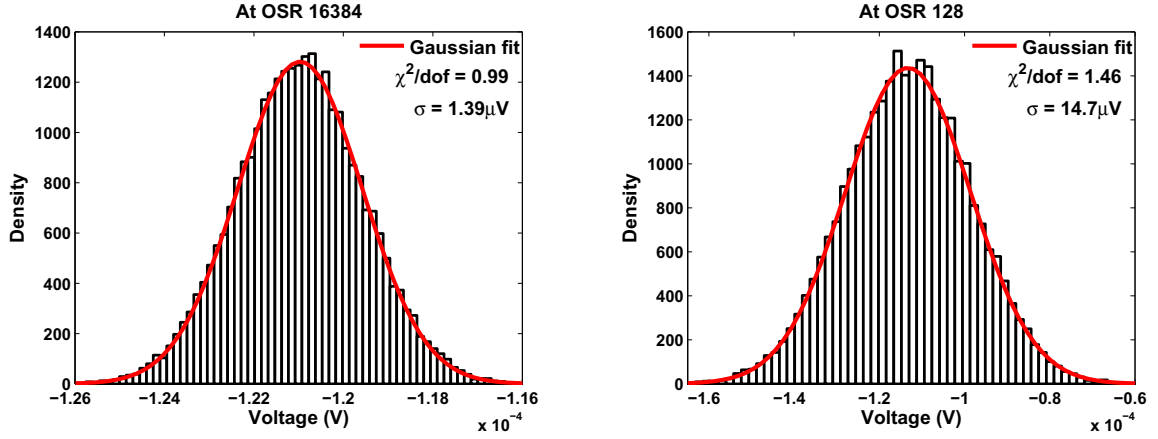


Figure 5.5: Histograms of intrinsic rms noise of the DAQ system at OSR=16384 (left plot) and OSR=128 (right plot). The analog input is terminated in these measurements. The red lines is the Gaussian fit providing the standard deviation of each histograms as the rms noise.

by a Gaussian function that provides the standard deviation, σ , as the intrinsic rms noise. The fit gives an intrinsic rms noise of $1.39 \mu\text{V}$ and $14.7 \mu\text{V}$ at OSR=16384 and 128. These noise figures agree quite well with those from the LTC2440 ADC chip specification [68]. The effective number of bits (ENOB) at OSR=16384 and 128 are measured to be 23.8 and 20.4 respectively, just slightly less than the specified values of 24.4 and 20.0 listed on the ADC chip specification (see Table. 5.1). The DAQ system as a whole does not introduce significantly more noise on top of the intrinsic noise of the ADC chip.

In addition, the power spectral density (PSD)¹ spectra of the noise measurements (shown in Fig. 5.6) do not show any observable peaks, in particular at the AC power supply frequency of 60 Hz and higher-order harmonics. This demonstrates that the

¹PSD measures the distribution of the power of signals of interest over frequency domain and normalizes the power to an equivalent bandwidth of 1 Hz, irrespective of the actual bandwidth, hence, this makes it possible to compare noise measurements executed with different bandwidth settings or different spectrum analyzers.

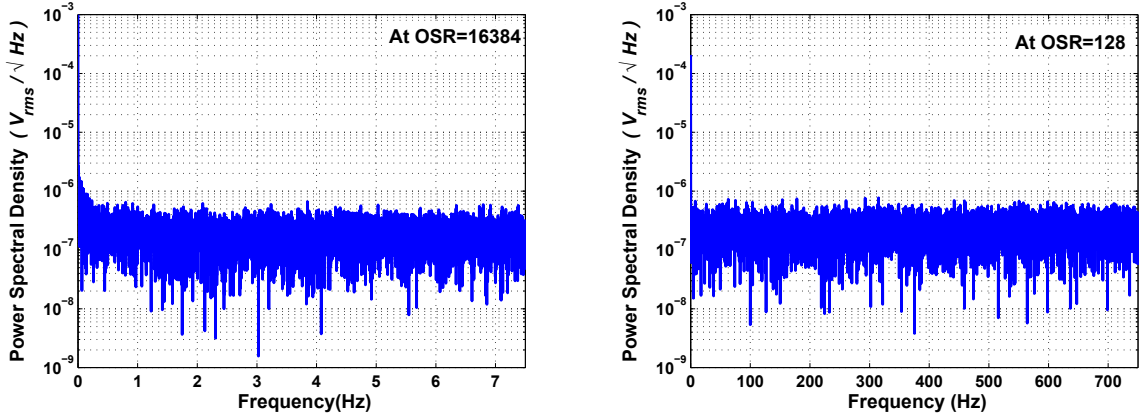


Figure 5.6: Power Spectral Density (PSD) spectra of the intrinsic rms noise of the DAQ system at OSR=16384 (left plot) and 128 (right plot). The vertical axis is in log scale.

DAQ system as a whole has no significant ground loop pickup above the intrinsic noise level. More importantly, there exist no additional sources of spurious noise from trigger or digital switching. Such noise sources give rise to non-Gaussian noise that cannot be suppressed by taking a longer average. The base level of the noise power spectrum of the whole DAQ system is measured to be $0.21 \mu V_{\text{rms}}/\sqrt{\text{Hz}}$ at 1 Hz. Table. 5.1 shows a comprehensive list of maximum bandwidths (equal to half of maximum sampling rate) and measured ENOBs at all available OSR values. Note that the maximum sampling rate at OSR=64 is limited by the maximum XPortTM baud rate of 921600 bps [72].

The intrinsic rms noise of the DAQ system also depends on the voltage level of the analog input. The procedure of this noise test is the same as the preceding noise evaluation, except that a test voltage source is connected to the analog input of the ADC board. For a low noise performance, the test voltage source is made of 1.5 V batteries (Energizer[®] IndustrialTM AA) connected in series. In practice, the battery pack has its own intrinsic noise which would adversely affect the noise measurement

accuracy. The normalized covariance² computation [74] is used to further test whether the noise of the battery is small enough to be negligible. In the test, we utilized two ADC boards to simultaneously sample the voltage output from the same battery pack, with a sampling rate of 15 Hz and an OSR of 16384. We then estimated the extent to which the fluctuations of the data sets collected from the two ADC boards are correlated. A strong correlation would indicate a large contribution of the battery pack noise on the noise measurement. The analysis shows that the normalized covariance is less than 0.1, signifying a weak correlation. This verifies that the battery noise is negligible in this noise measurement. The measured rms noise of the DAQ system as a function of the input voltage level is plotted in Fig. 5.7. The rms noise increases as the input voltage rises. The error bars are statistical and correspond to one standard deviation. We fit the functional dependence of the rms noise using $\sqrt{a + bV^2}$, where a characterizes the intrinsic rms noise without the analog input and b characterizes the noise dependency of the input voltage level. The fit model was chosen to include the independent contributions from the PSD of the noise without loads and the PSD of the noise that varies with the voltage input. The result shows that the rms noise without loads (at $V=0$) is $(1.33 \pm 0.44) \mu\text{V}$, matching the result in the preceding noise test within the error bar.

II Channel Cross-Talk

Cross-talk between individual channels due to any feedthrough coupling, such as mutual capacitance coupling, is one of the primary systematic effects in a DAQ system. To measure the level of channel cross-talk, a 1.5 Hz square wave with an amplitude of 19 V peak-to-peak (V_{pp}), 95 % of full scale input range, was applied to one ADC board and served as an aggressor channel. At the same time, the adjacent ADC board

²Another word is the normalized cross correlation C_{norm} ranging from -1 to 1 which estimates the extent to which two random variables, $f(n)$ and $g(n)$, vary together: $C_{norm} = \frac{\sum f(n)g(n)}{\sqrt{\sum f(n)^2 \sum g(n)^2}}$. The larger magnitude corresponds to the stronger relationship between them.

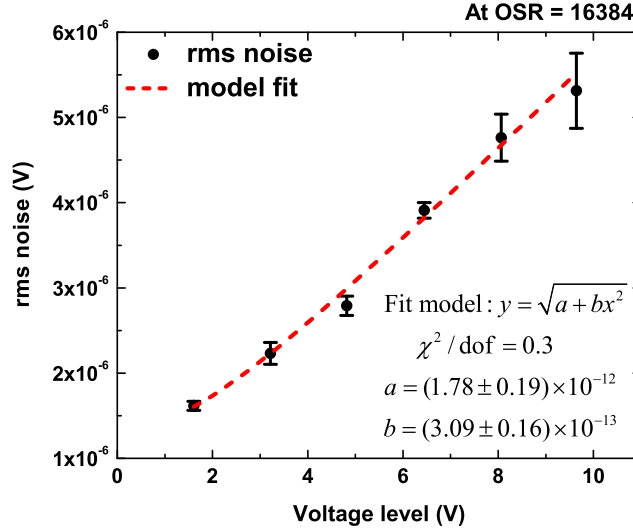


Figure 5.7: Intrinsic rms noise of the DAQ system as a function of the input voltage. The red curve shows the model fit.

with the analog input terminated, as a victim channel, was sampled with an OSR of 512 and a sampling rate of 450 Hz. The digitized data from the victim channel was then averaged under the same cycle of the square waveform of the aggressor channel to reduce the random noise, thereby revealing any small contribution of the cross-talk. Fig. 5.8(a) displays the digitized signal averaged over 41548 cycles from the victim channel. The lack of any square waveform indicates negligible cross-talk effects. The PSD spectra (Fig. 5.8(b)) of both the aggressor and the victim channels also show no measurable correlations between the two channels. In the aggressor channel, peaks at 1.5 Hz and the harmonics are evident, whereas in the victim channel no corresponding peaks are found at these frequencies. In conclusion, our custom DAQ system has a cross-talk smaller than ~ 191 dB, much lower than any commercially available system. The reduction of systematic effect from the channel cross-talk (in particular between the high voltage monitoring and the SQUID monitoring channels) is an indispensable requirement to accomplish the solid-state EDM experiment.

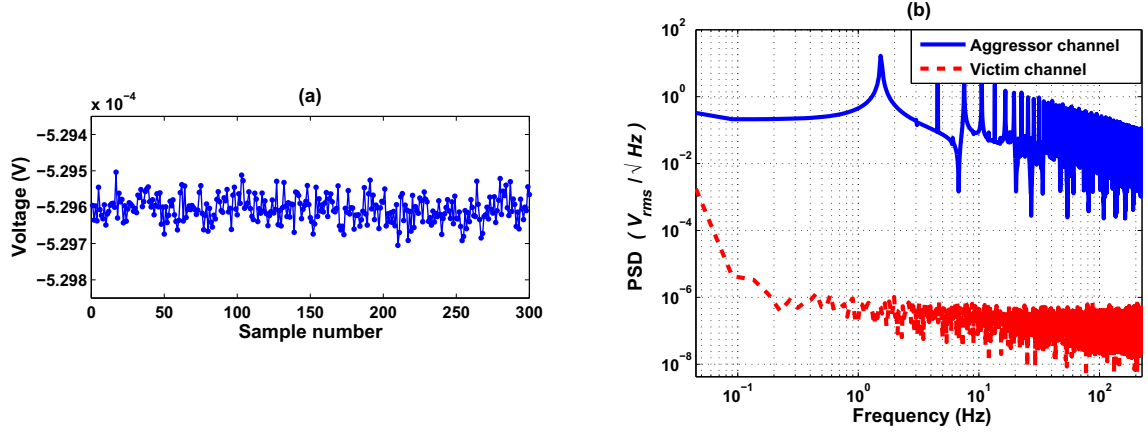


Figure 5.8: Channel cross-talk measurement. (a) Digitized output of the victim channel, averaged over 41548 cycles of the square waveform. (b) PSD spectra of the aggressor channel (blue curve) and the victim channel (red curve) in log-log scale.

III Settling Time

The settling time is defined as an elapsed time during which the output of the DAQ system settles to a desired accuracy. For an accurate EDM measurement, the settling time should be much shorter than the time period to modulate the polarity of the high voltage applied to the GGG samples. Because the high voltage is modulated in a square waveform, the settling time can be a source of systematic effect in the EDM experiment. To measure the settling time of the DAQ system, we supplied a step function as the analog voltage input to the ADC board under test. The step function should settle in a time much faster than the DAQ system. Therefore, we employed a PhotoMos relay (AQV22O) as the test pulser to generate an instantaneous step function with high speed switching time around 0.03 ms [75]. Two types of step input generated from the pulser are applied to the ADC board (see (a) and (c) in Fig. 5.9): one step (a) decreases from 9.5 V to zero and the other step (c) increases from -9.5 V to zero with a frequency of 3 mHz. We collected the step functions for 200 cycles with an OSR of 16384 and a sampling rate of 15 Hz. The averaged results are shown

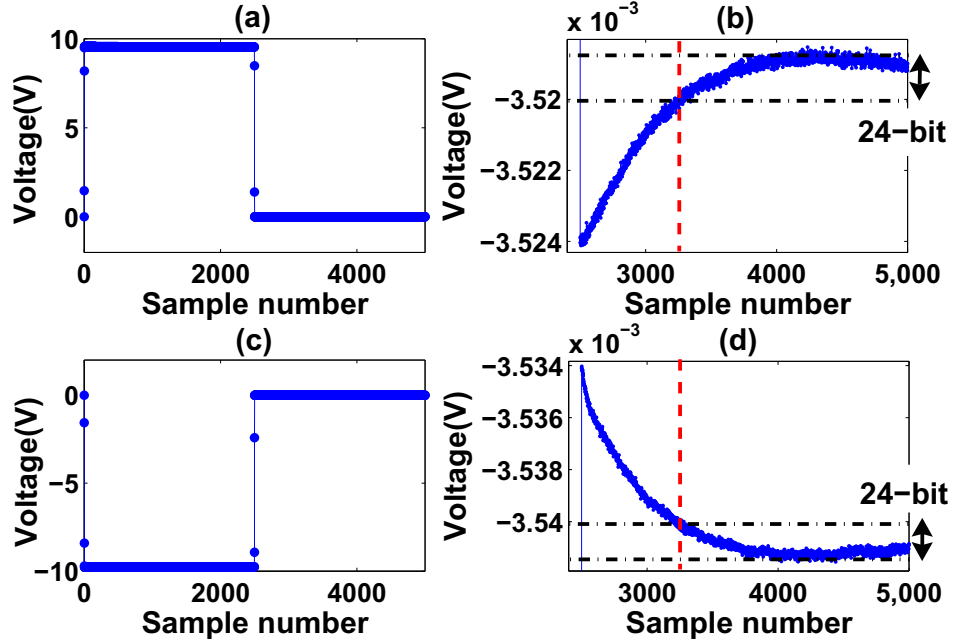


Figure 5.9: Settling time measurement. (a) a step function input with from 9.5 V to 0 V, and (c) a step function from -9.5 V to 0 V. (b) and (d) are zoomed-in voltage plots around the region of voltage transition on (a) and (c). It takes 3 samples to settle the digitized output to the 22-bit resolution (see (a), (c)), and 760 samples to settle to 24-bit resolution (see (b), (d)).

in Fig. 5.9. Upon the voltage switch, the digitized output settles to 22-bit resolution within three samples, corresponding to a settling time of 200 ms (Fig. 5.9(a) and (c)). To settle to 24-bit resolution, it takes 760 samples that correspond to a much longer time of around 51 s (Fig. 5.9(b) and (d)).

IV Common Mode Rejection

Before the analog signal is digitized by the ADC, some undesirable common-mode noise (picked up from any ambient sources) is always present on both the high and low input wires of the ADC board, equal in both the phase and amplitude. This common-mode noise is quite often generated by capacitive couplings between the wires and

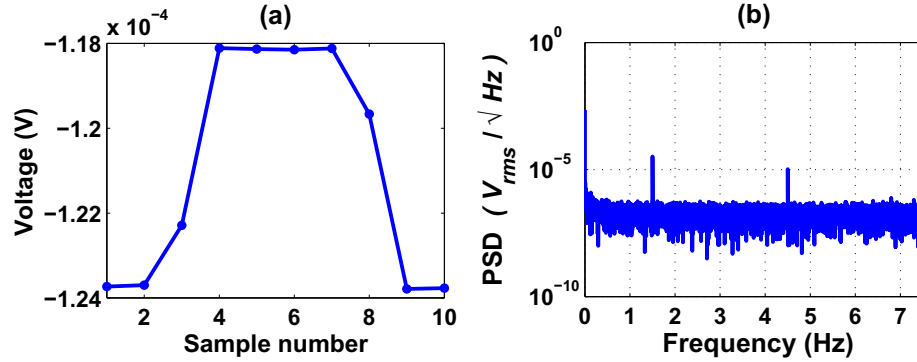


Figure 5.10: Common-mode rejection test. (a) Digitized output averaged over 7199 cycles. (b) The PSD spectrum of the output of 10,000 samples. The high and low analog inputs are connected to a common voltage source.

ground. For the best performance, the DAQ system must sufficiently suppress the common-mode noise so as not to add additional noise, and in the mean time not to distort any voltage input of interest. To measure the CMRR of the DAQ system, we connected both the high and low inputs of the ADC board under test to a common voltage source of a 1.5 Hz square waveform with a $4 V_{pp}$ amplitude. Data was collected at $OSR=16384$ with a sampling rate of 15 Hz. Fig. 5.10(a) shows the digitized data averaged over 7199 cycles. Notice that even with a square wave as the input, the averaged output waveform is distorted because of the discrepancies on the phase and amplitude between the high and low analog inputs, as a result of the common-mode rejection adjustment. The PSD spectrum is shown in Fig. 5.10(b), where the apparent peak at 1.5 Hz (and 4.5 Hz) is measurable, which indicates some degree of CMRR. By comparing the amplitude of the output, $5.68 \mu V_{pp}$, to the applied waveform strength of $4 V_{pp}$, the CMRR is estimated to be 1 ppm, which is sufficient for the EDM experiment.

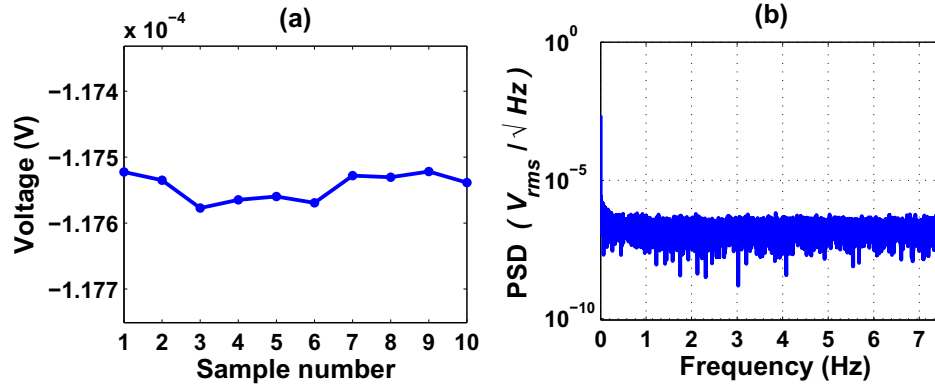


Figure 5.11: Power supply noise measurement. (a) Digitized data averaged over 4798 cycles. (b) The PSD spectrum of the output (with a terminated input) of 10,000 samples

V Power Supply Rejection

Even with the most careful choice, inevitably the DC power supply used to operate the ADC board has some degree of noise, such as voltage ripples, that can adversely affect the performance of the DAQ system. This unwanted noise from the power supply can parasitically couple to the analog voltage input through the circuitry, thereby adding undesirable noise to the digitized output. We quantified the ability of the DAQ system to reject the power supply noise by: a) mixing a 1 V_{pp}, 1.5 Hz square wave together with a 12 VDC to create a “rippled” supply voltage; b) terminating the analog input of the ADC board under test; and c) collecting digitized data with an OSR of 16384 at a sampling rate of 15 Hz. The resulting data averaged over 4798 cycles is plotted in Fig. 5.11(a) with the PSD spectrum plotted in Fig. 5.11(b). The time trace of the averaged data does not show any square wave corresponding to the power supply ripple. No observable peak at the frequency of the ripple is found in the PSD spectrum, either. In summary, the PSRR of the DAQ system is quite high, and the noise from the power supply is negligible even with a bad power supply with large ripples.

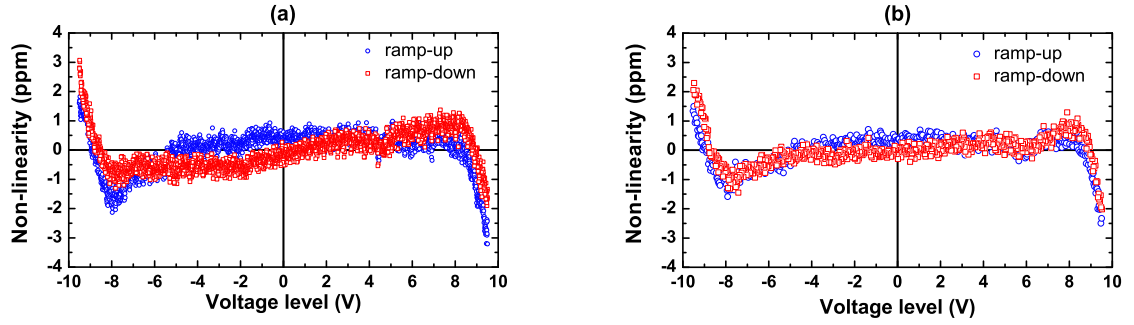


Figure 5.12: The non-linearity of the DAQ system as a function of the input voltage. (a) with a 0.01 Hz triangular waveform. (b) with a 0.04 Hz triangular waveform. The maximum non-linearity of the DAQ system is ± 3 ppm over the full input range.

VI Linearity

The linearity of the DAQ system characterizes how accurately a digitized result reflects the analog input. Measurement of the linearity of a high-resolution DAC system is especially difficult due to the lack of a good calibration source. We have tried several commercial voltage sources with sinusoidal waveform output, but found that the total harmonic distortion and phase error are too large to be useful in order to carry out this test. Instead, we used the newly developed low-distortion, 20-bit precision DAC board (described in Sec. 7.2.3) as the voltage source. An input of 0.01 Hz triangular waveform with a 19 V_{pp} amplitude generated by the DAC board is fed into the ADC board under test and sampled at OSR=4096 with a sampling rate of 50 Hz. We performed a least-square line fit ($y = a + bx$) to one cycle of the digitized output, separating the ramping down half-cycle from the ramping up half-cycle. The non-linearity is quantified by the residual deviation from the ideal triangular waveform.

Fig. 5.12(a) shows the non-linearity (in ppm) as a function of the input voltage. The line fit has $\chi^2/\text{dof} = 0.94$ and 0.75 on ramp-down and ramp-up halves, respectively. The maximum non-linearity of the DAQ system is estimated to be ± 3 ppm

over the full input range (± 1 ppm between voltage range of ± 7 V). This is sufficient for the EDM experiment. The non-linearity of this DAQ system arises mainly from the LTC2440 ADC chip, with some small contributions from op-amps and resistors in the input stage and buffer stage of the ADC board (Sec. I). In practice, this measured non-linearity should be the combined effect from the DAC board and the DAQ system, however, without an independent calibrated voltage source we cannot isolate the non-linearity of the DAQ system. Nevertheless, the measured non-linearity is already close to the specification of the ADC chip and thus implies that errors from the DAC board are probably insignificant. The small 1 ppm discrepancy between the ramp-up and ramp-down data sets (Fig. 5.12(a)) is probably a result of the temperature change lagging some time behind the voltage change. Increasing the frequency of the triangular waveform reduces this discrepancy as shown in Fig. 5.12(b) that indicates the non-linearity of the DAQ system measured with the 0.04 Hz triangular waveform.

5.1.4 Conclusion

A high resolution 24-bit DAQ system with special attention to the noise performance in order to improve the EDM experiment has been developed [76]. The detailed characterizations of the relevant parameters of the DAQ system are shown. The measured ENOB can be as high as 24.1 when sampled at 7 Hz. The EDM measurement requires a sampling rate at ~ 700 Hz, and the DAQ system has a ENOB of 21.1. The most important performance requirement is the ultra-low channel cross-talk which reduces the leading systematic effect observed in the EDM experiment. Using this custom DAQ system, the feasibility of the solid state method for the electron EDM search will be demonstrated.

5.2 Low Distortion HV Polarity Switch System

In addition to the development of the low-noise, high-resolution DAQ system, a low distortion HV polarity switch system utilizing vacuum-tube triodes has been built in order to improve the flatness of the HV supplies to the samples. In this section, the hardware and performance of the HV polarity switch system will be described, with special attention given to voltage drift.

5.2.1 Motivation

At the start of the EDM experiment, a commercially available HV polarity switch system (Brandenburg 2540-301) was employed to generate the electric fields which magnetize the GGG sample. With this HV system, a non-zero spurious electron EDM signal was observed. Careful studies of the relation between applied HV, measured leakage currents and SQUID readouts have been made for discerning the major causes of the background. The developed DAQ system provided the essential tool for unbiased correlation studies in which HVs in a square waveform with frequency 2.9 Hz and amplitude ranging from 0.48 kV_{pp} to 5.83 kV_{pp} were applied across the GGG samples through the HV electrodes in an individual measurement sequence, and then leakage currents and SQUID signals were monitored. The voltage signals of interest were continuously collected for 3 hours with a sampling rate of 1.16 kHz. The maximum strength of HV that can be applied to the samples was limited by the instability of the SQUID sensor. This limitation was later significantly improved by replacing HV-related components.

Fig. 5.13 shows zoomed-in plots of the applied HVs monitored through a 1000:1 voltage divider where (a) and (b) show positive and negative top, respectively. It can be seen that the voltage drift (dV/dt) from the HV system is as large as a few ten V/s. The considerable voltage drift on the nominal ± 0.6 kV voltages leads to a non-zero displacement current through the relation of $I = CdV/dt$ flowing directly in

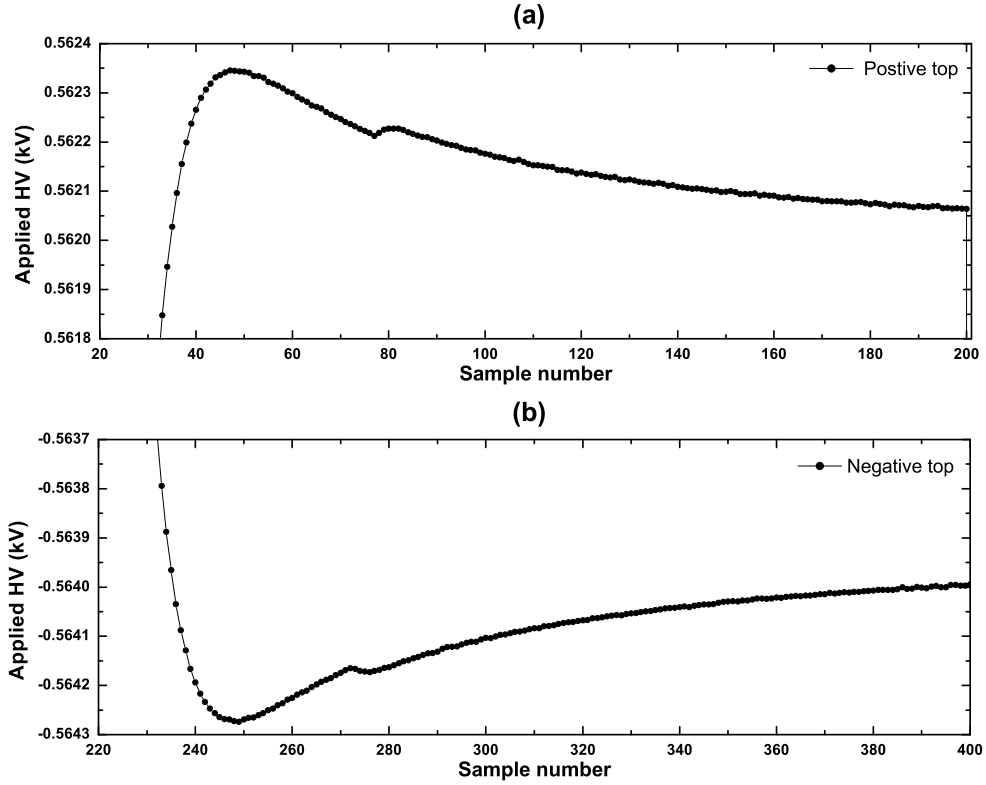


Figure 5.13: Time trace of the applied HV averaged for 3 hours: (a) positive top of 0.5 kV and (b) negative top of -0.6 kV.

and out of the HV electrodes. This current produces a magnetic field in phase with the polarity of the HV, resulting in a non-zero offset mimicking the EDM-induced magnetization, assuming that the normal of the pickup coil is not perfectly aligned with the electric field lines. Accordingly, the magnetic signal induced by dV/dt might be one of the sources generating spurious EDM signals in the EDM experiment. The displacement current also flows on the ground electrodes (see Fig. 4.1), hence it can be detected by the leakage current monitor.

The correlation between the measured leakage current and voltage drift is plotted in Fig. 5.14(a). The leakage currents increase linearly at higher voltage drift, which shows that it is mainly coming from the voltage drift. According to the line fit

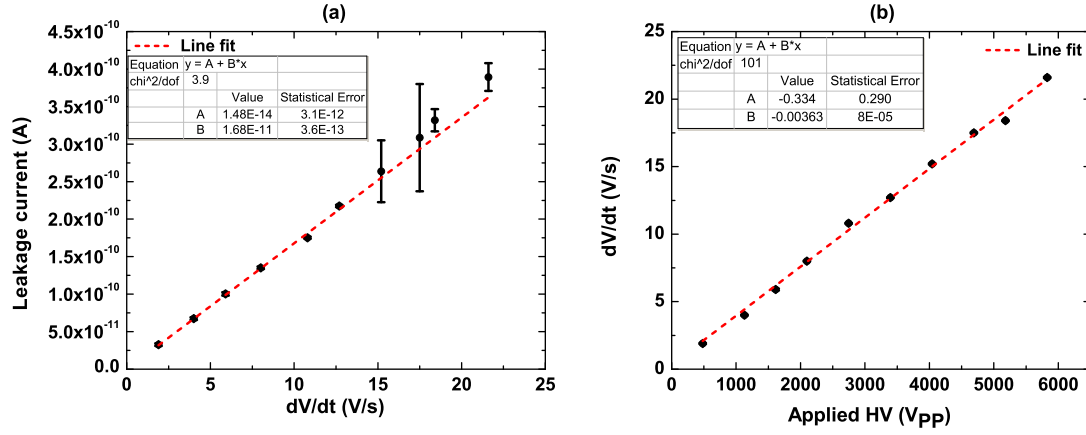


Figure 5.14: Correlation between the measured leakage current and the applied HV: (a) the measured leakage current as a function of the voltage drift, (b) the estimated voltage drift as a function of the applied HV.

performed on the plot, the capacitance of GGG is estimated to be (16.8 ± 0.3) pF because the slope of the plot signifies the capacitance (recall $I = C dV/dt$). The result matches that presented in Sec. 3.4. The constant term of the fit indicates that zero voltage drift does not induce the current flowing on the electrodes. This verifies the accuracy of the correlation study. Fig. 5.14(b) shows the degree of voltage drift from the HV polarity switch system as a function of the applied HV. Increasing HV produces a linear increase of voltage drift. For example, the drift at the maximum applied HV of 5.8 kV_{pp} in this study is measured to be 21 V/s , which corresponds to a leakage current of 400 pA . In accordance with the line fit, when 10 kV_{pp} is applied (maximum strength which can be generated by the HV system) to the HV electrodes, the dV/dt is expected to be 36 V/s which would generate a leakage current of 600 pA . This leakage current generates enormous magnetic flux in the vicinity of the sample, too large for carrying out the EDM experiment. Although the SQUID sensor is not susceptible to the radial field generated by the magnetic flux, some fraction of the field can be enclosed by the flux pickup coil due to its slight tilt. Fig. 5.15(a) shows

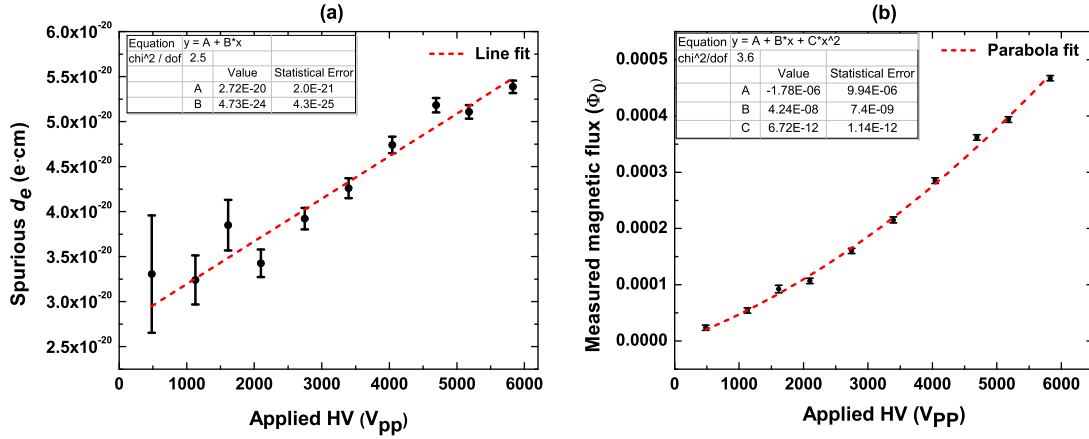


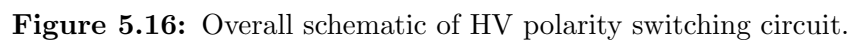
Figure 5.15: (a) Measured spurious electron EDM as a function of the applied HV. (b) Measured spurious magnetic flux as a function of the applied HV.

the spurious electron EDM value determined by Eq. 4.14 as a function of the applied HV. A very large spurious electron EDM on the order of 10^{-20} e-cm is measured, and it is linearly dependent on the strength of the applied HV, confirming that the major background originates from the magnetic field associated with the voltage drift from the HV polarity switch system used here. Due to this spurious electron EDM signal, the measured magnetic flux Φ_{sq} has a quadratic term as shown in Fig. 5.15(b): with the relation $d_e = A + BV$ from Fig. 5.15(a), $\Phi_{sq} = A'V + B'V^2$.

As a result, the careful correlation studies have uncovered that the major systematic effect comes from the voltage drift produced by the HV polarity switch system. Therefore, to eliminate this source of background, the voltage drift needs to be sufficiently suppressed. A new HV polarity switch system has been designed and developed to replace the Brandenburg 2540-301 HV system.

5.2.2 Description of New HV Polarity Switch System

The new HV polarity switch system consists of two main components: a HV polarity switch circuit and feedback circuit. The former plays an important role to amplify an



I HV Polarity Switch Circuit

Fig. 5.16 shows the overall diagram of the HV polarity switch circuit that can be divided into three primary functions: components in black color switch the HV polarity as well as amplify and drive input signal, components in red serve as a filament drive to a vacuum-tube triode, and components in blue control the grid voltage of the vacuum-tube and the frequency of HV output. In order to handle the HV polarity switching between ± 5 kV, the vacuum-tube triodes (6BK4C) are connected in series

to the positive and negative DC HV supplies (Standard Research PS350). The HV system contains two output channels, Ch1 and Ch2, which are designed to generate HV of opposite polarities. Each output channel needs to operate alternatively two vacuum-tubes where one manages the positive HV (A and D) and the other manages the negative HV (B and C). The HV electrodes are connected to either of the HV output channels.

Operation of the vacuum-tube triode, composed of a plate, grid, cathode, and heater, requires a filament drive to the heater so as to indirectly heat the cathode. The heater applies thermal energy to the cathode so that it can reach its operating temperature at which thermionic emission of electrons can occur. An audio power amplifier LM2876, which maintains an excellent signal to noise ratio of greater than 95 dB [77], is used for generating the proper filament drive. With its gain set to 21 using supporting electronic components, a sine waveform with an amplitude of $0.31 V_{\text{rms}}$ and a frequency of 20.12 kHz is supplied to the input of LM2876 and the amplified output of $6.5 V_{\text{rms}}$, which is the required magnitude for the AC filament drive [78], is output. Since the vacuum-tube handles high voltage, a home-made transformer is supplemented to isolate the circuitry of LM2876 from the high voltage. The ratio of the number of turns in the secondary winding to that in primary winding is adjusted to be 1:1. The amplified output from the LM2876 passes through all four transformers in the HV system simultaneously and then powers the heaters of all the vacuum-tubes.

Once the filament drive is provided to the heater, a large number of electrons are emitted from the cathode. The electrons are attracted to the plate, positively charged with respect to the cathode, and in turn create the plate current (I_p) inside the vacuum-tube. The vacuum-tube triode serves as a HV switching regulator. To be specific, consider the vacuum-tube A in Fig. 5.16. With the plate connected to the DC HV of 5 kV, I_p is allowed to flow through the phototransistor FPT1000A assuming that the photodiode (LED) is on. The resistor of 11Ω between the cathode

of the vacuum-tube and the collector of the phototransistor causes a voltage drop, making the grid voltage negative with respect to the cathode. The grid functions generally as a controller of the plate current flow without attracting the electrons to itself. Since the grid is generally manufactured in the form of a spiral or wire mesh, the electrons can easily pass through the grid to reach the plate. The relative grid voltage with respect to the cathode, V_g , needs to be set negative so that generation of the grid current and the accompanying power loss do not come out. The V_g to I_p characteristics of the vacuum-tube used here are found in Ref. [78]. When the LED is on, the voltage drop arising from both the $11\ \Omega$ and FPT1000A is measured to be lower than 1 V, i.e., $-1\ \text{V} < V_g < 0\ \text{V}$. Therefore, a plate current ranging from 0.3 mA to 0.7 mA flows in accordance with the characteristics. In this case, a positive HV can be generated on the output channel named Ch1 out on Fig. 5.16 and monitored by the 1000:1 voltage divider named Ch1/1000 on the figure. On the other hand, when the LED is off, the plate current cannot flow through the phototransistor; instead it is diverted to the $120\ \text{k}\Omega$ resistor. That leads to a larger voltage drop so that V_g is smaller than $-3.5\ \text{V}$ which is the cut-off voltage for I_p . When $V_g < -3.5\ \text{V}$, the electrons from the cathode are unable to be captured by the plate and they turn back to the cathode due to the large negative voltage on the grid. Accordingly, in this case, no I_p flows on the circuit and the desired positive HV is not generated.

The HV polarity switch circuit works in such a way that the LEDs on the side of vacuum-tubes B and D are on when the LEDs on the side of vacuum-tube A and C are off and vice versa, thus Ch1 generates the positive (negative) HV output when Ch2 generates the negative (positive) HV output. This HV switching control is accomplished in conjunction with the feedback circuit which will be presented later. The zener diode connected in parallel to the phototransistor has been added to protect the transistor when a large current tries to flow into the transistor in the reverse direction from the emitter to the collector by directing the current to flow through itself.

The grid voltage V_g on each vacuum-tube is controlled through the opto-isolator driven by an arbitrary waveform generator. The opto-isolator is comprised of the combination of FPT1000A and LED. The LED converts the arbitrary waveform drive signal into the light output proportional to the drive signal. Once the FPT1000A senses the light, it allows the plate current to flow through itself. The degree of voltage drop on the FPT1000A depends on the strength of the drive signal. As an example, a higher strength of drive signal results in a smaller voltage drop on the FPT1000A and in turn V_g becomes larger though still $V_g < 0$. According to the V_g - I_p characteristics, higher V_g tolerates higher I_p so that higher HV output can be generated. Based on this method, not only are different waveforms of drive signal amplified by a factor of 1000, but also the frequency of the HV output is controlled. As shown in Fig. 5.16, one sine wave is simultaneously applied across each LED located in the Ch1 HV generator while the other, 180 degrees out of phase with the sine wave, is applied across each LED in the Ch2 HV generator. In the Ch1 HV generator, the first half of the sine wave (with negative value) operates only the LED on the side of vacuum-tube B, leading to the flow of the corresponding plate current. Then, the HV output, in the same shape and amplified by a factor of 1000, is generated on the Ch1 output channel. The second half with positive value operates only the LED on the side of vacuum-tube A, leading to the same shape and amplified HV output on the output channel. As a result, the combined HV output during one period amplifies the sine wave by a factor of 1000 with the same frequency. In the Ch2 HV generator, the reverse phenomena to Ch1 occurs: the plate current flows on the vacuum-tube D and C during the first and second half respectively, thereby the HV output with polarity opposite to the Ch1 HV output is generated.

The LED of the opto-isolator typically induces an undesired voltage clamp on the HV output owing to its on-voltage (V_d) above which the LED becomes a conductor. When the drive signal is a sine waveform on the Ch1 HV generator, only the voltage regions above V_d can lead to operation of the LED on the side of the vacuum-tube

A (see Fig. 5.16), therefore the voltage regions are only amplified and generated on the output channel. On the other hand, regions below V_d do not allow the LED to make light output, hence the regions are generated as a zero voltage on the output channel resulting in distorted HV outputs. This phenomenon is called the voltage clamp. Different LEDs have different values of V_d . For the LEDs used here, the V_d are measured to be around 2.7 V. To effectively eliminate such a voltage clamp phenomena, potentiometers and ± 15 VDC sources are additionally connected to the LEDs as shown in Fig. 5.16. The LEDs on the side of vacuum-tube A and D generate the light output signals to the FPT1000A only when the drive signal is positive with respect to their cathode. Therefore, each potentiometer is carefully adjusted to make the voltage at the cathode of each LED exactly equal to minus each V_d , so that all positive regions of the drive signal are relatively larger than V_d . This modification makes it possible for all positive voltage regions to be amplified and output without any voltage clamp. Likewise, since the LEDs on the side of vacuum-tubes B and C work only when the drive signal is negative with respect to the cathode, the voltages at their cathodes are adjusted to be exactly equal to their own V_d . With this trick, all negative voltage regions of the drive signal lead to the plate current flow and they are successfully generated as the HV output. This method, which is the same as the typical diode drop compensation [79], in conjunction with fine adjustment of the individual potentiometer for each LED, allows successful elimination of the voltage clamp phenomena on the HV output.

In order to monitor the generated HV output, the 1000:1 voltage dividers are employed. The supplementary 30 nF HV-compatible capacitors are connected in parallel to each HV output channel to reduce the transient ramp speed at every field reversal. This results in a reduction of the displacement current which is one of the leading systematic effects in the GGG-based EDM experiment.

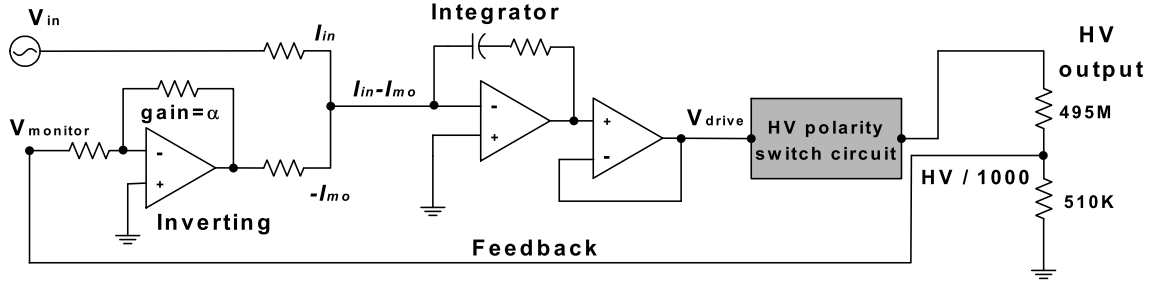


Figure 5.17: Simplified idea of the feedback circuit.

II Feedback Circuit

The raw HV output from the HV polarity switch circuit can be distorted, which is exactly 1000 times the drive signal, during the process of amplification. The feedback circuit has been additionally designed in order to compensate for unwanted signal distortion. The main objective of the circuit is to measure the degree of the distortion and then manipulate the reference input signal V_{in} generated by an arbitrary function generator depending on the measured distortion. The adjusted reference signal as the drive signal V_{drive} is supplied to the HV polarity switch circuit, resulting in improved HV output. The simplified strategy is schematized in Fig. 5.17. First an estimate of the distortion on the HV output with respect to V_{in} is performed by monitoring the HV output divided by 1000, $V_{monitor}$, from the HV polarity switch circuit. $V_{monitor}$ is inverted with a gain of α followed by adding it to V_{in} . Then the added output, $V_{in} - \alpha V_{monitor}$, is integrated by an inverting integrator and its output enters into the HV polarity switch circuit as V_{drive} . Consequently, V_{drive} can be expressed as

$$\begin{aligned}
 V_{drive} &= \frac{1}{RC} \int (V_{in} - \alpha V_{monitor}) dt \\
 &= \frac{1}{RC} \left[\int (1 - \alpha) V_{in} dt - \int \alpha (V_{monitor} - V_{in}) dt \right] \quad (5.1)
 \end{aligned}$$

where the first term in parenthesis corresponds to the signal proportional to V_{in} and the second term denotes the error (distortion) signal between the HV output and reference signal. Proper values of α , R , and C improve the efficiency of the feedback

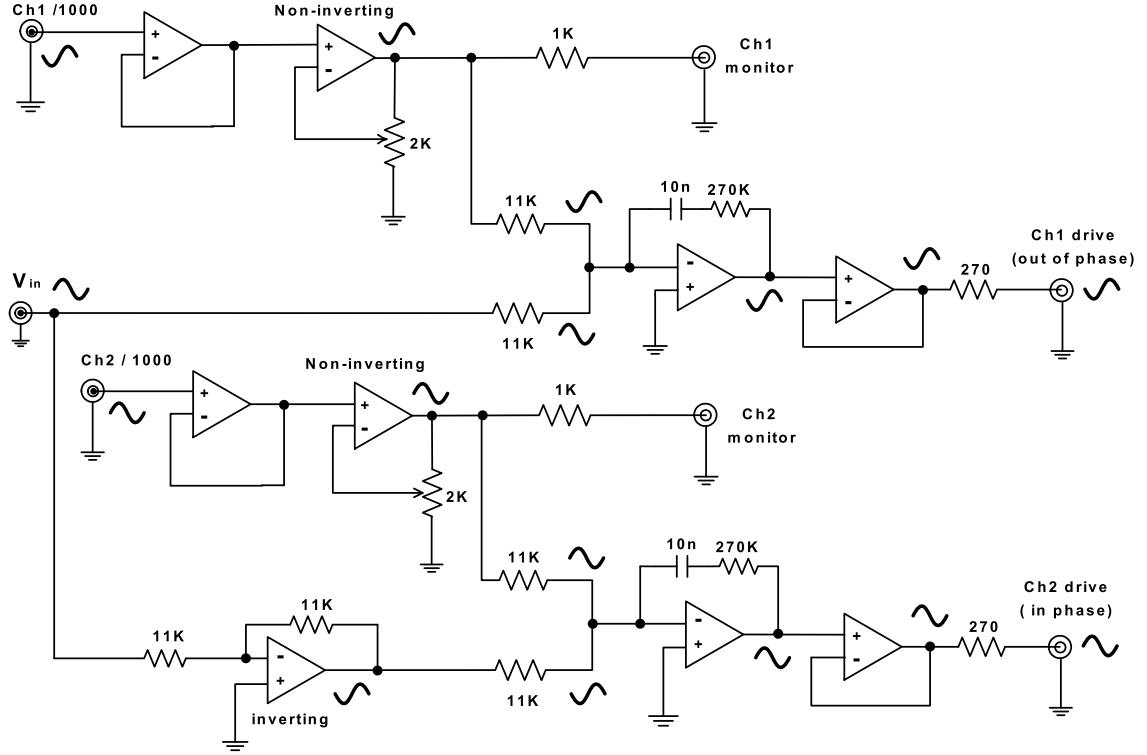


Figure 5.18: Overall circuit schematic of feedback circuit.

circuit. The V_{monitor} improved by V_{drive} is supplied to the feedback circuit again and the same process is repeated to obtain the best result.

The overall schematic of the designed feedback circuit is shown in Fig. 5.18. The HV outputs divided by 1000 are supplied to the feedback circuit as V_{monitor} . The followers (OP27) in the initial stage are added for isolation between the HV output and the feedback circuit. The follower prevents the high voltage from directly flowing into the feedback circuit, which might happen when the 495 M Ω resistor is accidentally broken or changed into a smaller resistor. Therefore, the main components in the feedback circuit can be effectively protected. The follower also changes the high input impedance of V_{monitor} into a few tens of Ω , thus no error occurs at the stage of

the non-inverting amplifier.

As shown in Fig. 5.18, a sine wave as V_{in} is provided to the input channel on the feedback circuit. $V_{monitor}$ from Ch1, out of phase with V_{in} , is amplified by the non-inverting amplifier with a certain gain properly adjusted by the 2 k Ω potentiometer and then combined with V_{in} to estimate its distortion. The inverting integrator then generates the improved output of V_{drive} that is still out of phase with V_{in} . The best values for R and C are found to be 270 k Ω and 10 nF. The additional follower right after the integrator is used to reduce the output impedance. The same process occurs with Ch2 except that because $V_{monitor}$ from Ch2 is in phase with V_{in} , V_{in} is inverted using the inverting amplifier with a gain of 1 to measure its distortion. The finally stabilized V_{drive} signals are loaded across the LEDs in the HV polarity switch circuit. The measurement of the HV outputs on each channel is performed by connecting the supplementary Ch1 and Ch2 monitors in the feedback circuit to the analog input of the ADC boards.

Based on the circuit designs mentioned above, the HV polarity switch system has finally been assembled. A photograph of the assembly is shown in Fig. 5.19. All vacuum-tubes are safely loaded on the transparent acrylic board with sockets. The amplifier LM2876 related to the filament drive is usually generating heat during operation and easily becomes hot, hence it has been mounted on a small piece of metal to absorb and remove its heat. Since the feedback circuit needs to be well-shielded from external noise sources, it has been enclosed by a metal box.

5.2.3 Voltage Drift on the HV Polarity Switch System

The most significant performance characterization of interest is the degree of voltage drift on the HV output generated by the HV polarity switch system. The causes of the drift would come from the reference signal itself as well as electronics components in the HV system such as op-amps, vacuum-tubes, or resistors. The EDM experiment needs HV sources in a square waveform with a low frequency, hence evaluation of

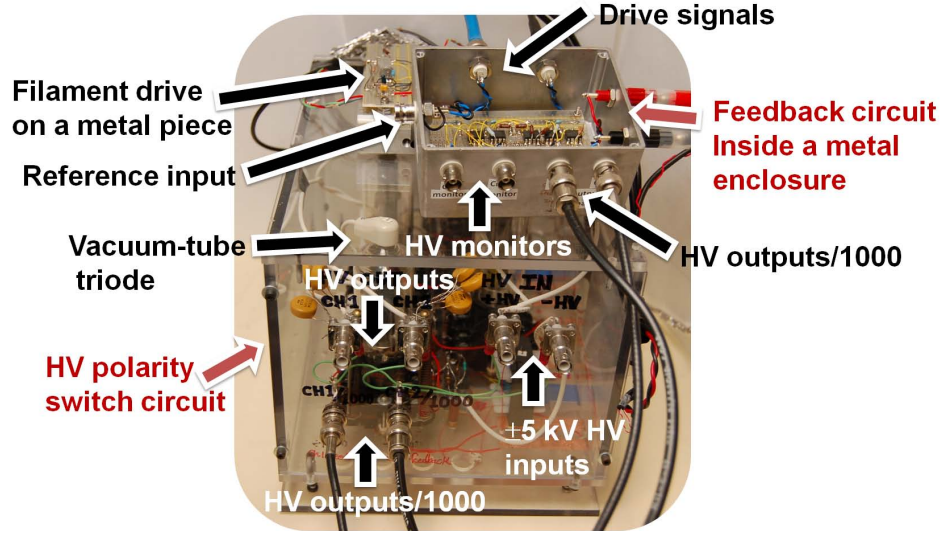


Figure 5.19: Photograph of the assembled HV polarity switch system.

the performance is accomplished by a square waveform generated by two different function generators.

One square waveform to drive the HV polarity switch system is generated by the 20-bit SRS DS360 function generator. Because the EDM experiment is planned to be operated at the polarity switching cycle of 1.43 Hz (see Chap. 6), the drive signal is chosen to be at the same frequency as well as 5 V_{pp} amplitude. The signal is supplied to V_{in} on the feedback circuit as the reference signal and then the 24-bit DAQ system collects data from the Ch1 and Ch2 HV monitors on the feedback circuit as well as the reference signal with an OSR of 256 and a sampling rate of 715 Hz. Fig. 5.20 shows the digitized outputs averaged over 35849 cycles. The HV output on Ch1 is out of phase with the reference signal while the output on Ch2 is in phase as mentioned before. In contrast to the reference signal, the HV outputs show a voltage overshoot at every field transition region, indicating that the overshoot is originating from the electronic components. The rising and falling time of the HV outputs, two times bigger than that of the reference signal, is due to the supplementary 30 nF and the capacitance (~ 100 pF) of the SHV cables.

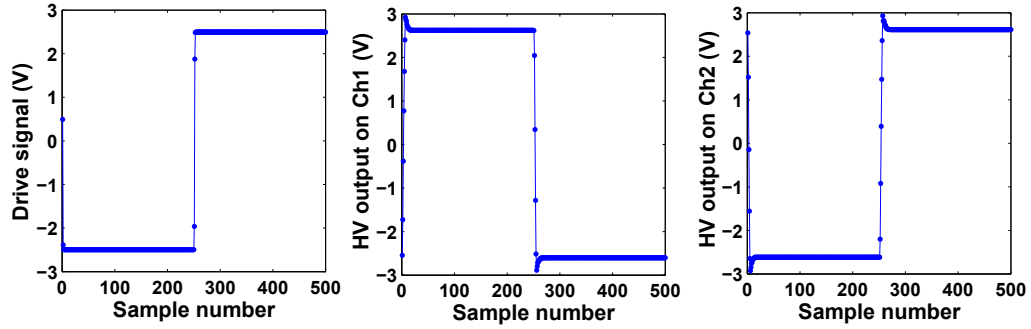


Figure 5.20: Digitized output of drive signal and HV monitor outputs on Ch1 and Ch2, averaged over 35849 cycles.

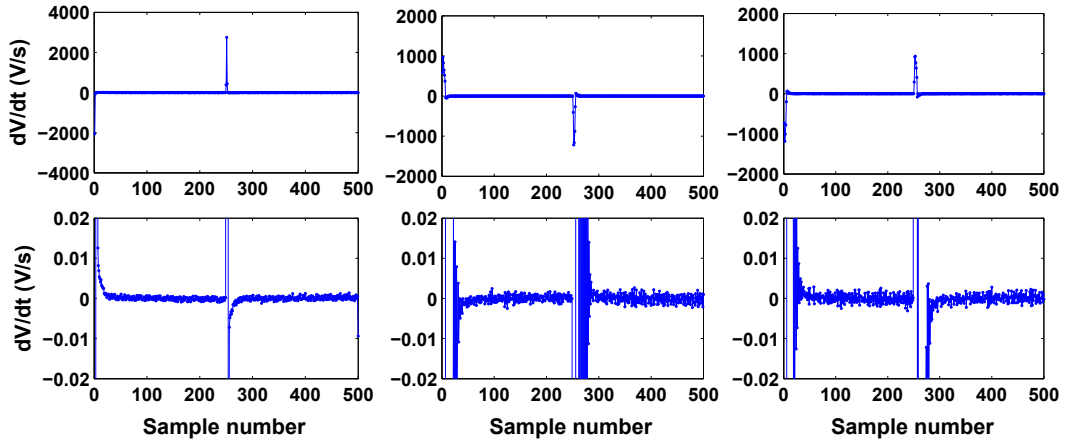


Figure 5.21: Time derivative of drive signal and HV monitor outputs on Ch1 and Ch2. Plots in the second row are zoomed-in views.

Fig. 5.21 indicates the time derivative of the reference signal and HV outputs divided by 1000 on Ch1 and Ch2, and their zoomed-in plots are shown in the second row. The voltage drift dV/dt of the signals is calculated within the last 30 % of each half cycle. The results are summarized in Table 5.2. Note that the actual dV/dt of HV outputs from the HV system is equal to 1000 times that of HV monitor outputs. It turns out that dV/dt of HV outputs are almost the same as that of the reference

Table 5.2: dV/dt of drive signal from the DS360 function generator and HV monitor outputs evaluated in the last 30 % of the half cycle.

dV/dt	reference signal	Ch1 HV monitor	Ch2 HV monitor
first half	$(-166.3 \pm 0.3)\mu\text{V/s}$	$(166.6 \pm 0.5)\mu\text{V/s}$	$(-175.2 \pm 0.8)\mu\text{V/s}$
second half	$(216.2 \pm 0.3)\mu\text{V/s}$	$(-232.3 \pm 0.6)\mu\text{V/s}$	$(224.2 \pm 0.7)\mu\text{V/s}$
average^a	$(-191.3 \pm 0.2)\mu\text{V/s}$	$(199.5 \pm 0.4)\mu\text{V/s}$	$(-199.7 \pm 0.5)\mu\text{V/s}$
real value^b	$(-191.3 \pm 0.2)\text{mV/s}$	$(199.5 \pm 0.4)\text{mV/s}$	$(-199.7 \pm 0.5)\text{mV/s}$

^a(first half -second half)/2

^b1000 times the averaged dV/dt

signal (discrepancy is only 4 %), indicating that the voltage drift of the HV system is limited by the reference signal. This custom HV system improves the distortion of voltage drift by a factor of 100 over its predecessor Brandenburg 2540-301. The expected leakage current through $I = CdV/dt$ is estimated to be around 3 pA.

The other square waveform with 1.43 Hz and 5 V_{pp} to drive the HV polarity switch system is generated by a 16-bit Agilent 33220A function generator. The same procedures as the previous performance test were repeated and the results are summarized in Table 5.3. It is also seen that the reference signal is the dominant source

Table 5.3: dV/dt of drive signal from the 33220A function generator and HV monitor outputs evaluated in the last 30 % of the half cycle.

dV/dt	reference signal	Ch1 HV monitor	Ch2 HV monitor
first half	$(133.6 \pm 0.3)\mu\text{V/s}$	$(-133.8 \pm 0.3)\mu\text{V/s}$	$(152.6 \pm 0.6)\mu\text{V/s}$
second half	$(-295.2 \pm 0.7)\mu\text{V/s}$	$(304.7 \pm 0.4)\mu\text{V/s}$	$(-317.4 \pm 0.5)\mu\text{V/s}$
average^a	$(214.4 \pm 0.4)\mu\text{V/s}$	$(-219.2 \pm 0.3)\mu\text{V/s}$	$(235.0 \pm 0.4)\mu\text{V/s}$
real value^b	$(214.4 \pm 0.4)\text{mV/s}$	$(-219.2 \pm 0.3)\text{mV/s}$	$(235.0 \pm 0.4)\text{mV/s}$

^a(first half -second half)/2

^b1000 times the averaged dV/dt

of dV/dt from the HV system.

For further improvement of the drift distortion, reduction of the transient ramp at field reversals has also been attempted using a reference signal in a square waveform with a rising and falling time of ~ 60 ms generated by the Agilent 33220A function generator. This reduction is also advantageous to minimize the transient current so that the SQUID sensor is stable. In contrast to the preceding performance tests, the 10 V_{pp} reference signal with 1.43 Hz is applied to the feedback circuit because the EDM experiment requires the application of the full range of 10 kV_{pp} across the GGG sample for enhancement of the EDM sensitivity. The real dV/dt of the Ch1 HV output is measured to be $(-0.05 \pm 0.03)\text{ V/s}$ while that of the reference signal is measured to be $(0.05 \pm 0.02)\text{ V/s}$. The result indicates that the drift performance is improved more than when using the pure square waveform. Compared with the expected drift value on the 10 kV_{pp} HV output from the Brandenburg 2540-301, the improved voltage drift is about 700 times smaller. This achievement is by virtue of the better reference voltage signal.

5.2.4 Conclusion

A new low-distortion HV polarity switch system has been built using vacuum-tube triodes as a HV switch. The HV system has been improved to have distortion below 10 ppm/s of voltage drift, leading to suppression of the non-zero spurious EDM signal. The reduction was achieved by improving the feedback circuit and reducing the transient ramp at field reversals. Currently, the voltage drift of the drive signal limits the performance of the HV system, hence it is necessary to find or develop a better function generator that has a smaller voltage drift for a future EDM experiment.

5.3 Improvement of the Statistical Sensitivity

5.3.1 Stable Operation of the SQUID Sensor

The EDM experiment operated at a temperature of 4.2 K results in sufficient suppression of intrinsic Johnson noise, which leads to stable operation of the SQUID sensor. For further increased stability of the SQUID sensor at the base level, any uncontrolled external noise sources of electromagnetic interference (EMI) or radio frequency interference (RFI) are undesirable. EMI/RFI increases the SQUID noise level (white noise as well as low frequency $1/f$ noise), triggers frequent SQUID baseline jumps, and makes it difficult to operate the SQUID sensor in the flux-lock loop. Moreover, the EMI/RFI can heat the SQUID components locally and change the voltage-to-flux transfer function on the SQUID readout electronics. Considerable effort including extensive laboratory work went into studying and eliminating electrical EMI/RFI noise as well as eliminating ground loops. Careful drawing of the ground paths in the electronic circuits of the whole system and connecting every zero reference point to the same ground point strongly reduces the possibility of unwanted current flowing in the ground loops. All electronics, e.g., a cell phone, not directly related to the experiment were turned off during the EDM measurement while electronics used for the experiment are powered through an isolation transformer to eliminate possible AC power line noise or noise transferred from the cyclotron facility at Indiana University. These nontrivial tasks provide significant improvements that help to stabilize SQUID operation at the base level without frequent SQUID baseline jumps.

The computer interface for the SQUID sensor (STAR Cryoelectronics PCI-1000) used in the EDM experiment connects the DAQ computer with a programmable feedback loop (STAR Cryoelectronics PFL-100). Typical computers are fairly noisy since all oscillators included in computer components, e.g., a motherboard or a video card, generate RF energy which can have negative impact on SQUID operation. Hence, a fiber optic modem (B&B electronics Model FOSTC), designed to provide connec-

tions between serial equipments (i.e., the DAQ computer and PCI-1000) using fiber optic cables, is employed. The use of fiber optic cables not only prevents the RF noise generated by the computer from leaking into the SQUID sensor, but also eliminates ground loop pickup. The PCI-1000 and the fiber optic modem are powered by clean 12 VDC car batteries in order to eliminate any power line frequencies and also the switching regulator RF interference used in most of the modern power supplies. A shielded serial cable (DB-9) between the PCI-1000 and the PFL-100 is used. Moreover, it was beneficial to locate the DAQ computer away from the SQUID equipments and to power the DAQ computer with a separate power outlet not shared by the SQUID electronics. Both the SQUID equipments and the remaining electronics such as HV supplies and DAQ system are mounted separately on two different racks to avoid possible noise pickup on the SQUID sensor.

To further suppress the flow of RF currents picked up by SHV (Safe High Voltage) cables, ferrite ring chokes (EMI filters) are added to both ends of the HV cables outside the cryostat. The chokes allow wanted signals (equal but in anti-phase) to pass through, while unwanted signals (in phase) are suppressed. In addition to the chokes, 1 M Ω and 200 k Ω (cryogenic-compatible) resistors serving as low pass filters are installed on the HV lines in series outside and inside the cryostat. With these resistors, it was confirmed that the high frequency ripple (~ 20 kHz) on the HV lines originating from the filament drive for vacuum tubes in the HV polarity switch system is eliminated and unseen by the SQUID sensor.

Since the experiment is operated at cryogenic temperatures, all cables and electronic components inside the cryostat should be cryogenic compatible. As an example, Fig. 5.22(a) shows a HV cable which is incompatible with cryogenic temperatures. After several thermal cycles down to 4.2 K, the insulation developed cracks. This damage undermines the voltage rating of the cable and frequent HV discharges can occur. This poses a serious problem since current induced by HV breakdown would exceed the current limit of the Josephson junctions of the SQUID and destroy the

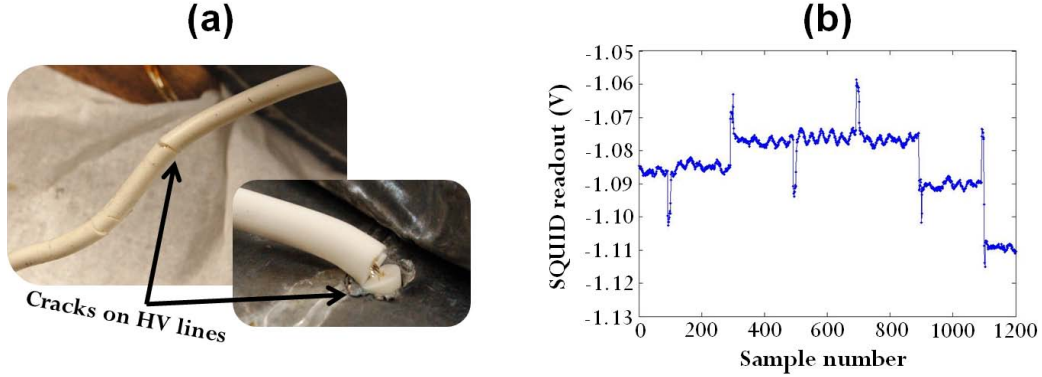


Figure 5.22: Source of SQUID baseline jumps. (a) Cryogenic-incompatible HV cables. Many cracks on the cables are observed after several thermal cycles of the system. (b) SQUID baseline jumps at every field reversal.

SQUID sensor. Additionally, the excess current could drive the superconductor in the SQUID sensor over its critical field, causing flux to become trapped and increasing the noise. HV discharge also gives rise to SQUID baseline jumps for every reversal of the field as shown in Fig. 5.22(b). To ensure the baseline jumps are real, the correlation between the SQUID readout and HV monitor signals was examined. Fig. 5.23 shows some examples of SQUID readout including the baseline jumps with the corresponding leakage current and HV monitor signals. Each enlarged section on Fig. 5.23(a) and (b) shows that small HV sparks (HV discharge) induce currents which cause baseline jumps on the SQUID sensor.

At the beginning of the experiment we encountered frequent SQUID instabilities in the form of baseline jumps at applied electric fields higher than 3 kV/cm. To address that, many tests on cryogenic-compatible HV cables and resistors were done. Incompatible HV components were replaced with cryogenic-compatible components which allowed the application of the full range of 10 kV_{pp} across the sample/electrode assembly.

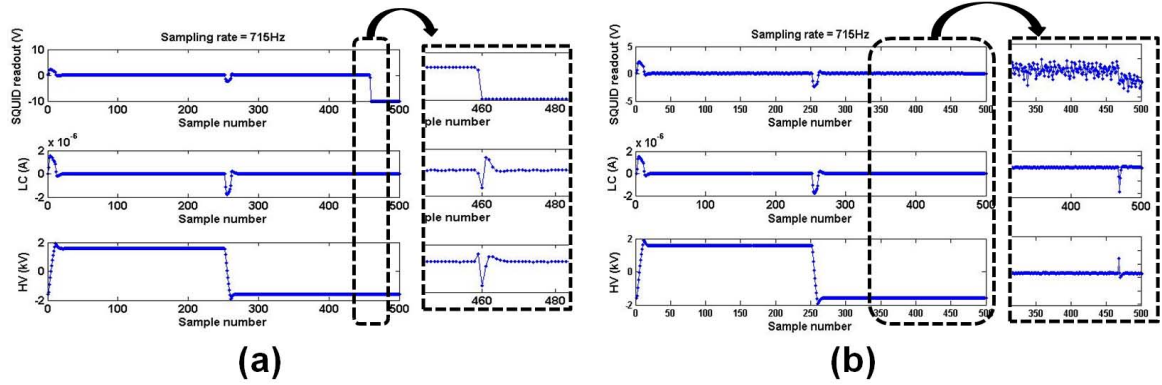


Figure 5.23: Examples of the SQUID baseline jumps due to HV discharge. (a) and (b) confirm that the HV discharge is a direct cause of SQUID instabilities.

5.3.2 Magnetic Shielding Improvement

The most important experimental requirement for higher SQUID sensitivity is the quality of magnetic shielding. If the magnetic shielding is poor then portions of the ambient magnetic field will remain in the sample/electrode assembly. Vibrations in the environment and liquid helium boiling will, through Faraday's law, cause the flux pickup coil to detect the residual magnetic fields. That results in observable vibrational peaks in the magnetic noise spectrum of the SQUID sensor. One example is shown in Fig. 5.24. Fig. 5.24(a) displays the flux noise spectrum of the SQUID sensor with many vibrational peaks due to insufficient magnetic shielding. The averaged SQUID signal in the time domain over 17278 cycles is also shown in Fig. 5.24(b) in which the SQUID signal is distorted by vibrational signals. Given that the vibrational peaks generally appear in the region of low frequency (mostly below 50 Hz) and the EDM experiment is also operated at a low frequency, the vibration pickup arising from poor magnetic shielding would be one of systematic effects (see Sec. 6.2). In addition to the systematic effect, the insufficient magnetic shielding would increase the flux noise of the SQUID sensor. According to Fig. 5.24(a), the flux noise of the SQUID sensor at 3 Hz is estimated to be $17 \mu\Phi_0/\sqrt{\text{Hz}}$ which is much higher than the manu-

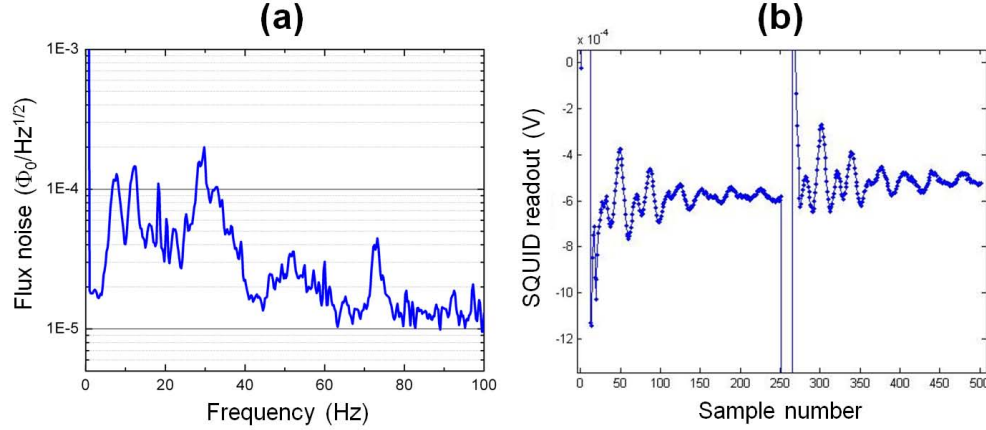


Figure 5.24: Insufficient magnetic shielding. (a) Many vibrational peaks are observable in the flux noise spectrum of the SQUID sensor. (b) The averaged SQUID signal in time domain over 17278 cycles shows evident vibrational signals.

facturer specification. Hence, the EDM experiment demands a high level of magnetic shielding to eliminate any residual fields (ambient and vibrationally-induced) around the assembly.

To reach the desired degree of magnetic shielding, first the sample/electrode assembly is shielded with two layers of superconducting lead foils as shown in Fig. 5.25. Fig. 5.25(a) shows the closed G10 cylinder housing the assembled package of electrodes and GGG samples. The G10 cylinder is enclosed by one layer of superconducting lead foil shown in Fig. 5.25(b). The lead foil is carefully sealed using solder. In order to ensure two layers of lead foil, a thin kapton insulator sheet is employed which separates one layer from the other as shown in Fig. 5.25(c). Finally, Fig. 5.25(d) displays the G10 cylinder enclosed by a second layer of superconducting lead foil. In this photograph, a solder-sealed lead box containing the SQUID sensor is also shown and each solder-sealed lead tube contains copper wires for control of the SQUID sensor, flux pickup coil, HV lines, and leakage current monitor wires. For further improvement of magnetic shielding, we employ an additional three layers of mu-metal and a cylinder

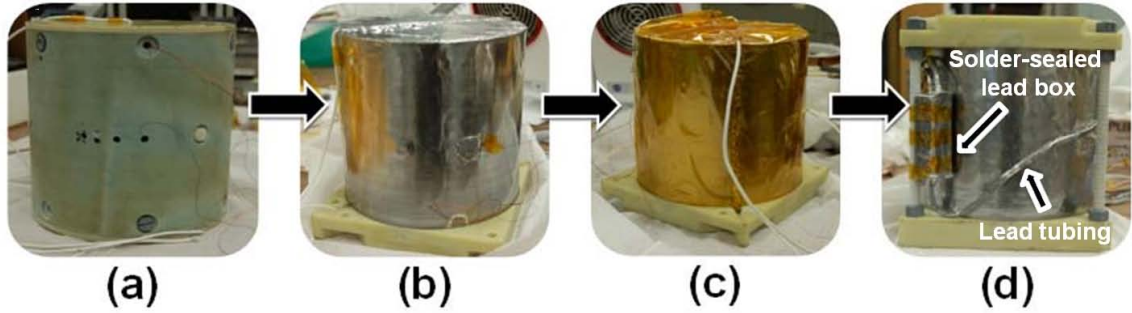


Figure 5.25: Photographs of two layers of superconducting magnetic shielding. (a) Assembled package of electrodes and GGG samples. (b) First layer of lead shield. (c) One layer of a kapton sheet insulator. (d) Second layer of lead shield.

of Co-Netic ferromagnetic shielding (see Sec. 4.1.1).

5.3.3 Conclusion

With the provisions mentioned above, the flux noise of the SQUID sensor is improved considerably. As displayed with the dashed curve in Fig. 5.26, the baseline of the SQUID sensor is measured to be $6\mu\Phi_0/\sqrt{\text{Hz}}$ at the frequency of operation (1.43 Hz) used in the EDM experiment (see next chapter). This sensitivity of the SQUID sensor is near to the manufacturer specification. To precisely estimate the overall magnetic shielding factor of the whole system, the following method is used: (a) an external uniform magnetic field with a frequency of 2 Hz and an amplitude of 10 Gauss, generated by a pair of Helmholtz coils wound outside the cryostat, is applied to the samples/electrodes assembly; (b) the amplitude of the residual peak at 2 Hz, detected by the flux pickup coil, is measured using a spectrum analyzer; and (c) the magnitude is compared to the applied field strength. The solid curve in Fig. 5.26 shows the spectrum with the application of the external magnetic field. With the suggested method, the overall magnetic shielding factor of the system is estimated to be 5×10^{11} , better than a factor of 50 improvement since the inception of

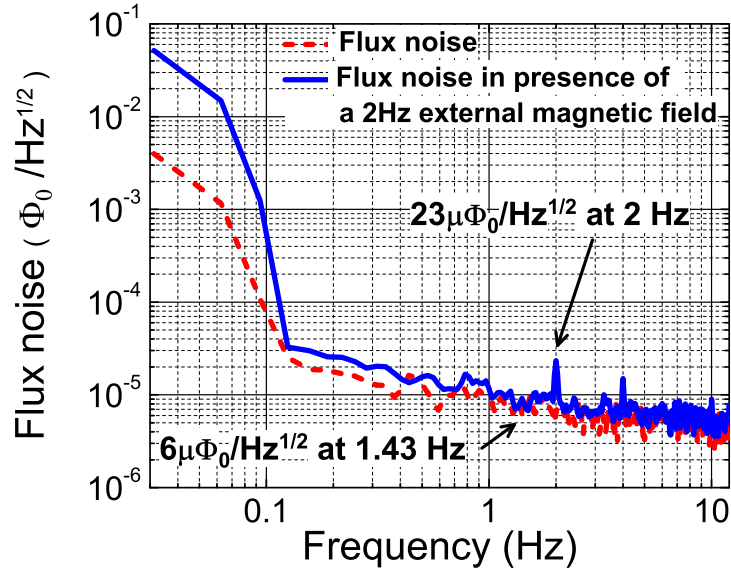


Figure 5.26: The magnetic flux noise spectra of the SQUID sensor operated at 4.2 K including the nominal noise spectrum (dashed curve) and the spectrum (solid curve) with an external magnetic applied field of 10 Gauss at 2 Hz.

the experiment. The quality of the magnetic shield and the ground-loop isolation also ensure that no observable vibrational peaks and power line harmonics show up on the SQUID flux noise spectrum. For more suppression of random noise, the average of the accumulated data sets is needed. The experimental results of the electron EDM experiment will be presented in the next chapter.

Chapter 6

Experiment Results

Through the efforts described above in the development and improvement stages of the experiment, which required the most time, the electron EDM experiment arrived at publishable results. In this chapter, the experimental measurements and results are discussed. In addition, possible systematic effects in this type of experiment are also covered.

6.1 Data Analysis

6.1.1 Experimental Method

The signal readout mechanism in the experiment has been improved considerably since the inception of the experiment using the 24-bit DAQ system. Fig. 6.1 displays the overall schematic of the improved signal readout mechanism. Each analog voltage signal is digitized by dedicated ADC boards, and the digital signals from each board used in the measurement are simultaneously collected by the FPGA on the master board through fiber-optic couplings. The signals are then transferred to the computer via Ethernet communication using MATLAB software. Each ADC board is housed in a separate metal enclosure and keeps apart from other enclosures to eliminate possible capacitive couplings. Data can be continually accumulated for a long time

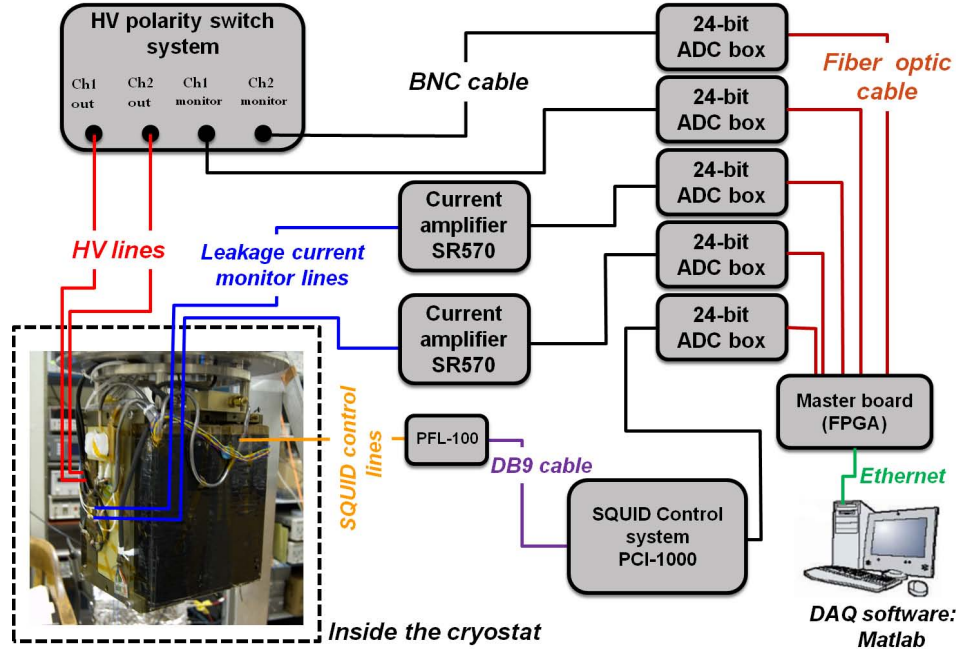


Figure 6.1: Schematic of the improved signal readout mechanism in the EDM experiment.

with the MATLAB language for data averaging, however the accumulation time for one uninterrupted run is limited by the need to replenish the liquid helium in the cryostat every 9 hours.

The voltage of the two HV electrodes was monitored using 1000:1 voltage dividers. Currents flowing in the two isolated ground electrodes were also monitored, as well as the analog voltage output from the SQUID readout electronics (PFL-100 and PCI-1000) that could be converted into the magnetic flux Φ_{sq} through the predetermined transfer function.

Fig. 6.2 shows a flowchart schematic of the DAQ software written in MATLAB for data control and data storage. The MATLAB script can be found in Appendix C. Before starting data storage, the HV drive source needs to be applied to the HV electrodes with the desired values (frequency, amplitude, and type of waveform) so as to warm up all electronics that provide voltage signals. The DAQ system values

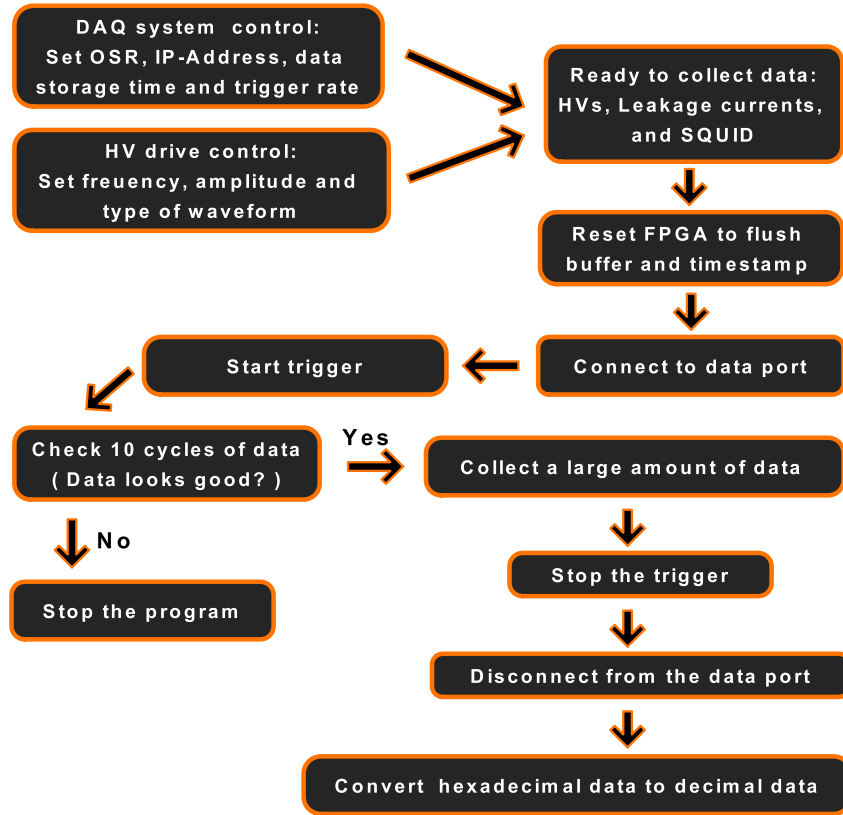


Figure 6.2: Flowchart to collect the voltage signals: HVs, Leakage currents and SQUID signal.

such as data storage time, OSR value, and trigger rate also need to be set. For data storage, the MATLAB program resets the FPGA first to flush buffers and timestamp and then establishes the connection to the data port (Xport). After the successful connection, it is ready to start the trigger to collect a large amount of data. To ensure that the collected data is not distorted by malfunctions of the DAQ system or the electronics, a step is added immediately before data collection during which the first 10 cycles of all voltage signals are plotted and can be checked by a person. In this step, if the collected data appears unacceptable, the MATLAB program will be aborted. After a desired amount of data is saved in a drive in the DAQ computer,

the program disconnects from the data port and stops the trigger. Because the raw collected data is expressed using hexadecimal, a step for conversion of hexadecimal data to decimal data is added as well.

In an EDM measurement sequence, a voltage of alternating polarity up to ~ 10 kV_{pp} in a square waveform with controlled ramp speed is applied to the HV electrodes. The ramp speed is limited to reduce the displacement current during field reversals, which helps to suppress any instability of the SQUID sensor. The polarity switching cycle is repeated at a rate of 1.43 Hz. This frequency of operation is chosen to be low enough to reduce the transient current, proportional to the frequency, but high enough to avoid the low frequency $1/f$ corner of the SQUID noise spectrum (see Fig. 5.26). In addition, the switching frequency is chosen to be irrational when 60 is divided by this frequency in order to cancel noise pickup at 60 Hz and its harmonics, which might occur during the measurement, in the process of data averaging. The SQUID sensor is heated up before starting a new run to diminish possible noise from trapped flux in the SQUID. The EDM measurement is not started until at least 30 minutes after replenishing the liquid helium so that the system has sufficient time to equilibrate in pressure and temperature.

Data analyses, including data averaging, are performed using MATLAB software. Data analyses, including data averaging, are performed using MATLAB software. In particular, a program was developed using MATLAB which is capable of scanning the data sequence of the SQUID readout during each uninterrupted run and then discarding any data cycles distorted by instabilities of the SQUID, such as flux jumps or EMI/RFI. The program allows only the undistorted data cycles to be used for data averaging.

Typical time-traces of data averaged for three hours on the monitored channels are plotted in Fig. 6.3. Data were taken with a sampling rate of 715 Hz (500 samples in one cycle) at OSR= 256. In this option, the cutoff frequency of the DAQ system is 357 Hz. The time-trace of the current monitor contains both the displacement current

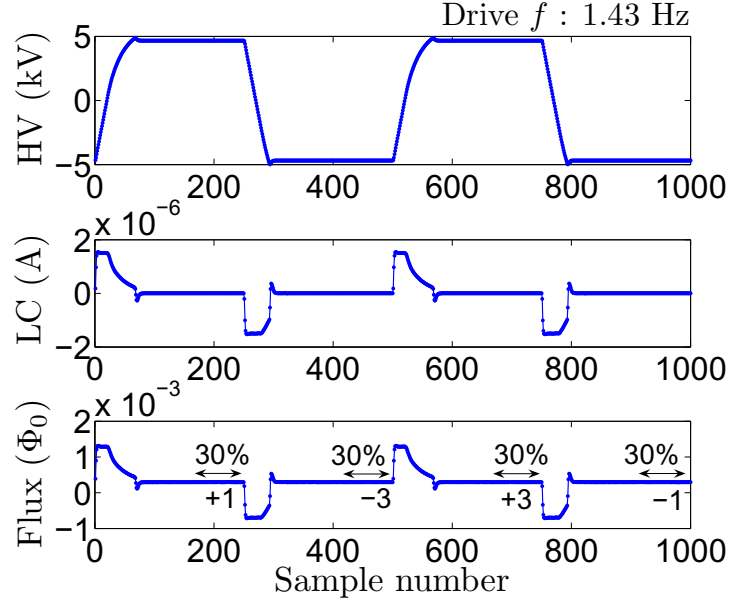


Figure 6.3: Time-traces of averaged signals for three hours on one HV monitor, one leakage current monitor, and the SQUID readout presented as two cycles of field reversal. Data were taken using the 24-bit DAQ system, with a sampling rate 715 Hz.

(charging and discharging current), CdV/dt , and the leakage current, V/R , flowing through the bulk sample or the sample surface. As shown in Fig. 6.3, the measured current through the ground electrode are dominated by the charging/discharging transient currents during the HV polarity switching. The SQUID sensor measures magnetic fields generated by the EDM-induced sample magnetization as well as by the electric currents flowing in and out of the electrodes as sources of systematic effects. During field reversals, the SQUID sensor measures the large magnetic field associated with the transient currents, which have to dissipate quickly so that the SQUID sensor can measure the EDM-induced magnetic flux once the field settles to the maximum amplitude of the applied HV. The difference between the flux when the HV is positive and negative within one cycle is proportional to the electron EDM and is the relevant

observable. The transient region immediately after each field reversal is excluded to attain the EDM-induced sample magnetization under each HV polarity. The HV output asymmetry on the HV monitor is observable, which might result from tiny functional problems of the HV components responsible for the positive HV output such as the vacuum tube or supporting components. The asymmetry, however, does not affect the electron EDM calculation because the region around the HV polarity switching is excluded. Our next-generation of HV polarity switch system will deal with this problem more carefully.

6.1.2 EDM Extraction Algorithms

Despite all the improvements discussed in the preceding chapter, there still exist residual voltage drifts on the SQUID readout. The worst case of such a voltage drift is illustrated in Fig. 6.5, and will be discussed later. The DC voltage drift can come from many sources including the SQUID electronics, the slow decrease in the level of the liquid helium, and the pressure drift inside the cryostat to name a few. Unlike the drift in the HV source, which changes sign in phase with the HV polarity, this DC drift does not have the same correlation with the HV cycle. To remove this DC drift from the data, we use two independent algorithms, drift-correction and fitting, to analyze the electron EDM data.

I Drift-Correction Algorithm

To obtain the electron EDM observable, the drift-correction algorithm takes the algebraic sum of the SQUID readout in two adjacent cycles of field reversal and applies a $[+1 -3 +3 -1]$ weighting to the averaged data for each half cycle. With this weighting, the effect of the DC voltage drift can be expanded into a polynomial function of the time and will cancel up to second-order. This can be verified as follows: let the voltage model of the averaged data be $V(t) = At + Bt^2 + Ct^3 + d$ where the first three terms are the voltage drift and the last term is related to the EDM-induced

magnetization. Then the weighting calculation on the averaged data for each half cycle is written as

$$\begin{aligned}
\Delta V &= V\left(\frac{T}{2}\right) - 3V(T) + 3V\left(\frac{3T}{2}\right) - V(2T) \\
&= \left(\frac{T}{2}A + \frac{T^2}{4}B + \frac{T^3}{8}C + d\right) + \left(-3TA - 3T^2B - 3T^3C + 3d\right) \\
&\quad + \left(\frac{9T}{2}A + \frac{27T^2}{4}B + \frac{81T^3}{8}C + 3d\right) + (-2TA - 4T^2B - 8T^3C + d) \\
&= -0.875CT^3 + 8d
\end{aligned}$$

where T is the period of the field reversal cycle and the EDM signal d changes sign when the electric field reverses the Stark-induced magnetization. Consequently, voltage drifts up to second-order are effectively eliminated. Although the third-order voltage drift remains in the weighting calculation, it should be negligible since the DC voltage drift is mostly first-order (i.e., $C \approx 0$). Note that to obtain the electron EDM observable, the resulting value ΔV should be divided by a factor of 8.

In this algorithm, the transient regions at the field reversal are excluded in the data average. Furthermore, to ensure that the transient current has sufficiently decayed, the data window contains only the last 30 % of the half cycle (see Fig. 6.3). The voltage drift dV/dt of the HV polarity switch system therefore needs to be controlled during the last 30 % of the half cycle so as not to dominate over the magnetic flux generated by the EDM-induced magnetization. Fig. 6.4 shows a histogram of the electron EDM observable, collected over one typical uninterrupted run with three hours of data. The distribution can be fitted to the Gaussian distribution, giving $\Phi_{sq} = (-1.89 \pm 9.25) \times 10^{-8} \Phi_0$. This corresponds to an electron EDM measurement of $d_e = (-0.24 \pm 1.17) \times 10^{-23}$ e-cm, using Eq. 4.14 and Eq. 4.15 which take into account all the suppression factors discussed in chapter 4.

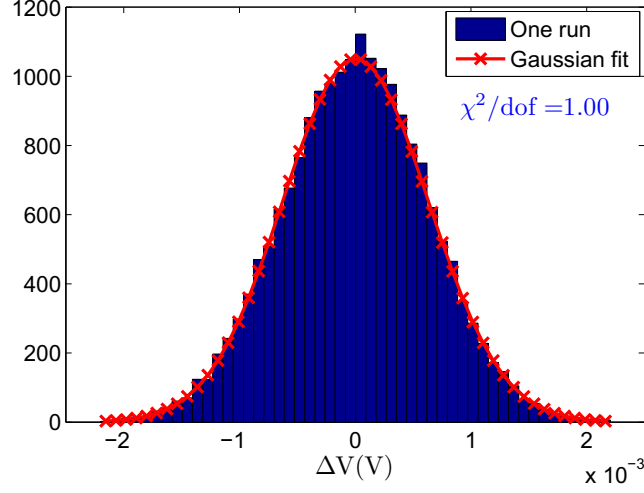


Figure 6.4: Distribution of the electron EDM observable (processed with the drift-correction algorithm). Data points were collected over one uninterrupted run (3 hours).

II Fitting Algorithm

To obtain the electron EDM observable, the fitting algorithm attempts to fit the entire time trace of the SQUID readout modulo one cycle of field reversal. Data from repeated, uninterrupted cycles over three hours are averaged to form the overall time-trace (Fig. 6.5). The error bars of each data point are estimated by the residual standard deviation from a least-square line fit on the last 30 % region of each half cycle. The averaged time-trace is fitted using the following voltage model:

$$\begin{aligned} V^+ &= Ae^{-t/\tau} + Bt + d^+ \\ V^- &= -A'e^{-t/\tau'} + (Bt + B\frac{T}{2}) + d^- \end{aligned} \tag{6.1}$$

where $V^+(t)$ or $V^-(t)$ are the SQUID readout during the half cycle with a positive and a negative HV polarity, respectively, and T is the period of the field reversal cycle. The first term in the model characterizes the decay of the transient current with a time constant τ and τ' . These two time constants could be different because of the asymmetry of the circuit handling the positive and negative voltage, the difference

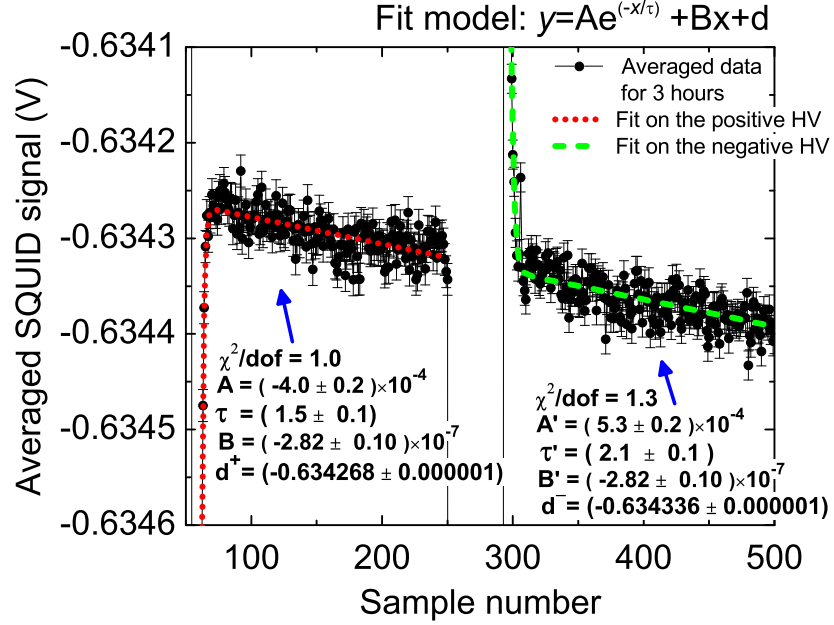


Figure 6.5: SQUID readout (averaged over one non-interrupted run) folded modulo one cycle of field reversal. This data set illustrates the worst case of DC voltage drift.

between the two HV channels, and/or the two HV electrodes. The second term describes the DC voltage drift. It is Bt for the first half cycle, and $Bt + B(T/2)$ for the second half a cycle, which starts $(T/2)$ later. The last constant term represents the EDM-induced magnetization and a DC offset. Note that the sign of the EDM-induced magnetization changes as the electric field is reversed, while the DC offset remains constant.

The electron EDM observable is derived by taking the difference of the fitted parameters d^+ and d^- (in which the DC offset is canceled out),

$$\Delta V = d^+ - d^- . \quad (6.2)$$

Note that in order to obtain the electron EDM observable, the resulting value ΔV should be divided by a factor of 2. The fit to the voltage model is performed using OriginPro software and the fitting results are shown in Fig. 6.5. The fitting algorithm

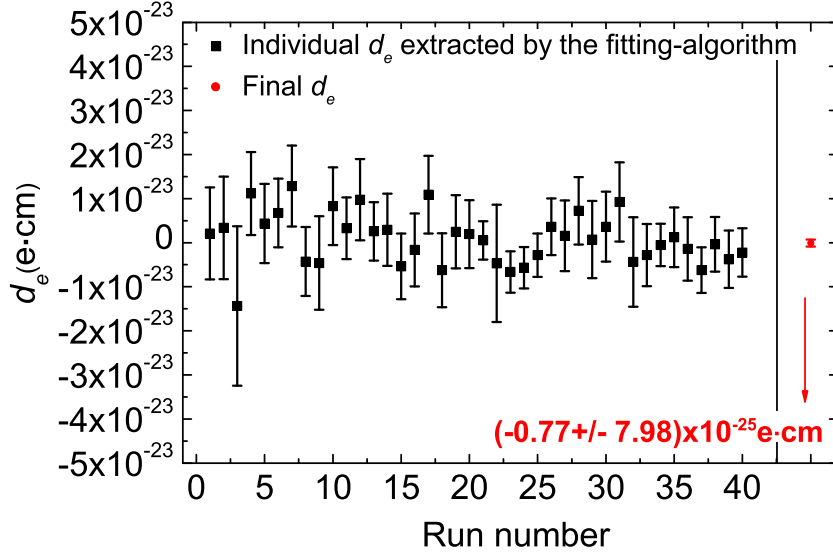


Figure 6.6: Results of electron EDM measurements, processed using the fitting algorithm. Each data point is the averaged result of one run. The final data point is the final averaged result over 40 experimental runs.

gives $\Phi_{sq} = (3.07 \pm 6.34) \times 10^{-8} \Phi_0$, corresponding to a d_e of $(0.39 \pm 0.81) \times 10^{-23} \text{ e.cm}$ using Eq. 4.14 and Eq. 4.15. The fitting algorithm arrives at a better statistical sensitivity than the drift-correction algorithm because the fitting algorithm uses the last 75 % of the time trace as opposed to 30 % used in the drift-correction algorithm. To increase the experimental sensitivity, data was collected over two weeks with a total integration time of 120 hours.

6.1.3 Error-Weighting for Data Averaging

Data analysis using the two algorithms shows similar distributions of the extracted electron EDM from each uninterrupted run. The results using the fitting-algorithm are shown in Fig. 6.6. Each data point corresponds to an uninterrupted run lasting for three to four hours. Proper error-weighting is applied to average the results of

each run from the drift-correction algorithm and the fitting algorithm. In the error-weighting, data points with higher sensitivity contribute more to the weighted mean \bar{d}_w which corresponds to the central value of the final electron EDM d_e . The weighted mean is given by

$$\bar{d}_w = \frac{\sum_{i=1}^N \frac{d_i}{\sigma_i^2}}{\sum_{i=1}^N \frac{1}{\sigma_i^2}} \quad (6.3)$$

where $1/\sigma_i^2$ is selected for the weighting, and in which σ_i is the sensitivity and N is the total number of uninterrupted runs. The weighted standard deviation σ is given by

$$\sigma = \sqrt{\frac{\sum_{i=1}^N \frac{1}{\sigma_i^2} (d_i - \bar{d}_w)^2}{\sum_{i=1}^N \frac{1}{\sigma_i^2}}} \times \sqrt{\frac{N}{N-1}}. \quad (6.4)$$

Finally, the weighted statistical error, corresponding to the final experimental sensitivity, is given by σ/\sqrt{N} . Note that the results with this error-weighting are the same as with the least-square constant fit. With this error-weighting, the final electron EDM value with 120 hours of data averaging is estimated to be $(0.41 \pm 1.38) \times 10^{-24}$ e·cm and $(-0.77 \pm 7.98) \times 10^{-25}$ e·cm for the drift-correction and fitting algorithms, respectively. These results can be compared to the previous experimental limit of $|d_e| < 5 \times 10^{-24}$ e·cm using a similar solid-state method in the gadolinium iron garnet system [30].

6.2 Discussion

In addition to the EDM sensitivity estimated in the preceding section, careful investigation of systematic effects of the GGG-based EDM search are also necessary. In this section, several sources of systematics are presented and the spurious magnetic flux generated by each effect is compared because the measured physical observable

is the magnetic flux. The present measured magnetic flux averaged over all runs is estimated to be $\Phi_{sq} = (0.48 \pm 6.02) \times 10^{-9} \Phi_0$.

6.2.1 Systematic Effects

The dominant systematic effect is due to the current flowing through the GGG sample which produces a magnetic field in phase with the polarity of the applied HV by the well-known Maxwell's equation inside a material:

$$\nabla \times \mathbf{H} = \mathbf{J}_f + \epsilon \partial \mathbf{E} / \partial t .$$

The first term on the right side is the leakage current due to the finite resistivity of the sample and the second term represents the displacement currents. It should be noted that, to first order, the magnetic fields generated by these currents are perpendicular to the EDM-induced magnetization. Some fraction of the field, however, will be measured by the SQUID sensor due to an inevitable slight tilt of the pickup coil. Studies of the correlation between the currents, the time-derivatives of the applied HV, and the SQUID signal allow us to quantify how much the radial fields generated by the currents could leak into the pickup coil and contribute to a spurious EDM signal. In particular, in the region of field switching the SQUID sensor detects an enormous magnetic field generated by the displacement current as shown in Fig. 6.3. The correlation studies also make it possible to separate the contribution from the displacement current from that of the leakage current. The current at the time of field reversal was measured to be $1.5 \mu\text{A}$, and the expected magnetic flux seen by the SQUID would be $1.4 \times 10^{-12} \text{ T}\cdot\text{cm}^2$ taking into account the coupling efficiency β described in Sec. 4.2. The actual magnetic flux measured by the SQUID sensor at the same region was $2.0 \times 10^{-14} \text{ T}\cdot\text{cm}^2$. Comparing the two flux values suggests that the pickup coil encloses about 1.4 % of the radial field generated by the current. An improvement to the geometry-dependent factor of 1.4 % will be attempted in a next generation EDM experiment by improving the alignment of the sample/electrode

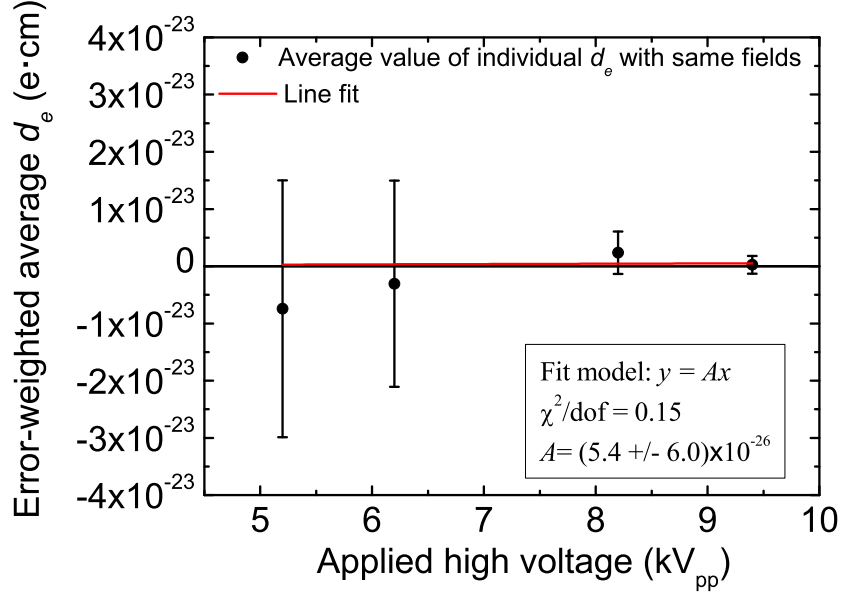


Figure 6.7: Measured electron EDM as a function of the applied HV. The data point at 9.4 kV_{pp} contains the highest statistics.

assembly.

With this estimate, for example, a current of (6 ± 2) pA (averaged over three hours in one uninterrupted run) measured excluding field transient regions at the maximum applied voltage of 9.4 kV_{pp} generates a spurious magnetic flux Φ_{sq} of $(3.79 \pm 1.26) \times 10^{-9} \Phi_0$ that is lower than the present flux sensitivity $6.02 \times 10^{-9} \Phi_0$. Despite the finite leakage current, the measured electron EDM is shown to be independent of the strength of the applied electric fields within the error bars, as shown in Fig. 6.7. In this figure, most measurements were made at 9.4 kV_{pp}. The fit model ($y = Ax$) was chosen such that no electron EDM would be present in the absence of applied fields and also to include a linear field dependence of a spurious electron EDM as shown in Fig. 5.15. This result suggests that the GGG-based EDM experiment is free of systematic effects linear in the HV.

More worrisome are surface currents following a helical path which generate an

additional magnetic flux. The magnetic flux in this case is parallel to the EDM-induced magnetization and so is directly picked up by the SQUID sensor. As an example, assuming a leakage current of 6 pA flows on the sample surface in a quarter-turn, the corresponding spurious magnetic flux generated by the current is calculated to be $2.3 \times 10^{-15} \text{ T}\cdot\text{cm}^2$. The SQUID sensor would measure the spurious flux to be $8.6 \times 10^{-5} \Phi_0$ which is about 140 times the present flux sensitivity. As a result, this surface current can generate large systematics for this type of experiment. No spurious electron EDM, however, is measured at the present sensitivity level, which indicates that such a detrimental current is not present or the spurious magnetic flux due to the current is too small to detect at the present sensitivity level. Higher experimental sensitivity is necessary to further investigate this current effect.

Another important source of systematics is cross-talk between the SQUID and other voltage monitor channels in the DAQ system. Large voltage changes such as that on the HV monitor channels can induce some degree of signal distortion in the SQUID monitor channel through capacitive coupling. The channel cross-talk of the 24-bit DAQ system has been characterized in Sec. 5.1. A square wave with an amplitude of 19 V_{pp} and a frequency of 1.5 Hz was applied to an aggressor channel and a victim channel collected samples for 8 hours. The averaged data over 41548 cycles is shown in Fig. 5.8(a). The difference in voltages between the first and second halves in the figure is computed using the region in the last 30 % of each half cycle, similar to the electron EDM observable presented in the preceding section. The calculation gives a voltage difference of $(1.30 \pm 3.76) \times 10^{-9} \text{ V}$ which is expected to be $\Phi_{sq} = (0.52 \pm 1.51) \times 10^{-10} \Phi_0$. This systematic is well below the present flux sensitivity. Consequently, the developed 24-bit DAQ system provides significant progress in suppressing one of the dominant systematic effects in this experiment. The channel cross-talk is currently estimated to be better than 191 dB in the DAQ system.

Magnetic hysteresis of the GGG sample is another source of systematic effect.

Since GGG is a paramagnet, magnetic hysteresis should not be a dominant systematic effect, but it is nonetheless possible. The main concern is a remnant sample magnetization caused by enormous magnetic fields generated by displacement currents during field switching. Note that the spurious sample magnetization changes sign as the electric field is reversed like the EDM-induced sample magnetization. For this reason, this systematic, if present, can be very detrimental. As described above, the magnetic field of the displacement current tends to be perpendicular to the EDM-induced magnetization, therefore 1.4 % of the remnant sample magnetization is picked up by the SQUID sensor. For example, a displacement current of $1.5 \mu\text{A}$ gives rise to a radial magnetic field of $1.71 \times 10^{-11} \text{ T}$, resulting in the remnant sample magnetization persisting after the displacement current dies down. Using the SQUID-based susceptometer system MPMS to characterize the magnetic hysteresis property of the GGG sample cannot produce measurements at the required sensitivity level due to large vibrations of the remnant field during each field ramping. Since there is no measurable offset between the half cycles on the SQUID readout, an upper limit can be placed on the remnant magnetization using the EDM results. Given the knowledge of the magnetic susceptibility of GGG, the remnant magnetization, which changes in phase with the applied field, needs to be controlled to better than $2.5 \times 10^5 \mu_B/\text{cm}^3$.

The final possible source of systematics we considered is vibrational peaks at the field reversal frequency of 1.43 Hz and harmonics thereof which can be observed on the flux noise spectrum of the SQUID sensor (see Fig. 5.24). Because the vibrational peaks are not suppressed during data averaging, they can distort the SQUID readout, resulting in a voltage offset between the half cycles in the SQUID readout. For example, assuming a vibrational sine wave at 1.43 Hz exists during the EDM measurements, the averaged SQUID readout will show the voltage offset as a spurious EDM signal due to the averaged sine wave. To estimate vibrational contributions to the spurious EDM signal, the flux noise spectrum of the SQUID sensor must be

Table 6.1: Systematic effects

Source	Φ_{sq}
Displacement current	$1.65 \times 10^{-10} \Phi_0^a$
Leakage current	$(3.18 \pm 0.07) \times 10^{-9} \Phi_0^b$
Channel cross-talk	$(0.52 \pm 1.51) \times 10^{-10} \Phi_0^c$
Present Flux Measurement	$(0.48 \pm 6.02) \times 10^{-9} \Phi_0^d$

^a $C \frac{dV}{dt} < 0.2$ pA at 9.4 kV_{pp}

^bAveraged over all runs

^cChannel isolation > 191 dB

^dAveraged over all runs

averaged over at least three hours and then fitted using

$$y = A + B/f + Ce^{-\frac{(f-1.43)^2}{2\sigma^2}}$$

where the first and second terms denote the white and pink noise respectively, and the last term characterizes a vibrational peak at 1.43 Hz. The amplitude C of the fit gives the numerical constraint on the possible vibrational contributions. Unfortunately, there was no opportunity to perform this study, and so it should be performed during the next-generation EDM measurements. Since there is no measurable offset between the half cycles on the SQUID readout, an upper limit can be placed on the vibrational peaks using the EDM results, just as in the case for magnetic hysteresis.

The comprehensive list of systematic effects is outlined in Table 6.1. At present, no spurious EDM signals are measurable; however, a next-generation electron EDM experiment, expected to improve the experimental sensitivity by several orders of magnitude (see Sec. 7.2), might suffer from a false EDM signal resulting from the leakage current. More careful studies are required to confirm if the EDM experiment is limited by the systematic of the leakage current in future measurements which will operate in the milli-Kelvin range.

6.2.2 Final Electron EDM Value

It appears that the dominant systematic effect comes from the leakage current, which creates an additional magnetic flux, and can lead to a spurious electron EDM signal through Eq. 4.14. The SQUID sensor measures not only the EDM-induced magnetization but also the spurious electron EDM signal which is mostly due to the leakage current. Accordingly, the measured magnetic flux Φ_{sq} needs to be corrected for each run by subtracting the corresponding additional magnetic flux created by the leakage current before extracting the electron EDM value. Since the fitting algorithm gives the higher statistical sensitivity than the drift-correction algorithm, only data extracted by the fitting algorithm are used for this correction. This consideration leads to the corrected central value of the electron EDM of -5.57×10^{-25} e·cm. With the spurious magnetic flux created by the leakage current, the total systematic uncertainty is also estimated to be $\pm 0.12 \times 10^{-25}$ e·cm using the proper error-weighting used in the estimate of the statistical uncertainty. These results lead to the final reported electron EDM value of $(-5.57 \pm 7.98_{\text{stat}} \pm 0.12_{\text{syst}}) \times 10^{-25}$ e·cm with 120 hours of data averaging, where the first uncertainty is statistical and the second systematic [80, 81]. With the background-free electron EDM value in this prototype experiment operating at 4.2 K, we have demonstrated the feasibility of the GGG-based solid state technique for the electron EDM search.

Chapter 7

Conclusions and Future Work

7.1 Conclusions of the EDM Experiment

In this dissertation we presented an experimental search for the intrinsic electron EDM using the non-conventional solid state technique at a low temperature. This research topic contributes considerably to a stringent test of fundamental discrete symmetries assumed in the SM of particle physics because the EDM observable emerges only if parity inversion and time reversal symmetries are both broken. In particular, it can open a way to provide crucial information about the nature of the less well-understood T violation at energy scales higher than tens of TeV, and could provide information complementary to results from high-energy collider experiments on the nature of symmetry breaking.

The experiment employs a gadolinium gallium garnet paramagnetic insulator which has a large magnetic response at low temperatures. A presence of the electron EDM would lead to a finite magnetization when the garnet sample is subjected to a strong electric field. The resulting Stark-induced magnetization is measured as the EDM signal using modern magnetometry in the form of the SQUID.

Significant efforts to control systematic effects and improve the statistical sensitivity are described. The major efforts include the design and implementation of the

24-bit DAQ system with ultra-low degrees of channel crosstalk, as well as a reduction of the voltage drift from the HV polarity switch system. Recent progress on the suppression of several sources of background allows the experiment to run free of spurious signals at the level of the statistical sensitivity. This dissertation reports the first background-free experimental limit of the electron EDM from the GGG-based EDM experiment on the order of 10^{-25} e·cm. This limit is the most sensitive result ever reached using the solid state method [30].

7.2 Further Improvements and Prospects

7.2.1 Low-Temperature EDM Experiment

Further improvement of the electron EDM sensitivity using the GGG system is possible. It would require cooling the experiment to milli-Kelvin temperatures using a dilution refrigerator. At such low temperatures, spin ordering in the GGG sample would increase according to the $1/T$ behavior of the magnetic susceptibility so that the EDM sensitivity is expected to be enhanced by about a factor of 100 at 40 mK, without improvements to other parts of the experiment. As mentioned in Chap. 4, however, the non-zero Curie-Weiss temperature and the spin-glass phase transition could potentially limit this gain. Careful measurements of the magnetic properties of the GGG material at low temperatures are required to determine the impact of its intrinsic AFM spin coupling. Preliminary measurements at such low temperatures are presented in Appendix A in detail.

The expected improvement in the electron EDM sensitivity originates from the enhanced magnetic susceptibility at sub-Kelvin temperatures, and so the same level of statistical uncertainty in the flux measurements as used in the 4.2 K experiment is sufficient. In addition, the constraints on all the systematic effects discussed in this dissertation do not need to be improved further. In fact, the leading systematic effect due to the leakage current can only be reduced by cooling the GGG sample to lower

temperatures at which the resistivity of the sample increases.

7.2.2 Design for the Next-Generation EDM Experiment

An improved experimental design for our next-generation EDM experiment can be made using additional studies with finite-element analysis calculations. As was described briefly in Chap. 4, optimized dimensions of lead shields containing the samples/electrodes assembly, as well as the position of the flux pickup coil, can enhance the EDM sensitivity. A change of the pickup coil placement can improve both the flux enhancement factor of the pickup coil and the flux suppression factor. Furthermore, changes to the sample's height are also an important factor to be investigated. Accordingly, studies about the effect of these changes in the present experimental setup on the EDM sensitivity have been accomplished. The studies suggest a best experimental configuration at the end.

I Change of the Placement of the Pickup Coil

To begin with, the effect of the flux pickup coil location on the EDM sensitivity is investigated by changing the gap size between the two GGG samples: a smaller gap size means that the pickup coil is closer to the GGG sample. With the present gap size of 0.66 cm already studied in Chap. 4, three different cases with the gap sizes of 0.46 cm, 0.25 cm, and 0.05 cm are additionally examined. Because the pickup coil location affects both the flux suppression factor (f) and the flux enhancement factor of the pickup coil ($1 + \eta$), those factors are estimated using a finite-element analysis calculation. Note that the gap size can be maximally reduced to the diameter of pickup coil (0.013 cm) if the ground electrodes are eliminated.

In the numerical calculations, each sample retains an identical remnant field of 1 Gauss along the z -axis like a permanent magnet as before. One example of the solutions is shown in Fig. 7.1(a) as a color-coded filled contour plot of B_z along the $y=0$ plane. The gap size in the figure was set to be 0.25 cm. Fig. 7.1(b) displays the line

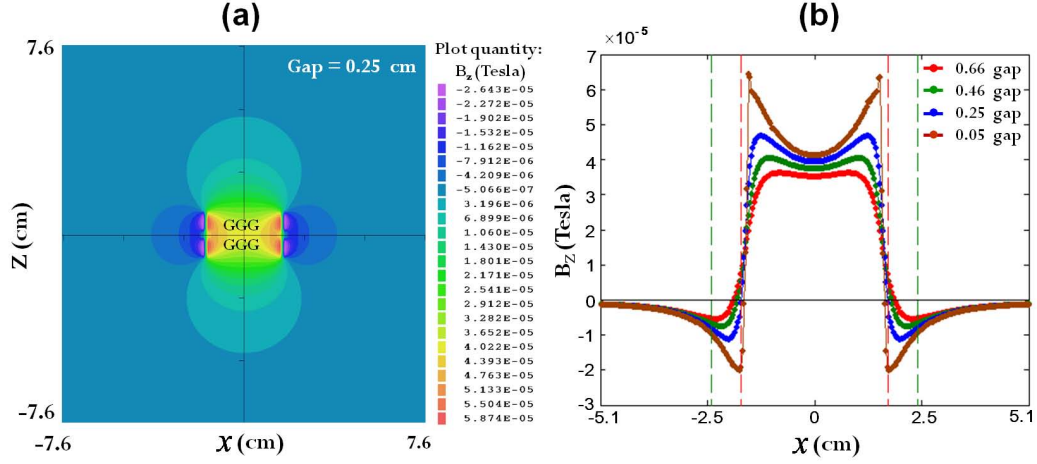


Figure 7.1: Solutions of the finite-element analysis calculation investigating the effect of the flux pickup coil location. (a) 2-D color-coded filled contour plot of B_z in Tesla along the $y = 0$ plane with the gap size of 0.25 cm. (b) Combination of line scans of B_z along $z=0$ where the pickup coil is placed on the solutions. Red and green dashed lines denote areas of the inner and outer coils of the pickup coil.

scans of B_z along $z=0$ performed for all cases. It can be seen that a smaller gap size provides a larger magnetic flux pickup as well as larger returning flux pickup, resulting in enhancement of the EDM sensitivity. In order to quantify the resulting total enhancement of the EDM sensitivity, the factors $1 + \eta$ and f has been estimated using the algorithms of Eq. 4.6, Eq. 4.7 and Eq. 4.8 (see Chap. 4). According to Eq. 4.9, the total sensitivity enhancement factor (e_{tot}) can be expressed by $e_{tot} = f(1 + \eta)$. A larger e_{tot} gives higher experimental sensitivity. The results are summarized in Table 7.1. As expected, smaller gap sizes provide larger total enhancement, leading to improvement of the experimental sensitivity. In comparison with the result from the present experimental setup, the new configuration with the gap size of 0.05 cm is estimated to push up the sensitivity a factor of 1.9. In other words, the experimental sensitivity is improved from 8.0×10^{-25} e·cm to 4.1×10^{-25} e·cm.

Table 7.1: Total enhancement of the EDM sensitivity from changing the gap size between two GGG samples.

gap size (cm)	f	$1 + \eta$	e_{tot}
0.66	0.16	1.1	0.17^a
0.46	0.18	1.2	0.21
0.25	0.21	1.2	0.26
0.05	0.25	1.3	0.33

^aThe present experimental setup

II Change of the Dimension of Lead Shields

The flux enhancement factor of the pickup coil, $1 + \eta$, is expected to be increased by reducing the radial dimension of the superconducting lead shields that separate the sample/electrode assembly from the ambient fields. Diminishing the radial dimension results in compressing the returning flux lines laterally, thereby more returning flux can be enclosed by the flux pickup coil. It is possible then to improve the present flux enhancement factor of 1.1.

In order to estimate the total sensitivity enhancement factor e_{tot} obtained from a change of the lead shield dimension, the radius of the shield was changed from 6.4 cm to 2.5 cm in the field simulations with the height fixed. It was found that the returning flux compression is not greatly influenced by the shield height. Note that the maximum reduction of the radial dimension is limited by the size of the pickup coil, i.e., the diameter of its outer coil of around 5.1 cm. The solutions of the field simulations are shown in Fig. 7.2. It can be seen that more returning flux is enclosed by the pickup coil at smaller shield diameters in Fig. 7.2(b). Unfortunately, however, the magnetic flux is shown to be suppressed more at smaller shield diameters, resulting in a loss of the EDM sensitivity.

The total sensitivity enhancement factor, given by $e_{tot} = f(1 + \eta)$, is indicated in Table 7.2. Despite more flux suppression, smaller radial dimension of the lead shield

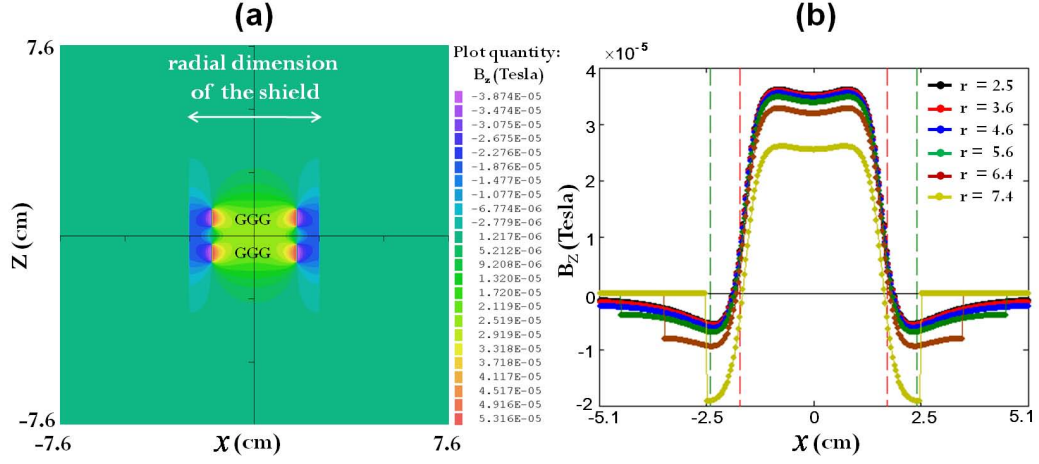


Figure 7.2: Solutions of the finite-element analysis calculation with the different radial dimension of the lead shields. (a) 2-D color-coded filled contour plot of B_z along the $y=0$ plane with the shield diameter of 5.1 cm. (b) Combination of each line scans of B_z along $z=0$ on the solutions. Red and green dashed lines denote areas of the inner and outer coils of the pickup coil.

can slightly improve the experimental EDM sensitivity. The EDM system enclosed by nearly maximally reduced lead shields is estimated to push up the EDM sensitivity

Table 7.2: Total enhancement of the EDM sensitivity from changing the dimensions of lead shields.

shield radius (cm)	f	$1 + \eta$	e_{tot}
2.5	0.10	1.9	0.19
3.6	0.14	1.3	0.18
4.6	0.15	1.2	0.17
5.6	0.15	1.1	0.17
6.4	0.16	1.1	0.17
7.4	0.16	1.1	0.17^a

^aThe present experimental setup

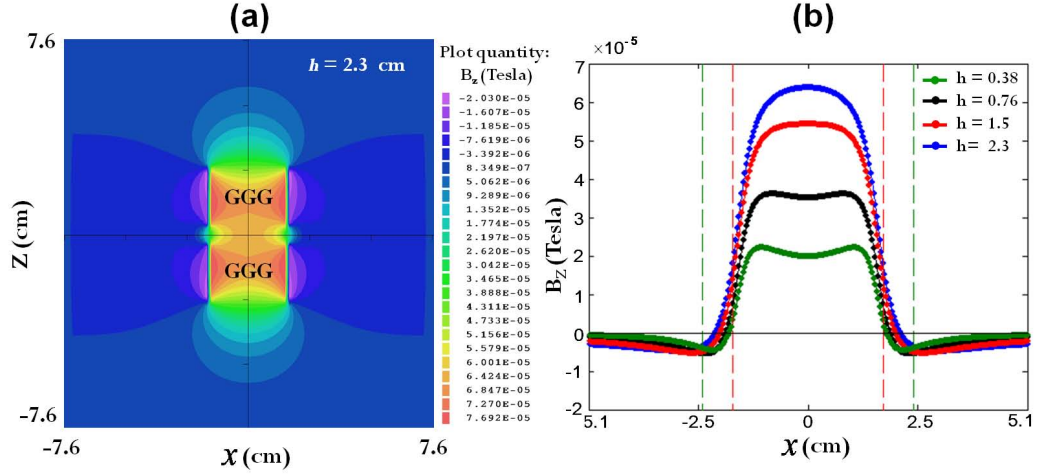


Figure 7.3: Solutions of the finite-element analysis calculation with the different sample height. (a) 2-D color-coded filled contour plot of B_z along the $y = 0$ plane with the sample height of 2.3 cm as an example. (b) Combination of each line scans of B_z along $z=0$ on the solutions. Red and green dashed lines denote areas of the inner and outer coils of the pickup coil.

by a factor of 1.1 compared to the present experimental setup.

III Change of the Sample Size

In addition to the changes described above in the present experimental setup for the sensitivity enhancement, a change of the sample size should also be studied to understand its effect on sensitivity. Since the diameter of the GGG sample is fixed to be equal to that of the pallet used in the synthesis of the polycrystalline GGG, only the sample height is of interest.

In the field simulations, the sample height h is set to be 0.38 cm, 1.5 cm, and 2.3 cm beyond the present height of 0.76 cm with the sample diameter fixed at 3.3 cm. One of the solutions is shown in Fig. 7.3(a) with $h = 2.3$ cm. Fig. 7.3(b) displays all line scans of B_z along the line of $z=0$ performed using each solution. According to the figure, the flux suppression is significantly reduced with larger sample height, leading

Table 7.3: Total enhancement of the EDM sensitivity from the change of the sample height.

h (cm)	f	$1 + \eta$	e_{tot}	e_{tot} / h
0.38	0.10	1.18	0.12	0.79
0.76	0.16	1.10	0.18	0.59^a
1.5	0.22	1.00	0.22	0.37
2.3	0.26	0.95	0.25	0.27

^aThe present experimental setup

to a larger flux pickup. Less of the returning flux, however, is then enclosed by the pickup coil.

It should be noted that the strength of the applied electric field across the GGG sample is also changed depending on the sample height: $E_{ext} \propto 1/h$. Therefore, in this case the total sensitivity enhancement factor, e_{tot} , should take into account the sample height by $e_{tot} = [f(1 + \eta)]/h$. The results are shown in Table 7.3. Due to the main $1/h$ behavior of the total sensitivity enhancement factor, the higher sample height decreases the EDM sensitivity despite the improvement in f . Therefore, the height of the GGG sample should remain as small as possible in the next-generation, provided it is not so small that electrical breakdown can occur. Cutting the sample in half laterally leads to a sensitivity enhancement by a factor of 1.3 in comparison with the present experimental setup.

IV Summary

In summary, based on the studies above, a better design for the next-generation EDM experiment is proposed as follows: (1) the two GGG samples used in the experiment are separated with a gap size of 0.051 cm, (2) the diameter of the lead shields is reduced to 5.1 cm. The total sensitivity enhancement of the proposed experimental setup has been additionally investigated using field simulation software. The factor

$1 + \eta$ and f obtained from this configuration are estimated to be 1.92 and 0.20, respectively. As a result, the proposed experimental setup enhances the experimental EDM sensitivity by a factor of 2.2 compared with the present experimental setup without any improvements to other parts of the experiment.

Since the EDM sensitivity increases at smaller gap sizes between the two GGG samples, the best configuration would eliminate the ground electrodes, the two samples stick together, and the flux pickup coil is located in the center of the combined sample. The meaning of that samples stick together is simply to use one GGG sample with a height twice that of the present samples. Measuring the leakage current and mounting the pickup coil remains to be resolved. The uniformity of applied electric field in the new configuration also needs to be investigated.

7.2.3 High Voltage System Improvements

At present, the voltage drift from the HV polarity switch system is limited by the drift of the drive signal generated by the arbitrary function generator. Development of a better drive source with higher resolution is required for further suppression of the voltage drift beyond the present value of 10 ppm/s. Improvement of drift characteristic will diminish the dominant systematic effect of the displacement current. For this reason, a precision 20-bit DAC board has been designed to be added to the 24-bit DAQ system. The DAC board can be used to drive the HV polarity switch system in a future electron EDM experiment.

The simplified schematic of the recently-built precision DAC board is shown in Fig. 7.4. The DAC board is controlled by the master board of the 24-bit DAQ system in the same way as the ADC board (see Sec. 5.1). The serial optical interface with the master board is implemented with the same optical modules (TORX147 and TOTX147) and optical fibers as the ADC board. The same PLL as the ADC board is used to recover the sample clock signal. The DAC function is accomplished with a 20-bit Analog Devices DAC chip (AD5791) and supporting components with

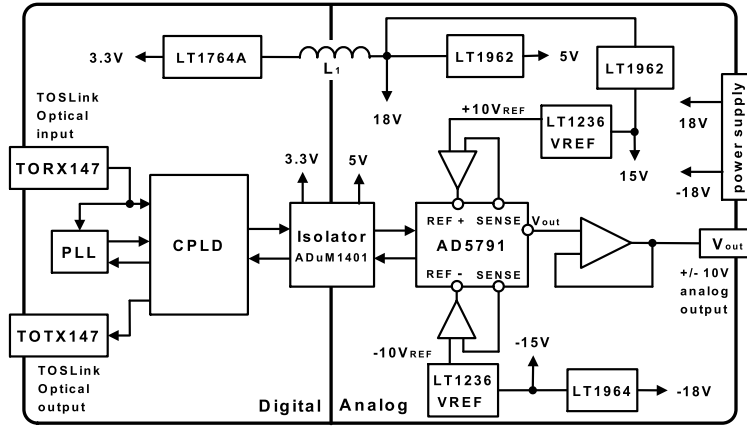


Figure 7.4: Simplified schematic diagram of the precision DAC board.

low noise and low temperature drift. The DAC chip offers a total harmonic distortion of <-97 dB, a low noise of $7.5 \text{ nV}/\sqrt{\text{Hz}}$, and a low temperature drift of $<0.05 \text{ ppm}/^\circ\text{C}$ [82]. This DAC chip is connected in a force sense reference configuration that uses the low-noise op-amp (AD8675) for the reference buffer and the ultra-low drift voltage references (LT1236) to apply a very stable $\pm 10 \text{ V}$ voltage reference, in order to minimize errors caused by varying reference currents. This reference circuit is very important as the DAC output is derived from the voltage reference inputs. The force sense reference buffers are required to accurately sense and compensate a voltage drop on the reference inputs. This reference configuration provides the best linearity performance of the DAC chip. The DAC output is buffered using another AD8675 op-amp in a unity gain configuration. Because the output impedance of the DAC chip is $3.4 \text{ k}\Omega$, the output buffer is required for driving low resistive loads. The analog power (LT1962 and LT1964) and digital power (LT1764A) are isolated using the digital isolator (ADuM1401) which, along with inductor L_1 , prevent digital noise from spreading to the analog supply. This DAC board is operated by a $\pm 18 \text{ V}$ DC power supply. The analog output waveform from this custom DAC board is created by the DAQ computer and the output range is $\pm 10 \text{ V}$.

Performance of this custom DAC board needs to be evaluated. The important performance characteristics to be scrutinized are the intrinsic rms noise and the voltage drift dV/dt on its analog output. The performance characterizations are measured using the 24-bit DAQ system. The rms noise is measured to be $<12 \mu V$ which is sufficient for driving the HV polarity switch system. In the voltage drift evaluation, the DAC board generates a square waveform with adjusted ramp speed, the same as what is used in the EDM experiment, with frequency 1.43 Hz and amplitude $10 V_{pp}$. Then the analog square waveform output is connected to the analog input of the 24-bit ADC board. Data are collected for 4 hours in order to perform data averaging. The voltage drift from the output is estimated to be ~ 0.03 ppm/s and ~ 0.3 ppm/s using the last 30 % and 50 % regions of the half cycles, respectively. Considering that the data window of only the last 30 % of each half cycle is used to extract the EDM observable in the drift-corrected algorithm, the voltage drift is improved greatly by a factor of 33 (recall that the smallest voltage drift which can be obtained in the lab was ~ 10 ppm/s).

In addition to the improvement of the low-drift drive source, a new scheme is planned to upgrade the HV polarity switch system to be capable of handling polarity switching between higher HVs than now, up to ± 20 kV. Both Stanford Research PS370 and PS375 DC HV supplies will be employed to apply positive and negative 20 kV to the plate of the vacuum-tube triodes. Attempts at improving the feedback circuit will also be done by adding a proportional-integral-differential (PID) controller to gain more stability of the HV output. Successful development of this upgrade will enhance the EDM sensitivity by a factor of 4.

7.2.4 Conclusion

In this section, further improvements for the electron EDM sensitivity are proposed. In addition to lowering the temperature of the EDM experiment, optimizing the geometry of the present prototype system, and increasing the electric fields up to

40 kV_{pp}, it is hoped that increasing the number of sample/electrode assemblies (of the type used in the prototype experiment) to eight can further improve the sensitivity. A better SQUID sensor with lower noise and a larger flux transfer efficiency will also be employed. With these proposed future improvements, the GGG-based EDM experiment is capable of improving the experimental EDM sensitivity to and beyond atomic beam-based experiments.

Appendix A

Magnetic Property Measurement at Milli-Kelvin Temperatures

To characterize magnetic properties of the GGG solid at milli-Kelvin temperatures, the solid needs to be cooled by a dilution refrigerator which is able to reach low temperature of about 20 mK. The DC SQUID-based susceptometer [54] available down to 2 K moves the sample through a pickup coil to detect the induced sample magnetization under a external magnetic field, however it would be difficult to employ this method in a dilution refrigerator in which cooling is achieved by thermal contact with the mixing chamber plate (details in Ref. [83]). To that end, this dedicated instrumentation requires a new design for the susceptometer so that it can operate at such a low temperature in the dilution refrigerator.

A.1 Design and Method

A possible alternative to moving the sample is applying a uniform AC magnetic field to the sample while a sensing coil detects the corresponding AC induced sample magnetization through Faraday's law, leading to a measurement of the AC magnetic susceptibility. As opposed to the DC magnetic susceptibility, the AC susceptibility

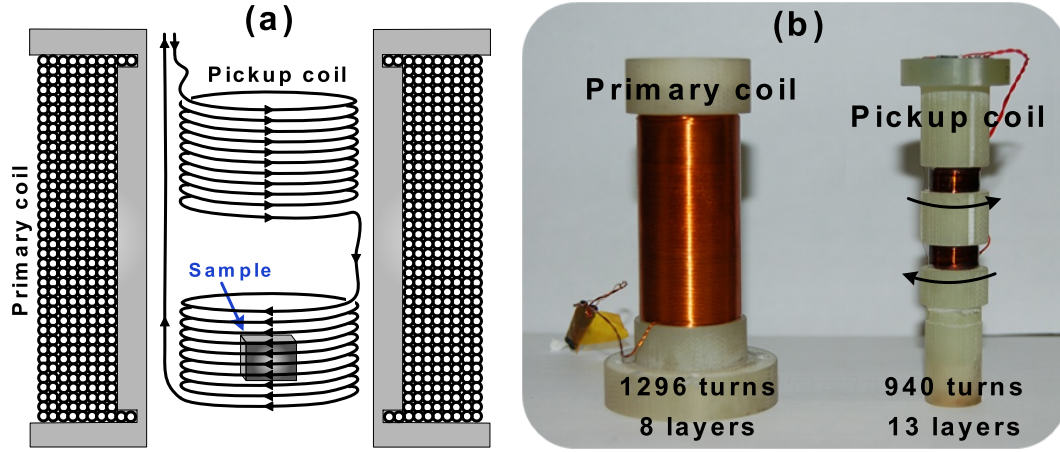


Figure A.1: AC susceptometer apparatus. (a) schematic of the AC susceptometer design. (b) Photograph of the home-made set of AC susceptometer coils, the primary coil (left) and the pickup coil (right).

is a function of both temperature and frequency. Hence, the AC magnetic susceptibility measurements yield critical information about sample magnetization dynamics. Based on the experimental idea, I have designed and built a new AC susceptometer guided by Ref. [84]. Fig. A.1(a) displays a sketch of the configuration of the AC susceptometer coils. The susceptometer is composed of a primary coil in a solenoid configuration which produces a uniform AC magnetic field and a pickup coil in a pair configuration which senses the induced sample magnetization. The primary coil surrounds the pickup coil which contains two counter-wound sections as a gradiometer, reference coil (upper) and sample coil (lower) in which the sample stays at its center. Assuming both reference and sample coils are identical, the common-mode magnetic signals from applied and ambient fields are completely eliminated and thus only the magnetic signals due to sample magnetization is measured. Therefore, a high degree of conformity of the coils is required for higher experimental accuracy. The same cube-shaped polycrystalline GGG sample used in the DC susceptibility measurement is situated using vacuum grease in a custom-made sample holder made of quartz. The

use of quartz is to maximize the thermal conductivity with the mixing chamber plate (see Ref. [83]).

Furthermore, the non-metallic quartz suppresses substantially possible signal distortions due to eddy currents induced on the sample holder. As shown in Fig. A.1(b), the primary coil and each pickup coil section (reference and sample coils) are wound around a non-metallic G10 structure using a wire-winding machine. The primary coil has a length of 4.8 cm and a radius of 1.0 cm, while each pickup coil section has a length of 0.51 cm and 0.51 cm radius. The distance between the pickup coil sections is 1.3 cm. Note that the axial center of the primary coil is same as the center of the pickup coil. The primary coil contains 1296 windings with 8 layers of 30 AWG insulated copper wire and each pickup coil section contains 940 windings with 13 layers of 42 AWG insulated copper wire. The use of G10 material limits the Joule heating generated in the coils from transferring into the mixing chamber through thermal contact. In particular, the set of AC susceptometer coils is located 2.3 cm away from the mixing chamber plate in order to sufficiently reduce the eddy current heating on the plate, but maintain good thermal conductivity through the sample holder.

In practice, the internal axial magnetic field generated by the finite size of solenoid (primary coil) is not uniform everywhere. The axial magnetic field can be written as follows, using Eq. B.7 in Appendix B followed by supplementary calculations:

$$B(z) = \frac{\mu_0 n I}{2} \left[\frac{h + l - z}{\sqrt{r^2 + (h + l - z)^2}} - \frac{l - z}{\sqrt{r^2 + (l - z)^2}} \right]. \quad (\text{A.1})$$

Here n is the number of turns per unit length, h and r is the solenoid length and radius respectively, and l is the axial distance from the immediate current loop and the mixing chamber plate. Values of these variables were discussed above. Assuming the plate is positioned at $z = 0$, the expected $B(z)$ profile is plotted in Fig. A.2. Two dashed lines on the plot indicate the area of the primary coil. According to the plot, only 4 % of the axial field will contribute to generation of the eddy current on the mixing chamber plate, confirming that the design of the AC susceptometer is suitable for this measurement. Since the field profile exhibits a non-uniformity in the

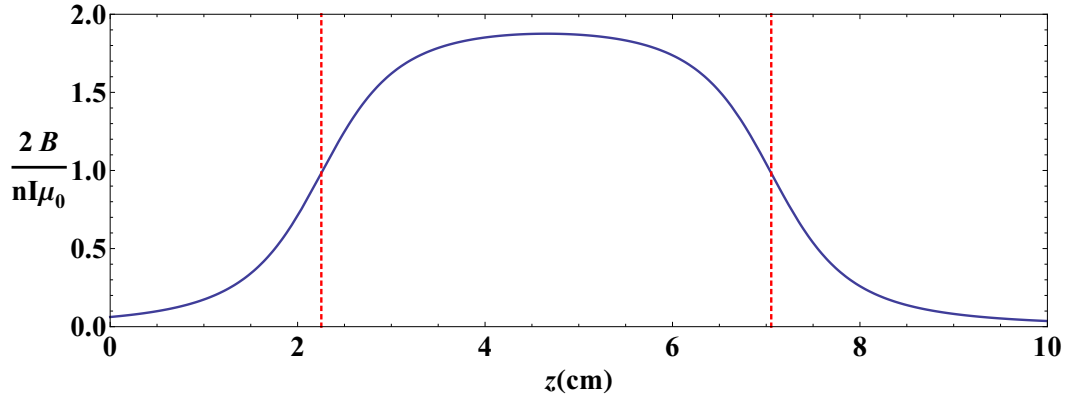


Figure A.2: The expected axial field profile generated by the primary coil. Two dashed red lines indicate the placement of the primary coil.

axial field inside the primary coil, I have supplemented two reinforcement side coils, each with 2 layers in the primary coil in order to homogenize the field as shown in Fig. A.1(b). The advantage of the reinforcement coils is described in Ref. [85]. Based on the field uniformity investigation, the best location for the pickup coil was chosen. For further homogeneity of the axial field, the length of the primary coil could be increased.

The AC susceptometer with the sample is mounted on the mixing chamber plate (made of copper) in the dilution refrigerator (Oxford instruments Model 75) using ceramic screws. Having the primary coil generating the AC magnetic field, voltage signals from the pickup coil are measured by a lock-in amplifier (SIGNAL RECOVERY model 7265) in volts rms which allows the signals to be separated from the noise. The internal oscillator of the lock-in amplifier is used for both the primary coil and the reference signal for the pickup coil. The current flowing on the primary coil is measured by a multimeter (Keithley Model 2000) in currents rms. A temperature sensor [86] is mounted using Stycast 2850 epoxy at a position closest to the sample on the sample holder surface to monitor the temperature at the sample. The resistance of the primary and pickup coils are measured to be $24 \, \Omega$ and $27 \, \Omega$ at a temperature

of 4 K respectively.

With the applied field H_a oscillating sinusoidally along the sample at a frequency of ω , the voltage signals from the reference coil and sample coil are expressed by Eq. A.2 and Eq. A.3 respectively.

$$V_r = -\frac{d\Phi_r}{dt} = -A_p N \frac{dH_a}{dt} - M_r \frac{dI_a}{dt} \quad (\text{A.2})$$

$$V_s = -\frac{d\Phi_s}{dt} = -N \left(A_p \frac{dH_a}{dt} + A_s \frac{dM}{dt} \right) - M_s \frac{dI_a}{dt} \quad (\text{A.3})$$

where N is the total number of turns of the reference and sample coils, A_p and A_s is the cross-sectional area of the pickup coil and the sample, I_a is the current flowing on the primary coil, M_r is the mutual inductance between the primary coil and the reference coil, M_s is the mutual inductance between the primary coil and the sample coil, and M is the induced sample magnetization. The total induced electromotive force V_p in the pickup coil is given by

$$\begin{aligned} V_p &= V_r - V_s \\ &= A_s N \frac{dM}{dt} + (M_s - M_r) \frac{dI_a}{dt} \\ &= A_s N \chi \frac{dH_a}{dt} + (M_s - M_r) \frac{dI_a}{dt}. \end{aligned} \quad (\text{A.4})$$

It should be noted that $\frac{dM}{dt} = \frac{dM}{dH} \frac{dH}{dt}$ and $\frac{dM}{dH} = \chi$. The relation of $H_a = \mu_0 n I_a = \mu_0 n I_0 e^{i\omega t}$ gives another expression as follows:

$$V_p = A_s N \chi \mu_0 n \omega I_0 + (M_s - M_r) \omega I_0. \quad (\text{A.5})$$

The AC magnetic susceptibility of the GGG sample can be estimated by the first term, the second term is the unwanted background due to mismatch between the pickup coil sections.

To limit the background, I subtract the V_p measured at a certain temperature from that measured at room temperature because the magnetic susceptibility at 300 K is almost zero. With this trick, the background-free magnetic susceptibility can be

estimated by

$$\chi(T) = \frac{1}{A_s N \mu_0 n \omega} \left[\frac{V_p(T) - V_p(300 \text{ K})}{I_0} \right]. \quad (\text{A.6})$$

In order to determine experimentally the value of the term $[V_p(T) - V_p(300 \text{ K})]/I_0$ in the equation, I changed the amplitude of applied magnetic field with the frequency fixed, that is, I changed the current strength flowing on the primary coil, and then measured each corresponding V_p at both temperatures T and 300 K. This measurement allows one to plot the linear graph of $V_p(T) - V_p(300 \text{ K})$ as a function of I_0 . The least-square line fit performed on the graph gives the value of the term in question. Based on this experimental method, I can investigate the temperature dependence of the AC magnetic susceptibility by changing the sample temperature. The temperature control is achieved by the Quantum Design resistance bridge coupled to the RuO thermal sensor located on the mixing chamber plate.

A.2 Preliminary Results

Fig. A.3 shows the preliminary results of the AC volume magnetic susceptibility in CGS unit, measured at a temperature decreasing toward 150 mK from 1.2 K, including the DC magnetic susceptibility measured using the DC susceptometer for comparison. The measurement was performed at different applied field frequencies of 1250 Hz, 830 Hz, and 475 Hz for additional search for the frequency dependence. Note that the correction for the demagnetization effect is already applied to these results using Eq. 3.4. The AC susceptibility increases continuously as the GGG solid is cooled. No order-disorder phase transition is observed down to 150 mK. However, we need a more accurate measurement with an improved AC susceptometer apparatus and lower temperatures so as to clarify where the Néel or freezing temperature is. In addition to the temperature dependence, the measured χ shows a frequency dependence, implying random spin fluctuations [43] which indicate the spin glass transition in the magnetic system.

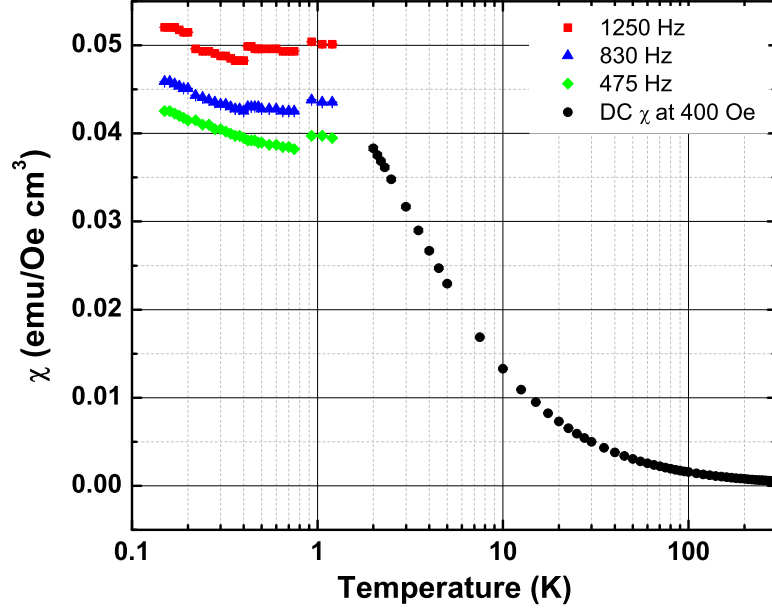


Figure A.3: AC volume magnetic susceptibility of the GGG sample as a function of temperature, measured at frequencies 1250 Hz (red squares), 830 Hz (blue triangles), and 475 Hz (green diamonds) and temperatures ranging from 1.2 K to 150 mK. The DC susceptibility (black circles) measured at a maximum applied magnetic field of 400 Oe is also displayed together for comparison. The x -axis is in log scale.

A.3 Future Work

To enhance the experimental accuracy in the AC susceptibility determination, an improvement of the AC susceptometer apparatus is essential. For further homogeneity of applied magnetic fields along the pickup coil/sample assembly, more reinforcement side coils or a longer primary coil might be required. The reinforcement coil influence on the field homogeneity can be studied using the finite-element analysis calculations. Several layers of superconducting shield that surround the whole AC susceptometer must be installed to allow the susceptometer to be shielded from ambient fields, thereby increase the susceptibility sensitivity. In addition to the sensitivity

enhancement, the shield prevents the AC fields from leaking into the mixing chamber plate, so that the eddy current heating can be minimized. Note that the magnetic field change occurs inside the shield, hence the field simulations with and without the shield are also necessary.

The Joule heating of the primary coil should be minimized and more importantly the eddy current heating on the mixing chamber plate must be controlled below the cooling power of the dilution refrigerator, making it possible to reach extreme low temperatures. It is also required that no magnetic materials are situated near the AC susceptometer and temperature stabilization is achieved. In addition, the current signal detection circuit of the AC susceptometer must be improved to effectively suppress the background. Ref. [87] could be a good example for that. Lastly, calibration of the AC susceptometer must be accomplished using a standard sample such as Gd_2O_3 or by the Curie-Weiss behavior observed above 2 K. Larger sample volume and higher applied field can also increase the sensitivity.

Appendix B

Analytical Model for Geometry-Dependent Flux Suppression

An analytical model for explaining the magnetic flux suppression in the disk-shaped sample used in the EDM measurement can be developed by treating the uniform bulk magnetization \mathbf{M} inside the sample as a current flowing on the sample surface in accordance with the Stokes' theorem. More specifically, the surface current arises from the surface current density \mathbf{K}_M induced by the homogenous magnetization \mathbf{M} with the relation of $\mathbf{K}_M = \mathbf{M} \times \mathbf{n}$ where \mathbf{n} is the normal vector pointing outward¹. To develop the analytical model, I begin with calculating a magnetic field \mathbf{B} at an arbitrary position p induced by a single circular loop of steady current I as shown in Fig. B.1.

In cylindrical coordinates, each vector that appears in Fig. B.1 can be written by $\mathbf{r} = \rho\hat{\rho} + z\hat{z}$, $\mathbf{r}' = \rho'\hat{\rho}'$, and $d\mathbf{l} = \rho'd\phi'\hat{\phi}'$. According to the Biot-Savart Law, the

¹The bound current density $\mathbf{J}_M = \nabla \times \mathbf{M}$ does not survive because \mathbf{M} is constant throughout the sample volume.

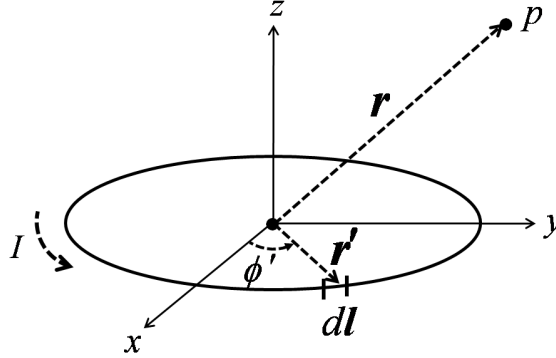


Figure B.1: A single circular loop carrying a steady current I with a radius of ρ'

induced magnetic field at the position p is given by

$$\mathbf{B}(\mathbf{r}) = \frac{\mu_0 I}{4\pi} \int d\mathbf{l} \times \frac{(\mathbf{r} - \mathbf{r}')}{|\mathbf{r} - \mathbf{r}'|^3} \quad (\text{B.1})$$

where $|\mathbf{r} - \mathbf{r}'| = \{(\rho \cos \phi - \rho' \cos \phi')^2 + (\rho \sin \phi - \rho' \sin \phi')^2 + z^2\}^{1/2}$ in rectangular coordinates. In addition, the cross-product term in the integral is written in rectangular coordinates

$$\begin{aligned} d\mathbf{l} \times (\mathbf{r} - \mathbf{r}') &= \rho' d\phi' \hat{\phi}' \times (\rho \hat{\rho} + z \hat{z} - \rho' \hat{\rho}') \\ &= \rho' \cos \phi' d\phi' z \hat{x} + \rho' \sin \phi' d\phi' z \hat{y} + [\rho'^2 - \rho \rho' \cos(\phi - \phi')] d\phi' \hat{z}. \end{aligned} \quad (\text{B.2})$$

Here $\hat{\phi}' \times \hat{\rho} = -\cos(\phi - \phi') \hat{z}$. Accordingly, each component of the magnetic induction is as follows:

$$B_x = \frac{\mu_0 I}{4\pi} \int_0^{2\pi} \frac{\rho' \cos \phi' z}{[(\rho \cos \phi - \rho' \cos \phi')^2 + (\rho \sin \phi - \rho' \sin \phi')^2 + z^2]^{3/2}} d\phi', \quad (\text{B.3})$$

$$B_y = \frac{\mu_0 I}{4\pi} \int_0^{2\pi} \frac{\rho' \sin \phi' z}{[(\rho \cos \phi - \rho' \cos \phi')^2 + (\rho \sin \phi - \rho' \sin \phi')^2 + z^2]^{3/2}} d\phi', \quad (\text{B.4})$$

$$B_z = \frac{\mu_0 I}{4\pi} \int_0^{2\pi} \frac{\rho'^2 - \rho \rho' \cos(\phi - \phi')}{[(\rho \cos \phi - \rho' \cos \phi')^2 + (\rho \sin \phi - \rho' \sin \phi')^2 + z^2]^{3/2}} d\phi'. \quad (\text{B.5})$$

We are only interested in the z component of the magnetic induction because the flux pickup coil is only sensitive to the EDM-induced magnetic fields which lie in the z direction in the experiment. Note that since the induced magnetic field has rotational

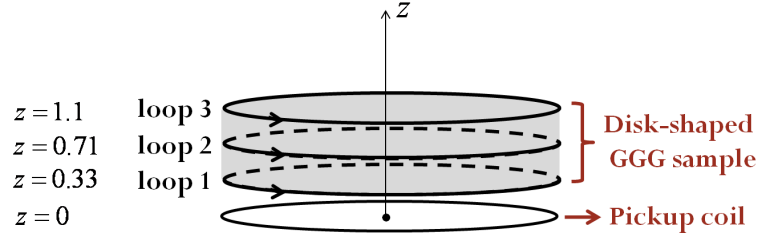


Figure B.2: Simplified disk-shaped GGG sample as a stack of three identical current rings with a distance of 0.38 cm between the rings. The flux pickup coil is placed 0.33 cm away from the immediate ring as the actual experimental setup.

symmetry with respect to the z -axis, we can set the variable of ϕ to be $\pi/2$. This simplicity leaves the following result of B_z (Eq. B.5),

$$B_z = \frac{\mu_0 I \rho'^2}{4\pi} \int_0^{2\pi} \frac{1 - \frac{\rho}{\rho'} \sin \phi'}{[(\rho' \cos \phi')^2 + (\rho - \rho' \sin \phi')^2 + z^2]^{3/2}} d\phi'. \quad (\text{B.6})$$

Next, the disk-shaped GGG sample with diameter 3.3 cm and height 0.76 cm is considered as a combination of many current loops in a solenoid configuration. Then the current flowing on the solenoid is written by $Indz$ where n is the number of turns per unit length. Assuming $n = 1$ for simplicity, Eq. B.6 should be integrated with respect to z :

$$B_z = \frac{\mu_0 I \rho'^2}{4\pi} \int_a^{a+0.76} \int_0^{2\pi} \frac{1 - \frac{\rho}{\rho'} \sin \phi'}{[(\rho' \cos \phi')^2 + (\rho - \rho' \sin \phi')^2 + (z - z')^2]^{3/2}} d\phi' dz. \quad (\text{B.7})$$

Here, the variable a is the distance along the z -axis between the observable point p and the immediate current loop. Eventually, Eq. B.7 is the final analytical model for the measured EDM-induced magnetic field.

The integral of the final analytical model Eq. B.7 is not easy to solve. Therefore, I need to make the analytical model as simple as possible. To this end, the disk-shaped sample is simplified as a stack of three identical current loops as shown in Fig. B.2. Two current loops are positioned at both ends and the other is located at the center of the sample. The distance between the loops is 0.38 cm. The flux pickup coil is

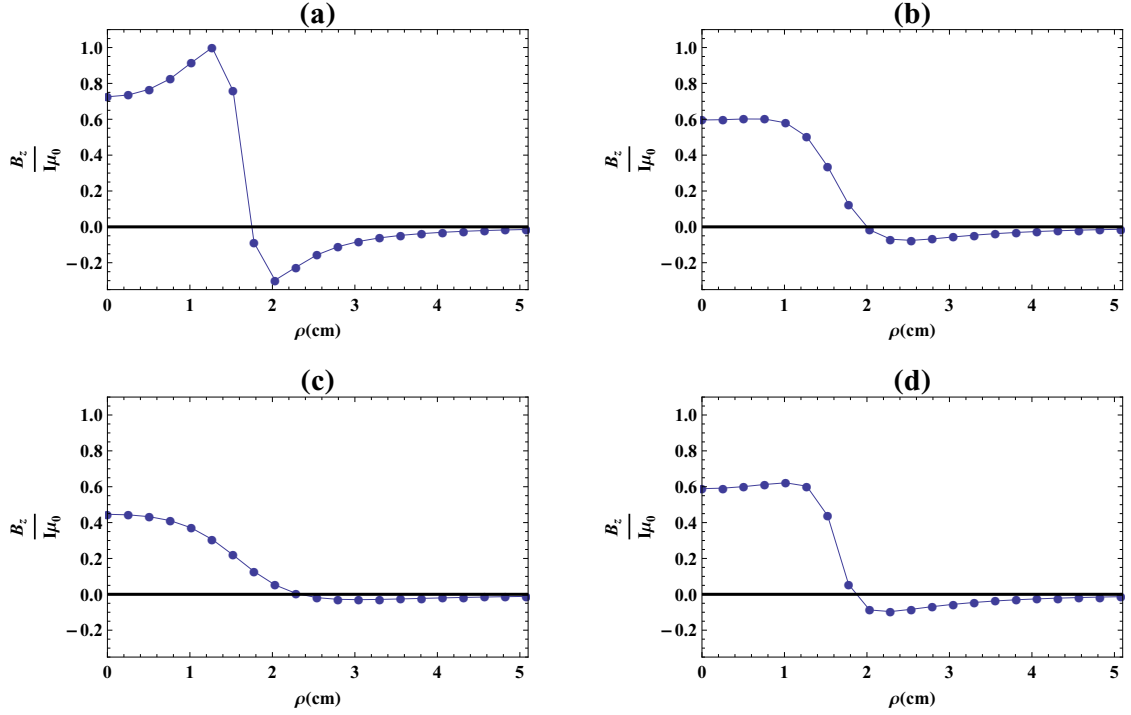


Figure B.3: Solutions of the simplified analytical model. (a), (b), and (c) show the magnetic induction from each current loop 1, 2, and 3. (d) shows the total induced magnetic field by all current loops normalized by number of loops.

placed 0.33 cm away from the immediate loop (loop 1) as the actual experimental setup (details in Sec. 4). Since the pickup coil is positioned at $z = 0$, the variable z in Eq. B.7 disappears. The current loop radius ρ' is set to 1.7 cm identical to the radius of the sample. In addition, the variable z' is also set to be 0.33, 0.71, and 1.1 cm for current loops 1, 2, and 3 respectively. Based on these simplifications, we can estimate the total induced magnetic field by the current loops at different observable positions of ρ . The result can be compared to that from the finite-analysis calculations in

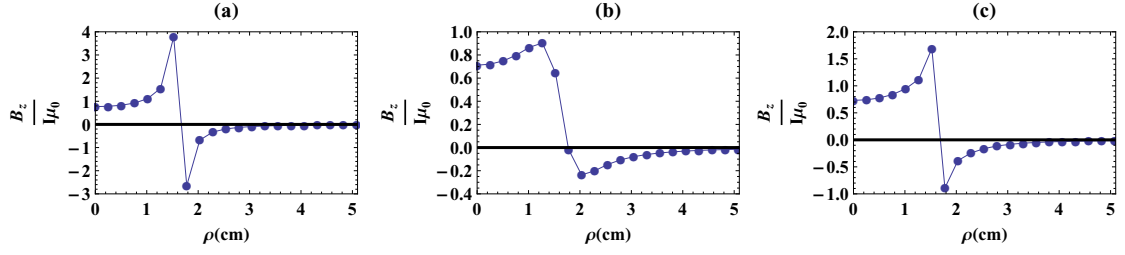


Figure B.4: Solutions of the analytical model when the pickup coil is positioned at the center of the sample ($z = 0.71$ cm). (a) and (b) are magnetic inductions by the current loop 2 and current loop 1 or 3, respectively. (c) is the total induced magnetic field by all current loops normalized by number of current loops.

Sec. 4. The final simplified analytical model is written by

$$\begin{aligned} \frac{B_z(\rho)}{\mu_0 I} = \frac{1.7^2}{4\pi} \left\{ \int_0^{2\pi} \frac{1 - \frac{\rho}{1.7} \sin \phi'}{[(1.7 \cos \phi')^2 + (\rho - 1.7 \sin \phi')^2 + (0.33)^2]^{3/2}} d\phi' \right. \\ + \int_0^{2\pi} \frac{1 - \frac{\rho}{1.7} \sin \phi'}{[(1.7 \cos \phi')^2 + (\rho - 1.7 \sin \phi')^2 + (0.71)^2]^{3/2}} d\phi' \quad (B.8) \\ \left. + \int_0^{2\pi} \frac{1 - \frac{\rho}{1.7} \sin \phi'}{[(1.7 \cos \phi')^2 + (\rho - 1.7 \sin \phi')^2 + (1.1)^2]^{3/2}} d\phi' \right\}. \end{aligned}$$

To calculate this equation, the numerical mathematics software package Wolfram Mathematica is employed. The solutions are plotted in Fig. B.3. Here ρ is chosen ranging from 0 to 5.1 cm with an interval of 0.25 cm. Fig. B.3(a), (b), and (c) show induced magnetic fields by the current loop 1, 2, and 3 respectively, while (d) is the total induced magnetic field by all current loops, normalized by number of loops. The total magnetic induction is comparable to Fig. 4.7(b). It should be noted that these solutions of the analytical model are symmetric about $\rho = 0$. The analytical solutions show non-uniform magnetic fields as the solutions of the finite-element analysis calculations.

Furthermore, I consider the case where the pickup coil is situated at the center of the sample ($z = 0.71$ cm), leading to a modification of the analytical model Eq. B.8

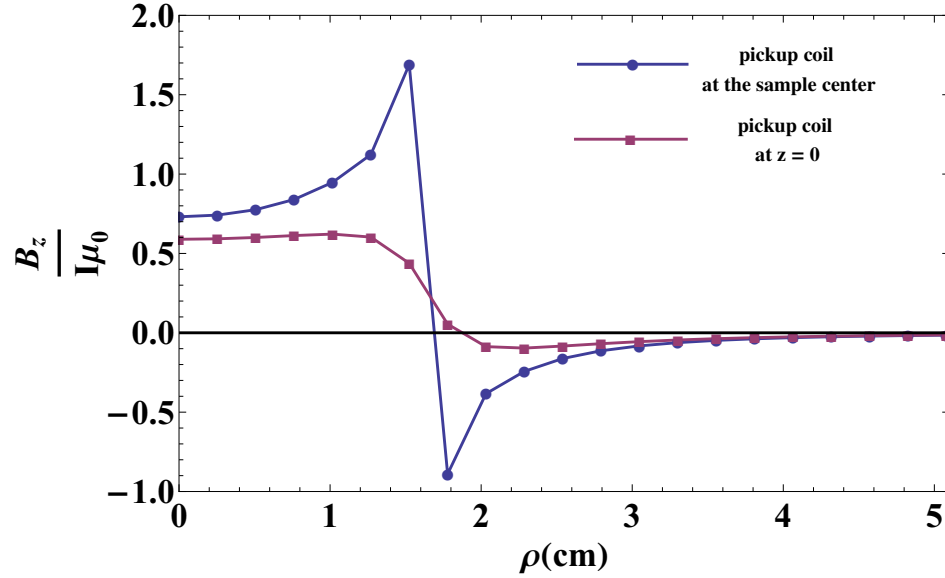


Figure B.5: Analytical solutions of the EDM-induced magnetic field with two different positions of the pickup coil. Data points with square dots and circular dots for the pickup coil positioned at $z = 0$ and at the sample center, respectively.

as follows:

$$\begin{aligned} \frac{B_z(\rho)}{\mu_0 I} = & \frac{1.7^2}{4\pi} \left\{ \int_0^{2\pi} \frac{1 - \frac{\rho}{1.7} \sin \phi'}{[(1.7 \cos \phi')^2 + (\rho - 1.7 \sin \phi')^2 + (-0.38)^2]^{3/2}} d\phi' \right. \\ & + \int_0^{2\pi} \frac{1 - \frac{\rho}{1.7} \sin \phi'}{[(1.7 \cos \phi')^2 + (\rho - 1.7 \sin \phi')^2 + (0)^2]^{3/2}} d\phi' \\ & \left. + \int_0^{2\pi} \frac{1 - \frac{\rho}{1.7} \sin \phi'}{[(1.7 \cos \phi')^2 + (\rho - 1.7 \sin \phi')^2 + (0.38)^2]^{3/2}} d\phi' \right\}. \end{aligned} \quad (\text{B.9})$$

The solutions of this analytical model are plotted in Fig. B.4. Fig. B.4(a) is originating from the current loop 2, while (b) is from the current loop 1 or 3. Fig. B.4(c) shows the final total induced magnetic field by all current loops normalized by number of loops. Comparison of the total magnetic field pickups between different positions of the pickup coil is displayed in Fig. B.5. Data points marked with squares correspond to the pickup coil positioned at $z = 0$ and circles corresponds to the pickup coil positioned at the sample center. It is conspicuous that the magnetic field pickup

when the pickup coil is at the sample center is much larger than the $z = 0$ case. The results are nearly identical to the numerical solutions (see Fig. 4.8(b)). Based on these analytical solutions, I have double checked that the EDM-induced magnetic flux is suppressed due to the sample geometry and additionally due to the placement of the pickup coil. Thus, the simplified analytical model built in this Appendix provides a clearer understanding of our electron EDM experiment.

Appendix C

Matlab Script for Data Control and Data Storage

The Matlab script for data control and data storage used in the EDM measurements is as follows.

```
1 function eEDM_measurement
2 %Data control
3 %-----
4 clear all
5 Frequency=715; % Trigger rate (Hz)
6 Drive_fre=1.43; % frequency of HV drive (Hz)
7 Storage_Time=3.5; % desired collecting time (hours)
8 Test_Sample=(Frequency/Drive_fre)*3;
9 OSR_VAL = uint8(hex2dec('1F')); % 256 OSR
10 IP_ADDR = '129.79.152.201'; % set IP address
11 %Create new folder for data storage
12 folder_unsigned=strcat('E:\Program ...
    Files\MATLAB71\work\youngjin\eEDM\071610\run2\unsigned');
13 mkdir(folder_unsigned) % for hexadecimal data
14 folder=strcat('E:\Program ...
```

```
Files\MATLAB71\work\youngjin\EDM\071610\run2\signed');
15 mkdir(folder) % for real data
16 %connect to trigger source
17 Trigger=gpib('ni',0,17);
18 fopen(Trigger);
19 command_string=sprintf('Frequency %d', Frequency);
20 fprintf(Trigger,command_string); % set trigger frequency
21 fprintf(Trigger,'OUTPut:SYNC OFF'); % Trigger source off
22 READ_PORT = 10001;
23 READ_PKTS = 24000;
24 Save_Break=15;
25 PACKET_SIZE = 40; %bytes
26 Naverage=int32((Storage_time*Frequency*60*60)/READ_PKTS*Save_Break));
27 READ_BYTES = PACKET_SIZE * READ_PKTS * Save_Break * Naverage;
28 READ_TIMEOUT = READ_BYTES * 2;
29 GPIO_PORT = hex2dec('77F0');
30 %-----
31
32 %Ready for Data storage: HVs, Leakage currents, and SQUID
33 %-----
34 %Reset the FPGA
35 reset_fpga(IP_ADDR,GPIO_PORT);
36 %Try to establish the connection to xport
37 con=pnet('tcpconnect',IP_ADDR,READ_PORT);
38 if con ≥ 0
39     %Connection sccessfully established
40     disp(['Connection successful, con = ' num2str(con)]);
41     %Set the OSR value
42     pnet(con,'write',OSR_VAL,'network');
43     disp(['OSR timeout set to ' dec2hex(OSR_VAL)]);
44     %Set the read timeout
45     pnet(con,'setreadtimeout',READ_TIMEOUT);
46     disp(['Read timeout set to ' num2str(READ_TIMEOUT)]);
47     %Get data from the connection and write it to a file
```

```
48     disp(['Waiting to receive ' num2str(READ_BYTES) ' bytes.']);
49     %Start trigger
50     fprintf(Trigger, 'OUTPut:SYNC On');
51
52     %Check 3 cycles of data
53     Test=pnet(con, 'read', [PACKET_SIZE Test_Sample 1], 'uint8');
54     %Analysis the data (convert hexadecimal data to integer data)
55     ADC_BITS = 28;    %total ADC bits
56     NUM_CHS = 8;      %number of channels
57     PKT_SZ = 40;      %bytes
58     SPL_SZ = 4;       %bytes in each channel
59     HEADER = uint32(2^(8*SPL_SZ)); % header is always FFFF
60     temp = uint32(0);
61     ch_idx = 1;
62     for run=1:1:Test_Sample
63         for i=1:SPL_SZ:PKT_SZ
64             %Get the header
65             if (i == 1)
66                 %Coherently sum the bytes to get value
67                 for j=1:1:SPL_SZ
68                     temp = temp + ...
69                         bitshift(uint32(test(j+i-1,run,1)), (SPL_SZ-j)*8);
70                 end;
71                 %Check for a valid header
72                 if (temp == HEADER)
73                     disp('Invalid file');
74                     break;
75                 end;
76             elseif (i== 5)
77                 temp = uint32(0);
78                 for j=1:1:SPL_SZ
79                     temp= temp + ...
80                         bitshift(uint32(test(j+i-1,run,1)), (SPL_SZ-j)*7);
```

```
80         end;
81         time_stamp_test(run) = double(temp);
82     else
83         temp = uint32(0);
84         for j=1:1:SPL_SZ
85             temp= temp + ...
86                 bitshift(uint32(test(j+i-1,run,1)),(SPL_SZ-j)*7);
87         end;
88         %make signed double
89         if temp > (2^(ADC_BITS-1)-1)
90             val = double(temp) - 2^ADC_BITS;
91         else
92             val = double(temp);
93         end;
94         signed(run,ch_idx) = val*(10/2^27);
95         if ch_idx < NUM_CHS
96             ch_idx = ch_idx + 1;
97         else
98             ch_idx = 1;
99         end;
100     end;
101 end;
102 %plot out the 3 cycles of data
103 figure(1)
104 subplot(2,3,1)
105 plot(signed(:,1),'.-');
106 title('SQUID Signal')
107 subplot(2,3,2)
108 plot(signed(:,4),'.-');
109 title('HV1 monitor')
110 subplot(2,3,3)
111 plot(signed(:,5),'.-');
112 title('HV2 monitor')
```

```
113     subplot(2,3,4)
114     plot(signed(:,7),'.-');
115     title(' LC1 monitor')
116     subplot(2,3,5)
117     plot(signed(:,8),'.-');
118     title(' LC2 monitor')
119     %-----
120
121     %Start collecting data
122     %-----
123     %Save the start time of measurement
124     tmp_time=str2num(datestr(now,'HH.MMSS'));
125     runtime(1,1)=tmp_time;
126     %collecing larage amount of data for the desired time
127     for measure=1:Save_Break
128         unsigned=pnet(con,'read',[PACKET_SIZE READ_PKTS ...
129             Naverage], 'uint8');
129         fname=sprintf('%d.mat',measure);
130         save_file=strcat(folder_unsigned,'\ ',fname);
131         save(save_file, 'unsigned');
132     end
133     %Save the end time of measurement
134     tmp_time=str2num(datestr(now,'HH.MMSS'));
135     runtime(1,2)=tmp_time;
136     save_file=strcat(folder_unsigned,'\runtime.mat');
137     save(save_file, 'runtime');
138     %Stop trigger
139     fprintf(Trigger,'OUTPut:SYNC OFF');
140
141     %Close the connection from data port
142     pnet(con,'close');
143     disp('Connection closed');
144 else
145     %Connection attempt failed.
```

```
146     disp(['Connection failed, con = ' num2str(con)]);
147 end;
148 fclose(Trigger);
149 %-----
150
151 %Convert hexadecimal data to integer data
152 %-----
153 pause(1);
154 ADC_BITS = 28;
155 NUM_CHS = 8;
156 PKT_SZ = 40;
157 SPL_SZ = 4;
158 HEADER = uint32(2^(8*SPL_SZ));
159 temp = uint32(0);
160 ch_idx = 1;
161 for iterate=1:Save_Break
162     cd(folder_unsigned)
163     fname=sprintf('%d.mat',iterate);
164     load(fname)
165     for scan=1:Naverage
166         signed = zeros(READ_PKTS,NUM_CHS);
167         time_stamp=zeros(1,READ_PKTS);
168         for run=1:1:READ_PKTS
169             for i=1:SPL_SZ:PKT_SZ
170                 if (i == 1)
171                     for j=1:1:SPL_SZ
172                         temp=temp+ ...
173                             bitshift(uint32(unsigned(j+i-1,run,scan)), ...
174                                     (SPL_SZ-j)*8);
175                     end
176                     if (temp == HEADER)
177                         disp('Invalid file');
178                         break;
```



```
178         end
179     elseif (i== 5)
180         temp = uint32(0);
181         for j=1:1:SPL_SZ
182             temp=temp+ ...
183                 bitshift(uint32(unsigned(j+i-1,run,scan)), ...
184                     (SPL_SZ-j)*7);
185         end
186         time_stamp(run) = double(temp);
187     else
188         temp = uint32(0);
189         for j=1:1:SPL_SZ
190             temp=temp+ ...
191                 bitshift(uint32(unsigned(j+i-1,run,scan)), ...
192                     (SPL_SZ-j)*7);
193         end
194         if temp > (2^(ADC_BITS-1)-1)
195             val = double(temp) - 2^ADC_BITS;
196         else
197             val = double(temp);
198         end
199         signed(run,ch_idx) = val*(10/2^27);
200         if ch_idx < NUM_CHS
201             ch_idx = ch_idx + 1;
202         else
203             ch_idx = 1;
204         end
205     end
206 end
207
208 if (scan≥2)
209     data=cat(1,data,signed); % combine samples each ...
210                             READ_PKTS*Naverage samples
211     time=cat(2,time,time_stamp);
```

```
207         else
208             data=signed;
209             time=time_stamp;
210         end
211     end
212     fname=sprintf('%d.mat',iterate);
213     save_file=strcat(folder,'\ ',fname);
214     save(save_file, 'data');
215     timename=sprintf('time_%d.mat',iterate);
216     save_file=strcat(folder,'\ ',timename);
217     save(save_file, 'time');
218 end
219 %-----
220
221 %rest FPGA
222 %-----
223 function reset_fpga(ip,port)
224 %This command will assert CP2 (GPIO1) to reset the FGPA
225 GPIO_FPGA_RST_A = ['1B'; '02'; '00'; '00'; '00'; '02'; '00'; ...
226     '00'; '00'];
227 %This command will de-assert CP2 (GPIO1) to reset the FGPA
228 GPIO_FPGA_RST_D = ['1B'; '02'; '00'; '00'; '00'; '00'; '00'; ...
229     '00'; '00'];
230
231 %Size of the XPort response to GPIO command
232 RESPONSE_SZ = 5;
233
234 %Try to establish the connection
235 disp(['Trying to connect to GPIO port ' ip ':' num2str(port) '...']);
236 con=pnet('tcpconnect',ip,port);
237 if con >= 0
238     %Connection successfully established
239     disp(['Connection successful, con = ' num2str(con)]);
240
241     %Wait a bit for the response
```

```
239     pnet(con,'setreadtimeout',5);
240
241     %Write the GPIO command to assert the FPGA reset.
242     pnet(con,'write',uint8(hex2dec(GPIO_FPGA_RST_A)), 'network');
243     disp(['Reset FPGA with GPIO port command ' ...
           num2str(hex2dec(GPIO_FPGA_RST_A))]);
244
245     %Get the return value from the XPort
246     disp('Waiting for response...');
247     data=pnet(con,'read',RESPONSE_SZ,'uint8');
248     %Check the return value
249     if sum(data) == (hex2dec('1B') + hex2dec('02'))
250         disp(['Received response of ' num2str(data)]);
251
252         %Write the GPIO value to release the FPGA reset.
253         pnet(con,'write',uint8(hex2dec(GPIO_FPGA_RST_D)), 'network');
254         disp(['Release FPGA with GPIO port command ' ...
               num2str(hex2dec(GPIO_FPGA_RST_D))]);
255
256         %Get the return value from the XPort
257         disp('Waiting for response...');
258         data=pnet(con,'read',RESPONSE_SZ,'uint8');
259
260         %Check the return value from the XPort
261         if sum(data) == hex2dec('1B');
262             disp(['Received response of ' num2str(data)]);
263         else
264             disp('FPGA reset de-assertion failed');
265         end;
266     else
267         disp('FPGA reset assertion failed');
268     end;
269
270     %Close the connection
```

```
271     pnet(con, 'close');
272     disp('Connection to GPIO port closed');
273
274 else
275     %Connection attempt failed.
276     disp(['Connection to GPIO port failed, con = ' num2str(con)]);
277 end;
278 %
```

Bibliography

- [1] R. Dalitz, *Philosophical Magazine* **44**, 1068 (1953).
- [2] O. Laporte, *Zeitschrift für Physik* **23**, 135 (1924).
- [3] T. D. Lee and C. N. Yang, *Physical Review* **104**, 254 (1956).
- [4] C. S. Wu, E. Ambler, R. W. Hayward, D. D. Hoppes, and R. P. Hudson, *Physical Review* **105**, 1413 (1957).
- [5] R. L. Garwin, L. M. Lederman, and M. Weinrich, *Physical Review* **105**, 1415 (1957).
- [6] CPLEAR Collaboration, *Physics Letters B* **444**, 43 (1998).
- [7] Ezequiel Álvarez and Alejandro Szykman, *Modern Physics Letters A* **23**, 2085 (2008).
- [8] E. M. Purcell, N. F. Ramsey, *Physical Review* **78**, 807 (1950).
- [9] A. D. Sakharov, *Soviet Physics-JETP Letters* **5**, 24 (1967).
- [10] J. H. Christenson, J. W. Cronin, V. L. Fitch, and R. Turlay, *Physical Review Letters* **13**, 138 (1964).
- [11] V Fanti, A Lai, and *et al*, *Physics Letters B* **465**, 335 (1999).
- [12] BABAR Collaboration, *Physical Review Letters* **87**, 091801 (2001).

- [13] Belle Collaboratioin, *Physical Review Letters* **87**, 091802 (2001).
- [14] N. Fortson, P Sandars, and S. Barr, *Physics Today* **56**, 33 (2003).
- [15] W. Bernreuther and M. Suzuki, *Reviews of Modern Physics* **63**, 313-340 (1991).
- [16] M. Kobayashi and T. Maskawa, *Progress of Theoretical Physics* **49**, 652 (1973).
- [17] L. L. Chau and W. Y. Keung, *Physical Review Letters* **53**, 1802 (1984).
- [18] I. B. Khriplovich and S. K. Lamoreaux, *CP Violation Without Strangeness*, Springer-Verlag, 1997.
- [19] I. B. Khriplovich and M. E. Pospelov, *Soviet Journal of Nuclear Physics* **53**, 638 (1991).
- [20] J. J. Hudson, D. M. Kara, I. J. Smallman, B. E. Sauer, M. R. Tarbutt, and E. A. Hinds, *Nature* **473**, 493-496 (2011).
- [21] S. M. Barr, *International Journal of Modern Physics A* **8**, 209-236 (1993).
- [22] R. Arnowitt, B. Dutta, and Y. Santoso, *Physical Review D* **64**, 113010 (2001).
- [23] M. E. Pospelov and A. Ritz, *Annals of Physics* **318**, 119-169 (2005).
- [24] L. R. Hunter, *Science* **252**, 73-79 (1991).
- [25] B. C. Regan, E. D. Commins, C. J. schmidt, and D. DeMille, *Physical Review Letters* **88**, 071805 (2002).
- [26] S. K. Lamoreaux, *Physical Review A* **66**, 022109 (2002).
- [27] C.-Y. Liu and S. K. Lamoreaux, *Modern Physics Letters A* **19**, 1235 (2004).
- [28] Z. W. Liu and H. P. Kelly, *Physical Review A* **45**, R4210 (1992).
- [29] N. F. Ramsey, *Physical Review* **78**, 695 (1950).

- [30] B. J. Heidenreich, O. T. Elliott, N. D. Charney, K. A. Virgien, A. W. Bridges, M. A. McKeon, S. K. Peck, D. Krause, J. E. Gordon, L. R. Hunter, *Physical Review Letters* **95**, 253004 (2005).
- [31] F. L. Shapiro *Soviet Physics Uspekhi* **11**, 345 (1968).
- [32] L. I. Schiff, *Physical Reviews* **132**, 2194 (1963).
- [33] P. G. H. Sandars, *Physical Letters* **14**, 194 (1965).
- [34] A. O. Sushkov, S. Eckel, and S. K. Lamoreaux, *Physical Review A* **79**, 022118 (2009).
- [35] B. V. Vasil'ev and E. V. Kolycheva, *Soviet Physics-JETP Letters* **47**, 243 (1987).
- [36] W. Bialek, J. Moody, and F. Wilczek, *Physical Review Letters* **56**, 1623 (1986).
- [37] Y. Shapira and T. B. Reed, *Physical Review B* **5**, 4877-4890 (1972).
- [38] S. Geller, *Zeitschrift fur Kristallographie* **125**, 1 (1967).
- [39] A. Paoletti, *Physics of Magnetic Garnets*, North-Holland Publishing Company, 1978.
- [40] O. A. Petrenko, G. Balakrishnan, D. McK Paul, M. Yethiraj, and J. Klenke, *Applied Physics A* **74**, 760-762 (2002).
- [41] O. A. Petrenko, C. Ritter, M. Yethiraj, and D. McK Paul, *Physical Review Letters* **80**, 4570-4573 (1998).
- [42] P. Schiffer, A. P. Ramirez, D. A. Huse, and A. J. Valentino, *Physical Review Letters* **73**, 2500-2503 (1994).
- [43] P. Schiffer, A. P. Ramirez, D. A. Huse, P. L. Gammel, U. Yaron, D. J. Bishop, and A. J. Valentino, *Physical Review Letters* **74**, 2379-2382 (1995).

-
- [44] A. P. Ramirez, *Annual Review of Materials Science* **24**, 453-480 (1994).
- [45] C. Kittel, *Introduction to Solid State Physics*, Wiley & Sons, New York, 7th edition, 1996.
- [46] V. A. Dzuba, O. P. Sushkov, Johnson, and Safronava, *Physical Review A* **66**, 032105 (2002).
- [47] K. Lal and H. K. Jhans, *Journal of Physics C-Solid State Physics* **10**, 1315 (1977).
- [48] R. D. Shannon, M. A. Subramanian, T. H. Allik, H. Kimura, M. R. Kokta, M. H. Randles, and G. R. Rossman, *Journal of Applied Physics* **67**, 3798 (1990).
- [49] Harold Weinstock, *SQUID sensors: Fundamentals, Fabrication, and Applications*, Kluwer Academic, 1st edition, 1996.
- [50] STARCryoelectronics pcSQUIDTM User's Manual.
- [51] E. E. Hellstrom, R. D. Ray, and C. Zhang, *Journal of the American Ceramic Society* **72**, 1376 (1989).
- [52] M. A. DiGiuseppe, H. Temkin and W. A. Bonner, *Journal of Crystal Growth* **58**, 279 (1982).
- [53] G. Zhao, T. Li, X. He, and J. Xu, *Materials letters* **56**, 1098 (2002).
- [54] Quantum Design Magnetic Property Measurement System (MPMS).
- [55] John D. Jackson, *Classical Electrodynamics*, Wiley & Sons, New York, 3rd edition, 1999.
- [56] Field precision AMaze program.
- [57] W. P. Wolf, M. J. M. Leask, B. Mangum and A. F. G. Wyatt, *Journal of the Physical Society of Japan* **17** B-1, 487 (1961).

- [58] A. H. Morrish, *The Physical Principles of Magnetism*, Wiley-IEEE Press, New York, 1st edition, 2001.
- [59] S. R. Dunsiger, J. S. Gardner, J. A. Chakhalian, A. L. Cornelius, M. Jaime, R. F. Kiefl, R. Movshovich, W. A. MacFarlane, R. I. Miller, J. E. Sonier, et al., *Physical Review Letters* **85**, 3504 (2000).
- [60] I. M. Marshall, S. J. Blundell, F. L. Pratt, A. Husmann, C. A. Steer, A. I. Coldea, W. Hayes, and R. C. C. Ward, *Journal of Physics-Condensed Matter* **14**, L157 (2002).
- [61] J. A. Mydosh, *Spin Glasses: An Experimental Introduction*, Taylor & Francis, 1st edition, 1993.
- [62] J. Nenonen, J. Montonen, and T. Katil, *Review of Scientific Instruments* **55**, 2397 (1996).
- [63] C. T. Munger, *Physical Review A* **72**, 012506 (2005).
- [64] Buhmann, V. A. Dzuba, and O. P. Sushkov, *Physical Review A* **66**, 042109 (2002).
- [65] T. N. Mukhamedjanov, V. A. Dzuba, and O. P. Sushkov, *Physical Review A* **68**, 042103 (2003).
- [66] Kuenzi, O. P. Sushkov, V. A. Dzuba, and Cadogan, *Physical Review A* **66**, 032111 (2002).
- [67] http://www.mt-berlin.com/charts/chart_07.htm#IND9.
The same company also has another table:
http://www.mt-berlin.com/frames_cryst/descriptions/substrates containing a different value of $K = 12$ for GGG.
- [68] LTC2440 data sheet.

-
- [69] LT1007 data sheet.
- [70] ADR445 data sheet.
- [71] Spartan-3E FPGA data sheet.
- [72] XPort data sheet.
- [73] <http://www.mathworks.com/matlabcentral/fileexchange/345>.
- [74] Sanjit K. Mitra, *Digital Signal Processing*, McGraw-Hill Science, New York, 2nd edition, 2001.
- [75] RF PhotoMOS (AQV22O) data sheet.
- [76] Y. J. Kim, B. Kunkler, C.-Y. Liu, and G. Visser (2011), submitted.
- [77] Audio power amplifier LM2876 datasheet.
- [78] Vacuum-tube triode 6BK4C datasheet.
- [79] Paul Horowitz and Winfield, *The Art of Electronics*, Cambridge university press, 2nd edition, 1989.
- [80] Y. J. Kim, C.-Y. Liu, S. K. Lamoreaux, and G. Reddy, *Journal of Physics: Conference Series* **312**, 102009 (2011).
- [81] Y. J. Kim, C.-Y. Liu, S. K. Lamoreaux, G. Visser, B. Kunkler, A. V. Matlashov, and T. G. Reddy, Submitted.
- [82] AD5791 data sheet.
- [83] Frank Pobell, *Matter and Methods at Low Temperatures*, Springer, 3rd, revised and expanded edition, 2007.
- [84] Martin Nikolo, *American Journal of Physics* **63**, 57-65 (1995).

-
- [85] C. P. Bidinosti and W. N. Hardy, *Review of scientific instruments* **71**, 3816-3821 (2000).
- [86] Carefully calibrated 1 k Ω RuO thick-film resistance thermometer.
- [87] A Banerjee, A K Rastogi, Manoj Kumar, A Das, A Mitra and A K Majumdar, *Journal of Physics E: Scientific Instruments* **22**, 230-233 (1989).

Curriculum Vitae

Young Jin Kim

CEEM, Indiana University Cyclotron Facility
2401 N Milo B. Sampson Lane, Bloomington, IN 47408, USA
Email: yjk2@indiana.edu, Tel: +1 (812) 606-6854

Education

- (9/2011, expected) Ph.D., Physics, Indiana University, Bloomington, IN, USA
Advisor: Chen-Yu Liu
Thesis: “An experimental search for the electron Electric Dipole Moment in a Gadolinium Gallium Garnet”
- (06/2007) M.S., Physics, Indiana University, Bloomington, IN, USA
- (02/2004) M.S., Condensed Matter Physics, University of Seoul, Seoul, South Korea
Advisor: Byung-Deok Yu
Thesis: “Adsorption of a single oxygen molecule on a $c(4 \times 2)$ Si(001) surface: A first-principles study”
- (02/2002) B.S., Physics, University of Seoul, Seoul, South Korea

Professional Experience

- Indiana University, Bloomington (Research Assistant, 05/2006 - present)
Advisor: Chen-Yu Liu
 - Carried out an experimental search for the permanent electric dipole moment (EDM) of the electron using a solid state system (Gadolinium Gallium Garnet paramagnetic insulator) at low temperature. The EDM experiment provides information about the nature of T (time-reversal symmetry) violation and a fundamental EDM would provide new source of CP violation which is necessary to explain the observed baryon asymmetry of our universe. The EDM of an elementary particle, if detected, would be direct evidence of new physics beyond the Standard Model.
 - Used the unconventional solid state technique in which the EDM signal is extracted from the bulk magnetization of the paramagnetic insulator induced by an externally applied electric field. The high number density of unpaired electrons in the paramagnetic sample generates a large magnetic response which might be detectable using a state-of-the-art magnetometer such as a Superconductor Quantum Interference Device (SQUID) sensor.

- Characterized magnetic properties of the paramagnetic sample using a SQUID susceptometer system (Quantum Design MPMS).
 - Constructed a high precision 24-bit DAQ system with an ultra-low level of crosstalk between channels in order to measure a minute signal of the paramagnetic sample's Stark-induced magnetization as well as eliminate systematic effects related to the channel crosstalk.
 - Improved the high voltage polarity switch system to reduce the voltage drift to 10 ppm/s (600 times lower than previous system) to minimize the systematic effect related to the high voltage system.
 - Mastered the operation of a SQUID sensor at low temperatures and maintained stable operation of the SQUID sensor at the base magnetic noise level by studying and eliminating any sources that generate electrical RF noise as well as eliminating ground loops.
 - Conducted various tests on cryogenic-compatible high voltage cables, resistors, and capacitors to reduce the formation of dielectric discharge and stabilize the SQUID sensor.
 - Obtained the lowest background-free experimental limit of the electron EDM using the solid state technique on the order of 10^{-25} e-cm with 120 hours of data averaging.
 - Demonstrated the feasibility of the solid state method using a paramagnetic insulator at low temperatures to search the electron EDM.
- Indiana University, Bloomington (Associate Instructor, 08/2005-05/2006)
 - University of Seoul, South Korea (University Physics Instructor, 03/2005-06/2005)
 - Taught General Physics for Computer Science and Car Engineering departments (lectures and laboratory sessions).
 - University of Seoul, South Korea (Research Assistant, 03/2002-02/2004)
Advisor: Byung-Deok Yu
 - Conducted theoretical predictions for the electronic structure of condensed matters on the basis of the pseudopotential method using a Vienna *Ab initio* Simulation Package(VASP) and parallel computing.
 - Mastered proficient computational and theoretical skills in the condensed matter physics.
 - KIAS(Korea Institute for Advanced Study) (Research Assistant, 06/2002-05/2003)
Advisor: Jooyoung Lee

- Investigated protein folding using a *Ab initio* method based on Anfinsen thermodynamics.
- University of Seoul (Research Assistant, 02/2000-08/2001)
Advisor: Eun-Jip Choi
 - Conducted an experimental investigation to search a new metal superconductor with high T_c beyond MgB_2 whose T_c is around 40 K.
- Tutor (05/2000-06/2005)
 - Taught several high and middle school students in math and physics.

Awards and Grants

- (1998-2001) 5 Full tuition scholarships (Top 5% students in the class), University of Seoul, South Korea
- (2010) McCormick Science Grant (\$2500), College of Arts and Sciences, Indiana University, USA
- (2010) Travel Grant (\$500), Office of Women in Science Program, Indiana University, USA
- (2010) Student Travel Grant (\$650), International Nuclear Physics Conference 2010
- (2010) First prize in the Nuclear Physics A Young Scientist Award for best poster presentation (500 Euro (\$650)), International Nuclear Physics Conference 2010 (<http://inpc2010.triumf.ca/studentwinners.html>)
- (2011) Travel Award (\$300), College of Arts and Sciences, Indiana University, USA
- (2011) Outstanding Graduate Student in Experimental Research (\$500), Department of Physics, Indiana University, USA

Presentations

- Poster presentation
 - “A search for the permanent Electric Dipole Moment of Electron in a solid state system”, The 12th Annual Women in Science Research Conference (Bloomington, IN, USA, March 2010)

- “An experimental search for the Electric Dipole Moment of the electron based on solid-state techniques”, International Nuclear Physics Conference 2010 (Vancouver, Canada, July 2010)
- “An experimental search for the electron Electric Dipole Moment in Gadolinium Gallium Garnet”, APS (American Physical Society) April Meeting (Anaheim, CA, USA, April 2011)
- Contributed Talk
 - “Studies on magnetometry and samples used for an experimental search on the Electric Dipole Moment of the Electron using solid-state techniques”, APS April Meeting (Saint Louis, MO, USA, Apr. 2008)
 - “An experimental search for the Electric Dipole Moment of the electron based on solid-state techniques”, International Nuclear Physics Conference 2010 (Vancouver, Canada, July 2010)
 - “An experimental search for the Electric Dipole Moment of the electron based on solid-state techniques”, Fall Meeting of the APS Division of Nuclear Physics (Santa Fe, NM, USA, Nov. 2010)
- Invited talk
 - “An experimental search for the electron Electric Dipole Moment in Gadolinium Gallium Garnet”, Colloquium in the physics department of University of Nevada, Reno (Reno, NV, July 2011)

Publications

- Articles in journals
 - J. S. Ahn, **Y. J. Kim**, M. S. Kim, S. I. Lee, and E. J. Choi, “Structural and superconducting properties of $\text{MgB}_{2-x}\text{Be}_x$ ”, *Physical Review B* **65**, 172503 (2002)
 - B. D. Yu, **Y. J. Kim**, J. Jeon, H. Kim, H. W. Yeom, I. W. Lyo, K. Kong, Y. Miyamoto, O. Sugino, and T. Ohno, “*Ab initio* study of incorporation of O_2 molecules into Si(001) surfaces: Oxidation by Si ejection”, *Physical Review B* **70**, 033307 (2004)
 - **Y. J. Kim**, C. -Y. Liu, S. K. Lamoreaux, G. Visser, B. Kunkler, A. V. Matlashov, and T. G. Reddy, “New experimental limit on the Electric Dipole Moment of the Electron in a paramagnet insulator”, *Physical Review D*, submitted (2011)

- **Y. J. Kim**, B. Kunkler, C. -Y. Liu, and G. Visser, “A high dynamic range data acquisition system for a solid-state electron Electric Dipole Moment experiment”, *Review of Scientific Instruments*, submitted (2011)
- Published contributions to academic conferences
 - **Y. J. Kim**, C. -Y. Liu, S. K. Lamoreaux and G. Reddy, “Experimental search for the electron Electric Dipole Moment using solid state techniques”, Proceedings of the 24th International Nuclear Physics Conference 2010 at Vancouver in Canada, *Journal of Physics: Conference Series* **312**, 102009 (2011)